

SPARSE RECONSTRUCTION FOR NEAR-FIELD MIMO RADAR IMAGING
PROBLEMS USING FAST MULTIPOLE METHODS

A THESIS SUBMITTED TO
THE GRADUATE SCHOOL OF NATURAL AND APPLIED SCIENCES
OF
MIDDLE EAST TECHNICAL UNIVERSITY

BY

EMRE ALP MİRAN

IN PARTIAL FULFILLMENT OF THE REQUIREMENTS
FOR
THE DEGREE OF DOCTOR OF PHILOSOPHY
IN
ELECTRICAL AND ELECTRONIC ENGINEERING

JANUARY 2022

Approval of the thesis:

**SPARSE RECONSTRUCTION FOR NEAR-FIELD MIMO RADAR
IMAGING PROBLEMS USING FAST MULTIPOLE METHODS**

submitted by **EMRE ALP MİRAN** in partial fulfillment of the requirements for the degree of **Doctor of Philosophy in Electrical and Electronic Engineering, Middle East Technical University** by,

Prof. Dr. Halil Kalıpçılar
Dean, Graduate School of **Natural and Applied Sciences**

Prof. Dr. İlkay Ulusoy
Head of the Department, **Electrical and Electronics Engineering**

Prof. Dr. Sencer Koç
Supervisor, **Electrical and Electronics Engineering, METU**

Assoc. Prof. Dr. Sevinç Figen Öktem
Co-Supervisor, **Electrical and Electronics Engineering, METU**

Examining Committee Members:

Prof. Dr. Özlem Aydın Çivi
Electrical and Electronics Eng. Dept., METU

Prof. Dr. Sencer Koç
Electrical and Electronics Eng. Dept., METU

Prof. Dr. Özgür Ergül
Electrical and Electronics Eng. Dept., METU

Prof. Dr. Vakur Ertürk
Electrical and Electronics Eng. Dept., Bilkent University

Prof. Dr. Orhan Arıkan
Electrical and Electronics Eng. Dept., Bilkent University

Date: 27.01.2022

I hereby declare that all information in this document has been obtained and presented in accordance with academic rules and ethical conduct. I also declare that, as required by these rules and conduct, I have fully cited and referenced all material and results that are not original to this work.

Name Last name : Emre Alp Miran

Signature :

ABSTRACT

SPARSE RECONSTRUCTION FOR NEAR-FIELD MIMO RADAR IMAGING PROBLEMS USING FAST MULTIPOLE METHODS

Miran, Emre Alp

Doctor of Philosophy, Electrical and Electronic Engineering

Supervisor: Prof. Dr. Sencer KOÇ

Co-Supervisor: Assoc. Prof. Dr. Sevinç Figen Öktem

January 2022, 127 pages

Multiple-input-multiple-output (MIMO) radar is an advanced radar technique, where spatially distributed transmitting and receiving sub-arrays operate sequentially or simultaneously. In this technique, each antenna may transmit either the same or different waveforms, and this leads to better spatial resolution when compared to conventional phased array radar. Therefore, MIMO radar has been extensively used in imaging applications in the last two decades. In all these applications, the imaged scene is typically sparse and objects of interest are located at the near-field of the antenna. More importantly, in most of these applications, the imaging system has to deal with the requirement of high quality real-time recovery from large-scale under-sampled measurement data. In this thesis, we aim to develop an efficient sparse solution method to large-scale near-field imaging problems. For this purpose, we first construct the imaging problem as a convex optimization problem and solve it using the augmented Lagrangian based reconstruction algorithms. Then, for large scale problems, we propose applying the fast multipole method (FMM) formulation in these algorithms for efficient computation of matrix-vector products. This

approach avoids constructing and storing large-scale sensing matrices explicitly in memory and accelerates the reconstruction. We numerically test the effectiveness of the approach for several near-field imaging scenarios, ranging from point scatterers to extended targets (2-D/3-D). Results show that we can successfully apply FMM in the sparse reconstruction algorithms and it makes the reconstructions very efficient in terms of both computation time and memory usage.

Keywords: multiple-input-multiple-output antenna array, near-field radar imaging, linear inverse problem, sparse reconstruction, fast multipole method.

ÖZ

YAKIN ALAN MIMO RADAR GÖRÜNTÜLEME PROBLEMLERİ İÇİN HIZLI ÇOK KUTUP YÖNTEMİ İLE SEYREK ÇÖZÜMLEME

Miran, Emre Alp
Doktora, Elektrik ve Elektronik Mühendisliği
Tez Yöneticisi: Prof. Dr. Sencer Koç
Ortak Tez Yöneticisi: Doç. Dr. Sevinç Figen Öktem

Ocak 2022, 127 sayfa

Çok giriş-çok çıkışlı (ÇGÇÇ) radar, uzaysal olarak dağıtılmış verici ve alıcı alt dizilerin sıralı veya aynı anda çalıştığı gelişmiş bir radar tekniğidir. Bu teknikte, her anten aynı dalga biçimini gönderebileceği gibi, gönderilen dalga biçimleri birbirinden farklı da olabilir ve bu, geleneksel faz dizili radarla karşılaştırıldığında daha yüksek uzaysal çözünürlük sağlar. Bu nedenle, ÇGÇÇ radarı son yirmi yılda görüntüleme uygulamalarında yaygın olarak kullanılmıştır. Tüm bu uygulamalarda, görüntülenen uzayda genellikle az sayıda nesne bulunur ve bu nesneler antenin yakın alanındadır. Daha da önemlisi, bu uygulamaların çoğunda, görüntüleme sisteminin, büyük ölçekli ve yetersiz örneklenmiş ölçüm verilerinden yüksek kaliteli ve gerçek zamanlı çıktı vermesi beklenmektedir. Bu tezde, büyük ölçekli yakın alan görüntüleme problemlerine verimli bir seyrek çözüm yönteminin geliştirilmesi hedeflenmiştir. Bu amaçla, görüntüleme problemi öncelikle dışbükey bir optimizasyon problemi olarak kurgulanmış ve genişletilmiş Lagrange tabanlı görüntü oluşturma algoritmaları kullanılarak çözülmüştür. Ardından, büyük ölçekli problemlerde matris-vektör çarpımlarının verimli hesaplanması için bahsi geçen algoritmalara Hızlı Çok Kutup Yöntemi (HÇKY) formülasyonu uygulanmıştır. Bu

yaklaşımında büyük ölçekli algılama matrislerinin bellekte oluşturulması ve depolanması gerekmez ve dolayısıyla hızlı görüntüleme sağlanır. Noktasal saçıcılar ve yaygın hedefler (2-B/3-B) gibi çeşitli yakın alan görüntüleme senaryoları için yaklaşımın etkinliği bilgisayar ortamında test edilmiştir. Sonuçlar, HÇKY'nin seyrek yeniden yapılandırma algoritmalarına başarıyla uygulanabileceğini göstermiştir. Ayrıca, HÇKY'nin uygulanması, hem hesaplama süresi hem de bellek kullanımı açısından görüntüleme algoritmalarını çok verimli hale getirmiştir.

Anahtar Kelimeler: Çok-giriş-çok-çıkışlı anten dizisi, yakın alan radar görüntüleme, doğrusal ters problem, seyrek çözüm, hızlı çok kutuplu yöntem

To my dearest family and Büşra

ACKNOWLEDGMENTS

First and foremost, I would like to thank my esteemed supervisors Prof. Dr. Sencer Koç and Assoc. Prof. Dr. Sevinç Figen Öktem for their continuous guidance, support and encouragement through the course of my thesis studies. I also would like to thank Prof. Dr. Özlem Aydın Çivi and Prof. Dr. Vakur Ertürk for contributing to the quality of my research and guiding me by their insightful suggestions during thesis monitoring committees.

I would like to acknowledge my former colleagues Mesut Doğan, Kübra Çırçır, and Yalçın Kocagil. Their invaluable friendship and emotional support made my journey more enjoyable.

Finally, I would express my deepest gratitude to my beloved fiancée Büşra, my sister, my parents, and my grandparents, who were always with me through the course of my studies, supporting and encouraging me even in my hardest days.

TABLE OF CONTENTS

ABSTRACT.....	v
ÖZ	vii
ACKNOWLEDGMENTS	x
TABLE OF CONTENTS.....	xi
LIST OF TABLES	xiv
LIST OF FIGURES	xv
1 INTRODUCTION	1
2 INVERSE PROBLEM.....	9
2.1 Solution of Inverse Problems.....	11
2.2 Regularization of Inverse Problems.....	12
2.2.1 Singular Value Decomposition (SVD).....	13
2.2.2 Tikhonov Regularization.....	16
2.3 Sparse Solution to Inverse Problem.....	19
2.4 Numerical Approaches to Sparse Approximation	22
3 MIMO ARRAYS AND FORWARD PROBLEM	27
3.1 Literature Review.....	27
3.1.1 MIMO Array	27
3.1.2 MIMO Radar	28
3.1.3 MIMO Radar Imaging Applications	28
3.2 Imaging Geometry	29
3.2.1 Point Spread Function (PSF).....	32
3.2.2 Down-Range and Cross-Range Resolutions	34

4	FAST MULTIPOLE METHOD.....	39
4.1	The FMM Formulation.....	40
4.1.1	Addition Theorem.....	40
4.1.2	Wave Translation.....	41
4.1.3	Truncation Number.....	43
4.1.4	Integration.....	44
4.2	FMM for Near-Field MIMO Imaging Problem.....	44
4.2.1	The First Stage.....	45
4.2.2	The Second Stage.....	46
4.3	Numerical Example.....	47
5	SPARSE SOLUTION TO IMAGING PROBLEMS	51
5.1	Greedy Pursuit Methods.....	52
5.1.1	Matching Pursuit.....	53
5.1.2	Orthogonal Matching Pursuit (OMP)	54
5.1.3	Stagewise Orthogonal Matching Pursuit (StOMP).....	55
5.1.4	Other Matching Pursuit Methods.....	57
5.1.5	Numerical Examples.....	59
5.1.6	Application of FMM in OMP Algorithm	61
5.2	Convex Optimization Techniques	63
5.2.1	Alternate Direction Method of Multipliers (ADMM)	63
5.2.2	Constrained Split Augmented Lagrangian Shrinkage Algorithm (C-SALSA).	69
5.3	Numerical Examples	73
5.4	Additional Analysis	85

6	DISCRETE DIPOLE APPROXIMATION	87
6.1	Mathematical Background	87
6.2	Formulation	89
6.3	Polarizability (α)	90
6.4	Implementation of DDA	92
6.4.1	Numerical Example	94
6.5	DDA in Near-Field MIMO Imaging	96
6.6	Application of FMM in DDA	98
6.6.1	Grouping	100
6.6.2	Numerical Examples	101
7	CONCLUSION	109
8	REFERENCES	111
	CURRICULUM VITAE	125

LIST OF TABLES

TABLES

Table 4.1 Algorithmic steps of conjugate gradient least squares.	48
Table 4.2 Reflectivity values obtained using FMM and direct matrix multiplication.	49
Table 5.1 Algorithmic steps of orthogonal matching pursuit (OMP)	54
Table 5.2 Algorithmic steps for stagewise orthogonal matching pursuit.....	56
Table 5.3 Algorithmic steps of regularized orthogonal matching pursuit.	57
Table 5.4 Algorithmic steps of compressive sampling matching pursuit	58
Table 5.5 Algorithmic steps of ADMM	68
Table 5.6 Algorithmic steps of constrained split augmented Lagrangian shrinkage-I	71
Table 5.7 Algorithmic steps of constrained split augmented Lagrangian Shrinkage- II	72

LIST OF FIGURES

FIGURES

Figure 1.1. The electromagnetic spectrum and absorption characteristic of the atmosphere.	2
Figure 1.2. Illustration of down- and cross-ranges.	3
Figure 1.3. Basic SAR principle.	4
Figure 1.4. MIMO array topologies: (a) Curvilinear array, (b) rectangular array, and (c) Mill's cross array (λ_c denotes wavelength of the center frequency of the operating band).	5
Figure 2.1. Forward problem vs inverse problem.	10
Figure 2.2. Threshold function with respect to σ_i	15
Figure 2.3. Threshold-to-zero function with respect to σ_i	16
Figure 2.4. Tikhonov regularization function with respect to σ_i	18
Figure 2.5. The behaviour of x_p as a function of p	21
Figure 2.6. Solutions to (a) ℓ_0 "norm" and (b) ℓ_1 -norm minimization problems that satisfy $\mathbf{Ax} = \mathbf{b}$ constraint.	22
Figure 3.1. Plus-shaped 2-D planar MIMO array.	29
Figure 3.2. Single point scatterer illuminated by plus-shaped MIMO array.	33
Figure 3.3. PSF of the plus-shaped MIMO array along x-axis.	33
Figure 3.4. Airy diffraction patterns generated by light from two point sources passing through a circular aperture. (a) Well-resolved case, (b) sources are at a distance determined by Rayleigh criterion, and (c) unresolved case.	35
Figure 3.5. Imaging environment with (a) 2.4 cm spacing between the point scatterers and (b) 6 cm spacing between the point scatterers. (c) Rayleigh criterion and (d) well-resolved case for the plus-shaped MIMO array.	36
Figure 4.1. Expression of $\mathbf{r} - \mathbf{r}'$ as a sum of three vectors.	42
Figure 4.2. Two-stage FMM. a) 1 st stage and b) 2 nd stage [127].	45
Figure 4.3. (a) CPU time, (b) memory requirement per matrix-vector product with respect to the number of the antennas for the FMM and the direct method.	50

Figure 5.1. Block diagram for greedy pursuit algorithms [93].	52
Figure 5.2. Imaging geometry (a) for one point scatterer and (b) for two point scatterers.	60
Figure 5.3. Reconstructed point spread functions for different sparsity levels: (a) 101-sparse, (b) 21-sparse, (c) 1-sparse.	60
Figure 5.4. Reconstructed solutions for different sparsity levels: (a) 101-sparse, (b) 21-sparse, (c) 8-sparse.	61
Figure 5.5. Reconstructed solutions with FMM for different sparsity levels: (a) 101-sparse, (b) 21-sparse, (c) 8-sparse.	62
Figure 5.6. Illustration of incident signal power calculation.	74
Figure 5.7. Normalized reconstructed solution for scattering from one point scatterer.	75
Figure 5.8. Imaging configuration for three point scatterers.	76
Figure 5.9. (a) ADMM solution and (b) CGLS solution.	77
Figure 5.10. Imaging configuration for nine point scatterers.	78
Figure 5.11. Imaging results for the first scenario: (a) Actual reflectivity of the point scatterers, (b) CGLS reconstruction, and (c) FMM-based ADMM reconstruction. The reconstructions are normalized by the largest value, therefore, they share the same colorbar.	78
Figure 5.12. Imaging results for the hexagonal target: (a) Actual reflectivity of the hexagonal target, (b) CGLS reconstruction, and (c) FMM-based C-SALSA-2 reconstruction. The reconstructions are normalized by the largest value, therefore, they share the same color bar.	79
Figure 5.13. Imaging configuration for rectangular planes.	80
Figure 5.14. FMM-based C-SALSA-2 reconstructions belonging to the corresponding planes at (a) $y = 47.5$ cm, (b) $y = 50$ cm, (c) $y = 52.5$ cm, (d) $y = 55$ cm, (e) $y = 57.5$ cm, (f) $y = 60$ cm, and (g) $y = 62.5$ cm.	81
Figure 5.15. CGLS reconstructions belonging to the corresponding planes at (a) $y = 47.5$ cm, (b) $y = 50$ cm, (c) $y = 52.5$ cm, (d) $y = 55$ cm, (e) $y = 57.5$ cm, (f) $y = 60$ cm, and (g) $y = 62.5$ cm.	82

Figure 5.16. (a) FMM-based C-SALSA-2 solution and (b) CGLS solution.	83
Figure 5.17. Reconstructed images of the concentric cylinders. The left, the middle and the right columns respectively show actual reflectivity of the cylinders, CGLS reconstruction and FMM-based C-SALSA-2 reconstruction.	84
Figure 5.18. 3-D reconstruction of the concentric cylinders.....	85
Figure 5.19. Performance of the sparsity-based reconstruction in the presence of noise, when compared to CGLS.	85
Figure 5.20. Comparison of the FMM and direct matrix-vector product in terms of (a) CPU time and (b) memory.....	86
Figure 6.1. System of equations for DDA.	93
Figure 6.2. Discretized dielectric cube.....	95
Figure 6.3. Far-zone scattered electric field calculated with CM, ILDR, VIEF, and CMRR (in comparison with HFSS).	96
Figure 6.4. Grouping scenario for DDA.	101
Figure 6.5. One-box-buffer scheme, including source, buffer, and observation boxes.	101
Figure 6.6. Normalized reconstructed images at $y = 55$ cm when (a) multiple reflections are included and (b) multiple reflections are ignored in the solution of the problem.	102
Figure 6.7. HH, HV and VH polarimetric images and RGB colour composite image of Tomakomai, Japan, acquired by PALSAR using H/V polarization on August 19, 2006.....	104
Figure 6.8. Normalized actual image of hourglass-shaped target.....	105
Figure 6.9. Color-assigned images for (a) HH-polarization, (b) VV-polarization, (c) HV-polarization. (d) Resulting colour-composite image of the target.	106
Figure 6.10. Lossless dielectric cube.	107
Figure 6.11. Normalized images reconstructed with the application of FMM at (a) $y = 51$ cm, (b) $y = 55$ cm, and (c) $y = 59$ cm.....	107
Figure 6.12. (a) CPU time and (b) memory requirement as a function of the number of unknowns.....	108

CHAPTER 1

INTRODUCTION

RADAR (acronym of **R**Ange **D**etection **A**nd **R**anging) is an electromagnetic device used for locating and detecting reflecting objects of interest. Its operation is principally based on radiating electromagnetic energy into space and capturing the backscattered waves from the objects. The existence of waves was first suggested by Scottish physicist James Clerk Maxwell and proved by a series of experiments conducted by the German physicist Heinrich Hertz in 1886-1888. Although it was mainly utilized for military purposes in its early stages, recently, its usage has evolved to a wide variety of applications, one of which is microwave imaging.

The first consideration that comes to mind for any kind of imaging technology is the type of energy that is used to illuminate the scene or object under test. Microwave imaging is carried out by the use of microwave energy, which is one form of electromagnetic radiation, and it is a band in the continuous spectrum as given in Fig 1.1. The spectrum also includes visible and infrared energy regions that are used in optical imaging. Only difference between them is the wavelength of the radiated energy. For majority regions of the spectrum, constituents of atmosphere (water vapor, oxygen molecules, etc.) absorb the electromagnetic energy. The regions apart from the absorptive ones (frequencies above ultraviolet region ($> 3 \times 10^{17}$ Hz) and frequencies below infrared ($< 10^{12}$ Hz)) can be used for imaging of optically opaque objects. Microwave energy occupies the region between 3×10^8 Hz – 3×10^{11} Hz. In contrast to the energy in the visible and infrared regions, microwave energy is capable of penetrating through haze, rain, snow and clouds, which makes it viable for radar imaging applications. Also, the width of this region extends the application fields of the microwave imaging from sub-surface monitoring to medical healthcare.

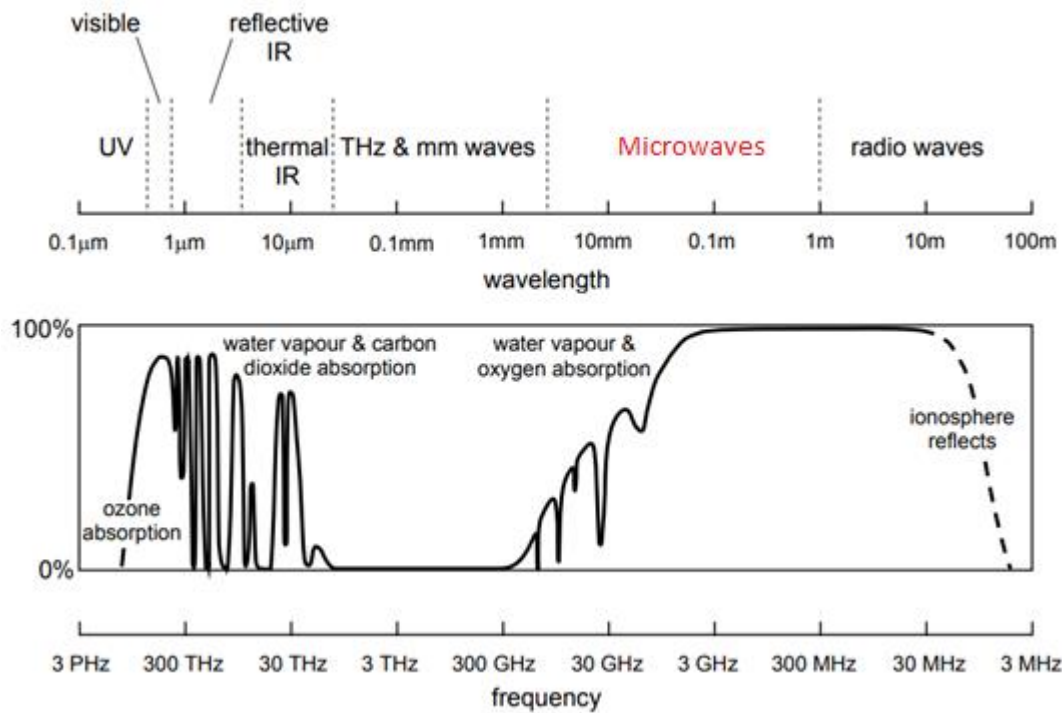


Figure 1.1. The electromagnetic spectrum and absorption characteristic of the atmosphere.

Radar imaging technology plays a key role, especially for remote sensing in critical situations, where the system is challenged by the requirement of rapid data acquisition. For example, locating people being taken hostages or getting caught in the middle of fire in a barricaded area, investigating non-metallic objects for detecting concealed weapons or improvised explosive devices at security check points, harmless scan of human body in the search for cancerous tissues, etc. can be listed for such applications [1-4]. In all of them, the radar system is installed upon a common scenario of monitoring a target (or multiple targets) residing in close proximity of the antenna aperture and it is aimed to reconstruct real-time image with a fine resolution.

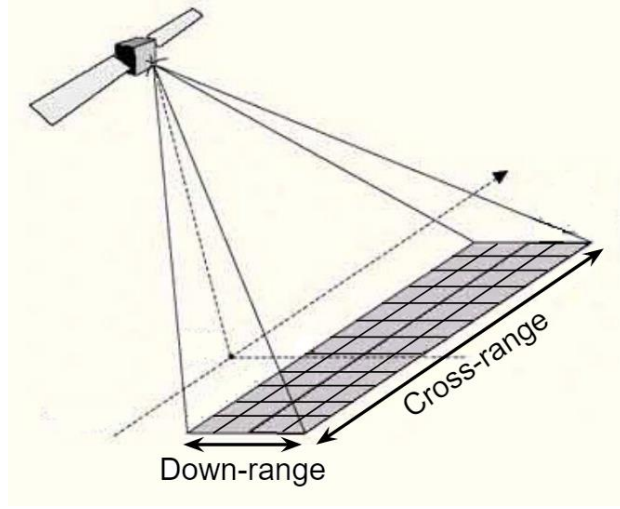


Figure 1.2. Illustration of down- and cross-ranges.

In the last two decades, ultra-wideband (UWB) radar systems have attracted the researchers, specifically in the fields of microwave sensing and radar imaging applications. A UWB radar system transmits ultra-narrow pulses that occupy a very large bandwidth since they change very rapidly. These pulses can penetrate through surrounding objects and allow high resolving capability in both down- and cross-range, leading to a three-dimensional (3-D) image reconstruction. The down-range resolution δ_{dr} of a radar system is directly related to the bandwidth of the transmission by

$$\delta_{dr} = \frac{c}{2B}$$

where, c is speed of light. The cross-range resolution δ_{cr} is determined by wavelength at the center frequency λ_c , distance to the target R , and aperture width of the array L in orthogonal dimensions and is given as:

$$\delta_{cr} \approx \frac{R\lambda_c}{L}$$

In addition, rather than simple target detection, waveform of the scattered UWB signal carries information about target's physical structure and electrical characteristics in its content, which eventually leads to target identification.

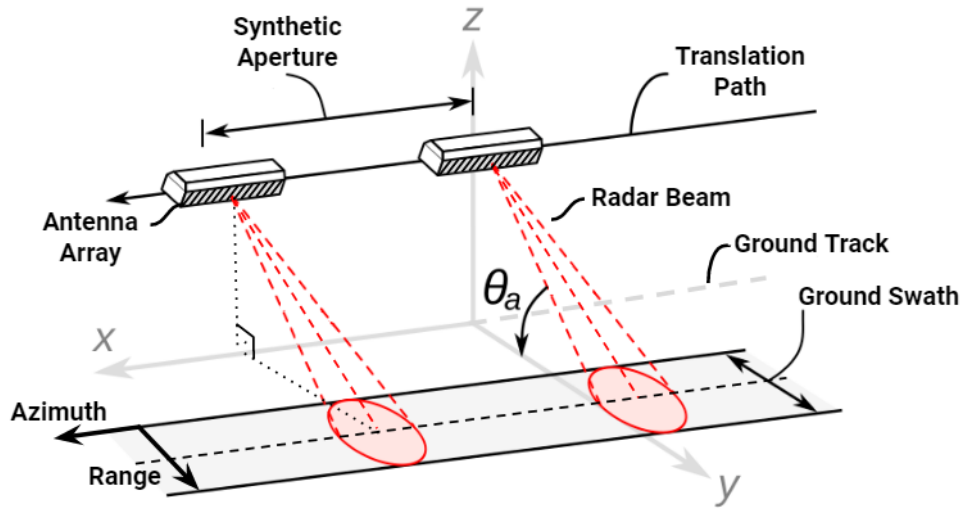


Figure 1.3. Basic SAR principle.

UWB technology has been implemented into synthetic aperture radar (SAR) systems for many imaging applications (including topography, oceanography, geomorphology, etc.) where imaging is carried out mostly by an array of identical transceiver pairs. Such systems can provide high azimuthal resolution through the use of a large synthetic aperture, which is generated by the translation of the antennas in space. However, the azimuthal resolution is limited by the length of this translation. Besides, for high resolution, the scattered fields are usually sampled by very densely placed transceivers. This requirement leads to two significant challenges: Increased data acquisition time and implementation cost (including manufacturing of the dense array and design of supporting electronic equipment), therefore, SAR systems may not be an appropriate tool for real-time near field imaging applications.

One key approach in order to deal with these challenges is implementation of multiple-input-multiple-output (MIMO) array topologies. MIMO arrays are characterized by spatially distributed transmitting and receiving sub-arrays, which are able to operate sequentially or simultaneously. In association with UWB transmission, real aperture radar systems with well-designed MIMO array topology

can provide 3-D images with improved resolution using fewer number of antennas than number of measurements required for SAR applications. With the adoption of UWB MIMO radar system, near-field imaging can be performed with reduced data-acquisition time and computational cost [1, 5-12].

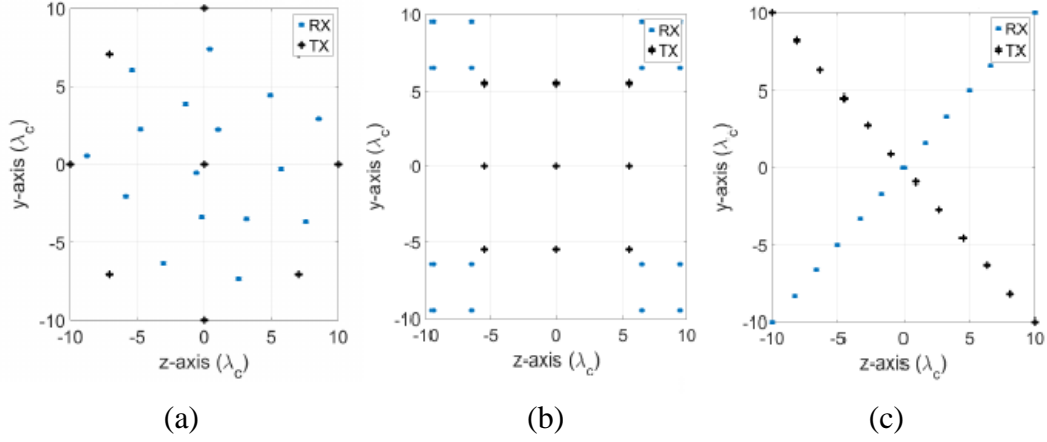


Figure 1.4. MIMO array topologies: (a) Curvilinear array, (b) rectangular array, and (c) Mill's cross array (λ_c denotes wavelength of the center frequency of the operating band).

In monochromatic case, the spacing between the antenna elements in an array must be about half-wavelength ($\lambda/2$) in order to avoid grating lobes in the radiation pattern, which directly affects the resolution of the radar system. Therefore, array aperture plays key role to establish the trade-off between the resolution and the data acquisition time. On the other hand, non-monochromatic approach is able to provide both low grating lobe level and high resolution through the use of specific MIMO array topologies, namely sparse arrays. Despite the fact that the grating lobes emerge because of the periodic reduction of antenna elements, in association with UWB transmission, the interference area around the main lobe can be reduced to a very small area. Hence, as the fractional bandwidth increases, influence of the grating lobes on the array pattern is significantly reduced. Recently, usage of sparse MIMO arrays in UWB radar imaging applications has been increased significantly [9, 11-12]. Several sparse MIMO array topologies are investigated for this reason, especially in near-field imaging applications [6-10, 13-17].

In a conventional MIMO radar system, the transmitting sub-array illuminates the target space with electromagnetic waves and the scattered fields are captured by the receiving sub-array. After reception, the fields are digitized into back-scattered data and processed by several reconstruction algorithms in order to obtain the image of the scene. Design of such system can be divided into three parts:

- (i) Design of the MIMO array configuration,
- (ii) design of transceiver module (TR module) and supporting electronic hardware,
- (iii) and implementation of the reconstruction algorithms.

This study focuses on the last part, specifically seeks an efficient sparse reconstruction to large-scale near-field MIMO radar imaging problems by developing a fast multipole method (FMM) based approach. The research activities that carried out in the scope of this thesis can be given step by step as follows:

Radar imaging is treated as the inverse problem of target detection and investigated by the use of its forward counterpart. Definition of ill-posedness, the shortcomings that it causes on the solution of inverse problem, and regularization approach to deal with them are discussed. Sparsity constraint and related sparse approximation concept are studied.

A plus-shaped MIMO configuration is designed to be used for near-field imaging applications and corresponding forward problem is established to relate reflectivity characteristics of the imaged scene to measurement data. The problem is then discretized using a predefined grid and converted into a linear system of equations. It is shown that solution of this system gets computationally demanding, as the grid size and extents of the imaging configuration (e.g. array aperture) increase.

Diagonalizability of the sensing operator and fast Fourier transforms are commonly utilized in the literature for efficient solution of large-scale near-field imaging problems [129-132]. These methods attempt to reduce computation time and memory requirement. Here in this thesis, it is demonstrated that FMM can be

employed when solving the radar imaging problem by exploiting the fact that its forward part is an electromagnetic scattering problem. Hence, matrix-vector products within the reconstruction algorithms can be carried out without forming the matrix (or its conjugate transpose) explicitly.

Sparse reconstruction methods, such as greedy pursuit (based on ℓ_0 “norm”) and convex optimization (based on ℓ_1 -norm), are investigated and demonstrated for various near-field MIMO radar imaging scenarios with a sparse scene. Then, for large-scale problems, the developed FMM-based approach is applied in the sparse reconstruction algorithms to efficiently calculate matrix-vector products, enabling accelerated CPU time and reduced memory usage.

Finally, discrete dipole approximation (DDA) is investigated and applied in near-field MIMO radar imaging problems in order to add the contribution from multiple reflections in the solutions, and thereby observe the visible and quantitative improvements on the sparse reconstructions. Furthermore, the FMM is applied in the DDA solution and further acceleration is sought, which depends on the discretization level.

Following the introduction chapter, the research goals are appropriately organized and written out as given below:

In Chapter 2, imaging problem is defined as a discretized linear inverse problem and its shortcomings are explained. Regularization methods, especially sparsity constraint, are discussed.

In Chapter 3, brief literature review on MIMO array, MIMO array-based radar, and its imaging applications are presented. A near-field radar imaging configuration with a plus-shaped MIMO array is implemented and corresponding forward problem is approximated using Born approximation. Then, the imaging problem is discretized and converted to a linear system of equations using a predefined grid. Also, the target is assumed to be stationary.

In Chapter 4, FMM and its mathematical background are briefly introduced. Then, a two stage FMM-based method is developed, which can be employed to efficiently calculate matrix-vector products within reconstruction algorithms. A small-scale near-field MIMO radar imaging problem is implemented and iteratively solved to demonstrate the applicability of the FMM-based method. Afterwards, the computational improvement that FMM can provide for large-scale problems is analyzed in terms of CPU-time and memory requirement.

In Chapter 5, several off-the-shelf sparse reconstruction algorithms are presented in detail. Each algorithm is numerically tested for different imaging scenarios with the incorporation of FMM formulation. The effect of FMM on the solutions are investigated in terms of computation time and memory requirement.

In Chapter 6, DDA, its background and implementation as a linear system of equations are presented. Usage of DDA for near-field MIMO imaging problems are mathematically explained and demonstrated by a numerical example. The reconstructed images are compared to those obtained without DDA in terms of image quality and results are reported. Finally, the FMM is applied in the DDA-based solution in order to obtain computational efficiency as a function of discretization level of the imaged scene.

Finally in Chapter 7, summary of this thesis is provided with concluding remarks.

CHAPTER 2

INVERSE PROBLEM

The problem of locating a target and identifying its characteristics by the indirect observations underlie all types of radar applications. This kind of problem is typically referred to as an inverse problem, which can be established with the use of its counterpart, namely forward problem. A classical forward problem directly estimates the observation data using known physical parameters and problem geometry through an appropriate mathematical model. Hadamard described that an inverse problem is called “well-posed”, if

- a solution exists,
- the solution is unique,
- and the solution is stable, implying that the problem has a solution that depends continuously on input data [18,19].

If the problem violates any of these rules, it is accepted as *ill-posed*. Inverse problems generally do not have unique solution and are very sensitive to small deviations on its initial values, therefore, they are ill-posed in Hadamard sense.

A linear mathematical model, which relates the observation data to the physical parameter(s) of interest, is expressed as

$$\mathbf{Ax} = \mathbf{b} \quad (2.1)$$

where $\mathbf{A} \in \mathbb{C}^{M \times N}$ is system matrix, representing direct operator of the linear model, $\mathbf{b} \in \mathbb{C}^M$ is observation data, presumed to be known, and $\mathbf{x} \in \mathbb{C}^N$ is a vector into which the unknowns are stacked in proper order. In real life applications, observations are always noisy and true form of the mathematical model is

$$\mathbf{b} = \mathbf{Ax} + \boldsymbol{\varepsilon} \quad (2.2)$$

where $\boldsymbol{\varepsilon} \in \mathbb{C}^M$ is an additive vector that constitutes random perturbation on the observation data with a known statistical model. It might be caused by modeling

errors, physical measurement errors, or numerical implementation errors due to finite precision etc.

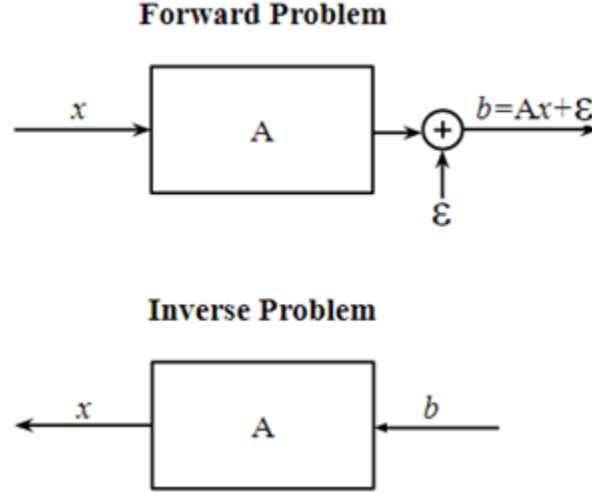


Figure 2.1. Forward problem vs inverse problem.

In the sense of the descriptions above, the calculation of \mathbf{b} using \mathbf{A} and \mathbf{x} (both are known) is the forward problem. Its solution is unique and it is insensitive to the observational noise. However, the estimation process of the unknown \mathbf{x} using noisy (and limited) observation data \mathbf{b} is the inverse problem.

The solution of a continuous inverse problem can be done on a computer by replacing the problem by its discrete version. This leads to an ill-conditioned system since the inverse problems tend to be ill-posed. Condition number of the matrix $\kappa(\mathbf{A})$, determines conditioning of the inverse problem and it is defined as

$$\kappa(\mathbf{A}) = \frac{\sigma_{max}}{\sigma_{min}} \quad (2.3)$$

where σ_{max} and σ_{min} denote maximum and minimum singular values of \mathbf{A} , respectively. A linear system with high condition number is called ill-conditioned, which indicates that the solution is sensitive to small perturbations on \mathbf{b} [19].

The forward model of an imaging system creates the back-scattered data \mathbf{b} for the imaged domain with the use of reflectivity distribution \mathbf{x} and forward operator \mathbf{A} as illustrated in Fig. 2.1. On the other hand, the original imaging problem based upon

the same model is to reconstruct the reflectivity distribution \mathbf{x} from the measurements of the back-scattered data \mathbf{b} under the environmental noise $\boldsymbol{\epsilon}$, which is typically in normal distribution. Such imaging problem is characterized as an ill-posed inverse problem.

During the imaging process, the scene is typically discretized by a very large number of points and only a limited (generally insufficient) number of measurements are available. In mathematics, a linear system with fewer equations than the number of unknowns is called under-determined (in contrast, if there are more equations than the number of unknowns, it is an over-determined system). Therefore, an imaging problem is generally under-determined by its nature. An under-determined system has either no solution or infinitely many solutions. A priori information is required to narrow down the number of solutions and obtain the most useful one.

2.1 Solution of Inverse Problems

One naive approach for the solution of an inverse problem with a square and invertible matrix $\mathbf{A} \in \mathbb{C}^{N \times N}$ is to find \mathbf{A}^{-1} and simply ignore the effect of the noise on the problem. The solution is then given by

$$\mathbf{x} = \mathbf{A}^{-1}\mathbf{b}. \quad (2.4)$$

For an over-determined system ($\mathbf{A} \in \mathbb{C}^{M \times N}, M > N$), the solution can be handled by a straightforward approach that is based on converting the problem into least squares problem

$$\min_{\mathbf{x}} \|\mathbf{b} - \mathbf{A}\mathbf{x}\|_2^2$$

whose solution is given as

$$\hat{\mathbf{x}}_{LS} = (\mathbf{A}^H \mathbf{A})^{-1} \mathbf{A}^H \mathbf{b} \quad (2.5)$$

where, \mathbf{A}^H is conjugate transpose of \mathbf{A} . On the other hand, for an under-determined system ($\mathbf{A} \in \mathbb{C}^{M \times N}, N > M$), there are infinitely many solutions, therefore, the most

useful solution among them should be picked. For example, the solution with minimum norm $\hat{\mathbf{x}}_{MN}$ is a straightforward approach for such a system and given by

$$\hat{\mathbf{x}}_{MN} = \underset{\mathbf{x}}{\operatorname{argmin}} \|\mathbf{x}\|_2^2 \quad \text{subject to} \quad \mathbf{b} = \mathbf{Ax}, \quad (2.6)$$

and the solution is given by

$$\hat{\mathbf{x}}_{MN} = \mathbf{A}^H(\mathbf{AA}^H)^{-1}\mathbf{b}. \quad (2.7)$$

It must be noted that an underdetermined system might be inconsistent, which means that it does not have an exact solution. However, it is still possible to find infinitely many solutions that minimize $\|\mathbf{b} - \mathbf{Ax}\|_2^2$. Among such solutions, there exists a unique minimum norm one and is called the minimum norm least squares solution.

All naive approaches given above are based on determining the inverse of an ill-conditioned matrix (either \mathbf{A}^{-1} or pseudo-inverse) and they often tend to fail for the solution of imaging problems. There exist some preconditioning methods for such non-invertible matrices, but they do not guarantee stable solutions. On the other hand, regularization of the problem is an effective method for such circumstances.

2.2 Regularization of Inverse Problems

Some modifications, alongside with a priori information, can be applied on the imaging problem in order to obtain approximate solutions that are less sensitive to noise when compared to the standard naive approaches. This modification procedure is called “regularization” and it replaces the ill-conditioned problem with a better-conditioned one, whose solution is approximation to the original solution.

Let the unknowns in (2.1) and (2.2) be renamed as \mathbf{x}^{exact} and $\hat{\mathbf{x}}$ so that the equations that they satisfy will take the form of

$$\mathbf{Ax}^{exact} = \mathbf{b} \quad (2.8)$$

and

$$\mathbf{A}\hat{\mathbf{x}} = \mathbf{b} + \boldsymbol{\varepsilon}, \quad (2.9)$$

respectively. In association with the perturbation theory, components of (2.6) and (2.7) satisfy following bound relation

$$\frac{\|\mathbf{x}^{exact} - \hat{\mathbf{x}}\|_2}{\|\mathbf{x}^{exact}\|_2} \leq \kappa(\mathbf{A}) \frac{\|\boldsymbol{\varepsilon}\|_2}{\|\mathbf{b}\|_2}, \quad (2.10)$$

which indicates that the approximate solution of a perturbed linear system may diverge from the exact solution, when the condition number $\kappa(\mathbf{A})$ is very high. The perturbations close to the upper bound are always encountered in discrete inverse problems, hence, regularization is strictly required in order to obtain rather stable and useful approximations for \mathbf{x}^{exact} , specifically in imaging problems.

2.2.1 Singular Value Decomposition (SVD)

As stated earlier, the minimum norm least squares solution to an inconsistent underdetermined system is unique. This solution can be obtained by SVD, which is a well-known method for solving discrete ill-conditioned inverse problems.

SVD of $\mathbf{A} \in \mathbb{C}^{M \times N}$ ($\text{rank}(\mathbf{A}) = r$) takes the form of

$$\mathbf{A} = \mathbf{U}\boldsymbol{\Sigma}\mathbf{V}^H \quad (2.11)$$

where, $\mathbf{U} = [\mathbf{u}_1, \mathbf{u}_2, \dots, \mathbf{u}_r] \in \mathbb{C}^{M \times r}$ and $\mathbf{V} = [\mathbf{v}_1, \mathbf{v}_2, \dots, \mathbf{v}_r] \in \mathbb{C}^{N \times r}$ are unitary matrices containing left and right singular vectors, respectively, and $\boldsymbol{\Sigma} = \text{diag}[\sigma_1, \sigma_2, \dots, \sigma_r] \in \mathbb{C}^{r \times r}$ is a diagonal matrix whose entries are singular values of \mathbf{A} that are placed into matrix in the following order

$$\sigma_1 \geq \sigma_2 \geq \dots \geq \sigma_r > 0.$$

Using SVD, it is straightforward to show that pseudoinverse of \mathbf{A} is

$$\mathbf{A}^+ = \mathbf{V}\boldsymbol{\Sigma}^{-1}\mathbf{U}^H, \quad (2.12)$$

thus, the minimum norm least squares solution can be rewritten as

$$\hat{\mathbf{x}}_{MMLS} = \mathbf{V}\mathbf{\Sigma}^{-1}\mathbf{U}^H\mathbf{b}. \quad (2.13)$$

2.2.1.1 Truncated Singular Value Decomposition (TSVD)

For an ill-conditioned system, the singular values of \mathbf{A} gradually converges to zero, therefore, $\kappa(\mathbf{A})$ becomes very large (see (2.3)). In order to avoid division by very small singular values in (2.14), $\mathbf{\Sigma}$ can be redefined in a truncated form

$$\mathbf{\Sigma} = \text{diag}[\sigma_1, \sigma_2, \dots, \sigma_k, 0, \dots, 0]$$

where, $\sigma_{k+1}, \dots, \sigma_r$ are set to zero and k denotes truncation number. TSVD replaces \mathbf{A} by \mathbf{A}_k and (2.13) turns into

$$\mathbf{A}_k^+ = \mathbf{V}\mathbf{\Sigma}_k^{-1}\mathbf{U}^H. \quad (2.14)$$

Hence, we have the TSVD solution as

$$\hat{\mathbf{x}}_{MMLS,k} = \mathbf{V}\mathbf{\Sigma}_k^{-1}\mathbf{U}^H\mathbf{b} \equiv \sum_{i=1}^k \frac{\mathbf{u}_i^H\mathbf{b}}{\sigma_i} \mathbf{v}_i. \quad (2.15)$$

The truncation number k governs the regularization of the problem and determines how sensitive the solution is in the presence of perturbation. Selection of k is very significant, i.e., as k increases, the approximate solution gets more sensitive to the perturbation, and as k decreases, the approximation falls far from the actual solution [20]. Literature offers wide range of methods for the selection of optimal k value, which can be found in [21-24].

It is also possible to filter out the excessively small singular values in a systematic way. One such approach is a member of general class of techniques, namely spectral filtering, that are expressed as

$$\hat{\mathbf{x}}_\lambda = \sum_{i=1}^k \phi_i^{[\lambda]} \frac{\mathbf{u}_i^H\mathbf{b}}{\sigma_i} \mathbf{v}_i \quad (2.16)$$

where λ denotes regularization parameter and $\phi_i^{[\lambda]}$ is filtering factor for i^{th} singular value, e.g., it can be chosen as 1 for large singular values while it can be chosen as 0

for the rest. Two widely used choices for $\phi_i^{[\lambda]}$ are given below and illustrated in Fig. 2.2 and Fig. 2.3.

i) Threshold function:

$$\phi_i^{[\lambda]} / \sigma_i = \frac{1}{\max(\sigma_i, \lambda)}$$

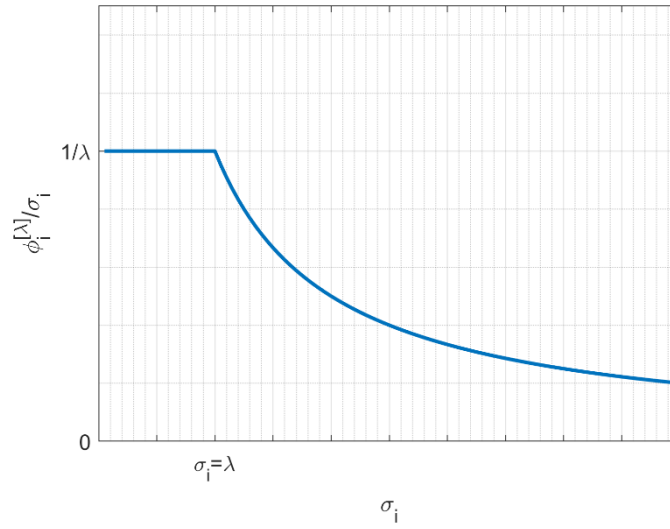


Figure 2.2. Threshold function with respect to σ_i .

ii) Threshold-to-zero function

$$\phi_i^{[\lambda]} / \sigma_i = \begin{cases} 1/\sigma_i, & \sigma_i > \lambda \\ 0, & \text{otherwise} \end{cases}$$

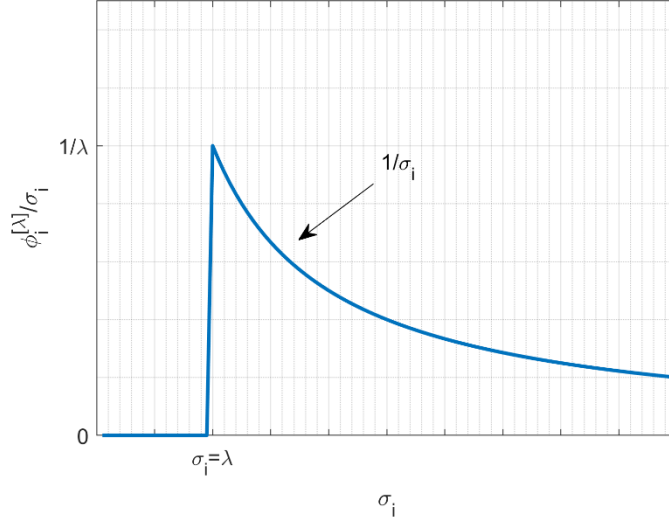


Figure 2.3. Threshold-to-zero function with respect to σ_i .

2.2.2 Tikhonov Regularization

SV-based regularization methods attempt to compute all singular values (or at least the most useful ones) and vectors explicitly. This is a computationally intensive method, therefore, they are mostly applied to ill-conditioned systems with matrices of small or moderate size. For large scale problems, one needs a more efficient way.

The concept of Tikhonov regularization was visited independently several times in the past, however, became popular after its application to the solution of integral equations by Andrey Tikhonov [26-28] and David L. Phillips [29]. Tikhonov added a regularization term into the problem and formulated the solution as

$$\min_{\mathbf{x}} \|\mathbf{b} - \mathbf{Ax}\|_2^2 + \|\mathbf{L}_\lambda \mathbf{x}\|_2^2. \quad (2.17)$$

$\mathbf{L}_\lambda \in \mathbb{C}^{k \times N}$, $k \leq n$, is the regularization matrix, which is commonly selected as $\mathbf{L}_\lambda = \lambda \mathbf{I}$, where \mathbf{I} is the identity matrix. Regarding available a priori information, \mathbf{L}_λ might also be selected as finite difference approximation of a differential operator or a scaled orthogonal projection [21, 30-33]. In (2.17),

- the first term $\|\mathbf{b} - \mathbf{Ax}\|_2^2$ estimates a least squares solution from a perturbed data \mathbf{b}
- and the second term $\|\mathbf{L}_\lambda \mathbf{x}\|_2^2$ applies smoothness into the problem by suppressing the perturbation through the control of l_2 -norm of \mathbf{x} .

The value of regularization parameter λ is the key factor in order to establish a balance between the two terms and find a sufficiently regularized solution. If it is too large, the second term dominates the formulation, thus, the least squares problem in the first term becomes meaningless. On the other hand, if it is too small, regularization of \mathbf{x} cannot be achieved because the noisy data has more weight.

Note that as $\lambda \rightarrow \infty$, solution of (2.17) becomes the zero vector, and as $\lambda = 0$, the formulation turns into the original least squares problem and \mathbf{x} becomes the naive solution to that problem.

Given $\mathbf{L}_\lambda = \lambda \mathbf{I}$, (2.17) can be rewritten as

$$\min_x \{\|\mathbf{b} - \mathbf{Ax}\|_2^2 + \lambda^2 \|\mathbf{x}\|_2^2\} \Rightarrow \min_x \left\{ \left\| \begin{bmatrix} \mathbf{b} \\ 0 \end{bmatrix} - \begin{bmatrix} \mathbf{A} \\ \lambda \mathbf{I} \end{bmatrix} \mathbf{x} \right\|_2^2 \right\} \Rightarrow \min_x \{\|\tilde{\mathbf{b}} - \tilde{\mathbf{A}}\mathbf{x}\|_2^2\}$$

and solution of which is in the form of

$$\begin{aligned} \mathbf{x}_{Tikhonov} &= (\tilde{\mathbf{A}}^H \tilde{\mathbf{A}})^{-1} \tilde{\mathbf{A}}^H \tilde{\mathbf{b}} = \left(\begin{bmatrix} \mathbf{A}^H & \lambda \mathbf{I} \end{bmatrix} \begin{bmatrix} \mathbf{A} \\ \lambda \mathbf{I} \end{bmatrix} \right)^{-1} \begin{bmatrix} \mathbf{A}^H & \lambda \mathbf{I} \end{bmatrix} \begin{bmatrix} \mathbf{b} \\ 0 \end{bmatrix} \\ &= (\mathbf{A}^H \mathbf{A} + \lambda^2 \mathbf{I})^{-1} \mathbf{A}^H \mathbf{b}. \end{aligned}$$

Tikhonov solution to an inverse problem is equivalent to a filtered solution by using SVD. Inserting SVD of a full column matrix \mathbf{A} into the equations and using $\mathbf{I} = \mathbf{V}\mathbf{V}^H$, the solution becomes

$$\begin{aligned} \mathbf{x}_{Tikhonov} &= (\mathbf{V}\Sigma^2\mathbf{V}^H + \lambda^2\mathbf{V}\mathbf{V}^H)^{-1} \mathbf{V}\Sigma\mathbf{U}^H \mathbf{b} \\ &= \mathbf{V}(\Sigma^2 + \lambda^2\mathbf{I})^{-1} \mathbf{V}^H \mathbf{V}\Sigma\mathbf{U}^H \mathbf{b} \\ &= \mathbf{V}(\Sigma^2 + \lambda^2\mathbf{I})^{-1} \Sigma\mathbf{U}^H \mathbf{b}. \end{aligned}$$

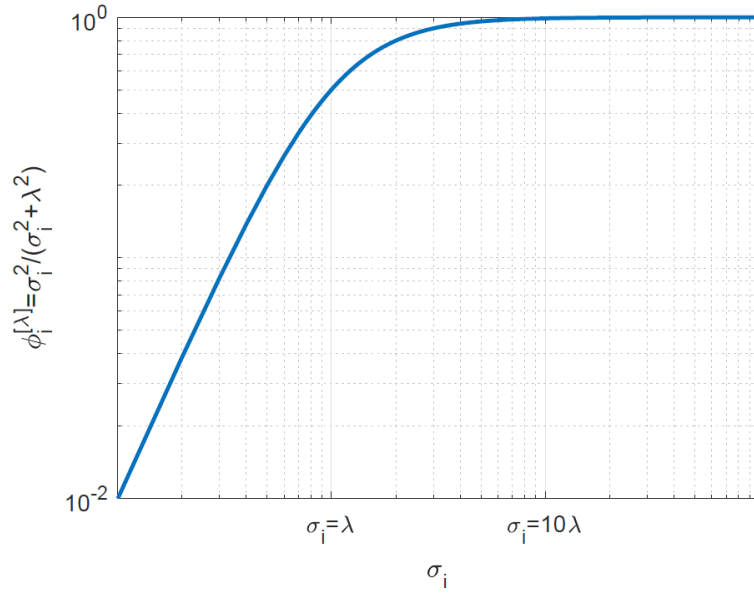


Figure 2.4. Tikhonov regularization function with respect to σ_i .

In the form of (2.16), $\mathbf{x}_{Tikhonov}$ can be recast as

$$\mathbf{x}_{Tikhonov} = \sum_{i=1}^k \phi_{T,i}^{[\lambda]} \frac{\mathbf{u}_i^H \mathbf{b}}{\sigma_i} \mathbf{v}_i \quad (2.18)$$

where

$$\phi_{T,i}^{[\lambda]} = \frac{\sigma_i^2}{\sigma_i^2 + \lambda^2} \approx \begin{cases} 1, & \sigma_i \gg \lambda \\ \sigma_i^2 / \lambda^2, & \sigma_i \ll \lambda \end{cases}$$

is Tikhonov regularization function and k is rank of \mathbf{A} . Fig. 2.4 depicts the behaviour of $\phi_{T,i}^{[\lambda]}$. It can be seen that as the singular values are larger than parameter λ , the filtering factor approaches to one and corresponding components directly contributes to $\mathbf{x}_{Tikhonov}$. On the other hand, for the singular values that are much smaller than λ , $\phi_{T,i}^{[\lambda]}$ is proportional to σ_i^2 , hence, corresponding components become negligible and get filtered out. Through the use of λ , the filtering can be controlled in a similar way that parameter k is used in TSVD. However, the most significant feature, which discriminates Tikhonov regularization from TSVD, is that the transition between the

filtered and maintained components are smoother and the filtering process is performed without explicitly computing the SVD of \mathbf{A} .

2.3 Sparse Solution to Inverse Problem

Over the last two decades, the demand for the analysis of high-dimensional linear inverse problems has grown, specifically in engineering applications. One fundamental approach to handle such problems is sparsity constraint, which is able to overcome the shortcomings of the problem (ill-posedness, underdetermined nature, etc.) and exploit them for the improvement at the quality of its solution. The sparsity constraint provides, except for regularization, an approximate solution that contains few non-zero entries when compared to its dimension. This approach is referred to as “sparse approximation” [34-35].

Note that Tikhonov regularization generally does not guarantee a sparse solution. In [36], two sparse reconstruction algorithms are proposed based on generalized Arnoldi-Tikhonov regularization, approximating l_1 -norm and total variation in terms of l_2 -norm. These algorithms can provide a sparse solution for the problem within fewer iterations than classical Tikhonov regularization algorithm at the cost of higher relative error.

The most basic expression for the sparse approximation is given by

$$\min_{\mathbf{x}} \|\mathbf{x}\|_0 \quad \text{subject to} \quad \mathbf{Ax} = \mathbf{b} \quad (2.19)$$

where $\|\cdot\|_0 : \mathbb{C}^N \rightarrow \mathbb{R}$ can be denoted as ℓ_0 “norm”^{*}, which gives the number of non-zero entries of a vector in \mathbb{R}^N . $\|\mathbf{x}\|_0 \leq s$ infers that the solution vector \mathbf{x} is s -

^{*} The reason why this term is written in quotation marks is that it is not a proper norm. It does not satisfy homogeneity condition, i.e., scaling a vector with a positive constant does not scale the “norm” as well.

sparse. In the case that the observed data is contaminated by noise, an error tolerance $\varepsilon \geq 0$ can be added to (2.19)

$$\min_{\mathbf{x}} \|\mathbf{x}\|_0 \quad \text{subject to} \quad \|\mathbf{b} - \mathbf{Ax}\|_2^2 \leq \varepsilon. \quad (2.20)$$

The regularization parameter λ can be added into the problem to obtain a balance between goals of minimizing error and number of non-zero components by

$$\min_x \|\mathbf{b} - \mathbf{Ax}\|_2^2 + \lambda \|\mathbf{x}\|_0. \quad (2.21)$$

It is apparent that (2.20) resembles the minimum l_2 -norm problem (2.6). Despite the notational similarity, there exists a significant difference between them. The solution to (2.6) is always unique and can be obtained using off-the-shelf methods based on computational linear algebra. On the other hand, (2.20) poses many mathematical challenges due to discrete and discontinuous nature of ℓ_0 “norm”. The exhaustive combinatorial search for all possible sparse subsets is generally exponential in the number of columns. This makes the solution of (2.20) NP-hard, meaning that it cannot be solved in polynomial time.

Although ℓ_0 “norm” provides a very simple concept for sparsity, it is not always feasible for practical cases (e.g. radar imaging) due to the fact that the actual solution vector rarely contains many strict zeroes in its entries. However, a solution vector containing small number of non-zero elements, can be approximated by applying weak l_p -norm.

The l_p -norm acts as a powerful sparsity constraint in the range of $0 < p \leq 1$ and is mathematically defined by

$$\|\mathbf{x}\|_p = (\sum_i |x_i|^p)^{1/p}, \quad (2.22)$$

thus, the problem to be solved is in the form

$$\min_{\mathbf{x}} \|\mathbf{x}\|_p \quad \text{subject to} \quad \mathbf{Ax} = \mathbf{b}. \quad (2.23)$$

Any p selection within $0 < p < 1$, e.g. $p = \frac{1}{2}$, $p = \frac{2}{3}$, makes (2.23) a non-convex problem, which is very hard to solve. As $p \rightarrow 0$, the ℓ_0 “norm” can be related to l_p -norm by

$$\|\mathbf{x}\|_0 = \lim_{p \rightarrow 0} \|\mathbf{x}\|_p^p = \lim_{p \rightarrow 0} \sum_{k=1}^N |x_k|^p. \quad (2.24)$$

Fig. 2.5 illustrates the behaviour of $|x|^p$ as a function of p . It can be seen that as $p \rightarrow 0$, $|x|^p$ becomes a count function, which returns 0 for $x = 0$ and 1 otherwise.

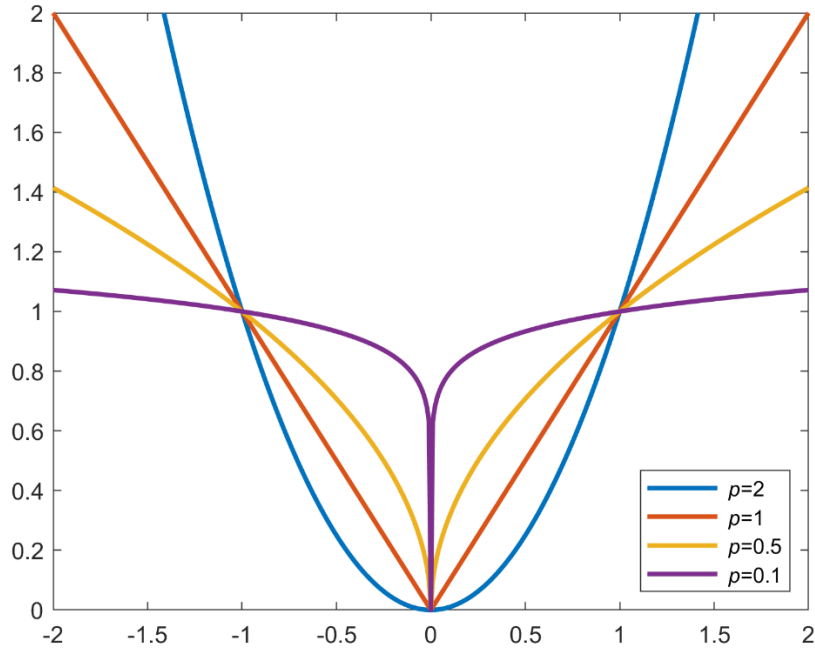


Figure 2.5. The behaviour of $|x|^p$ as a function of p .

When $p = 1$, (2.23) becomes a convex minimization problem. In the sense of sparse solution, l_1 -norm is the closest convex function to ℓ_0 “norm”. The solutions to l_1 -norm and ℓ_0 “norm” minimization problems that satisfy $\mathbf{Ax} = \mathbf{b}$ constraint are drawn in Fig. 2.6. As can be seen in Fig. 2.6(b), l_1 -norm and the constraint intersect at sparse solution (i.e. x_1 is non-zero, x_2 is zero). So, minimization of l_1 -norm can yield the sparsest solution, which also satisfies the minimization of ℓ_0 “norm”, among the

infinitely many solutions. Hence, the sparsest solution can be obtained with standard convex optimization tools.

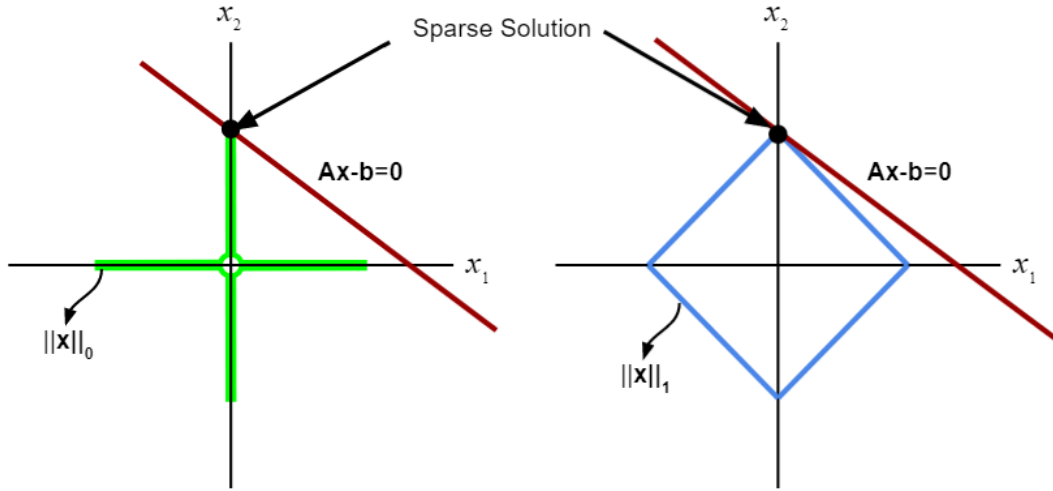


Figure 2.6. Solutions to (a) ℓ_0 “norm” and (b) ℓ_1 -norm minimization problems that satisfy $Ax = b$ constraint.

2.4 Numerical Approaches to Sparse Approximation

In this thesis, two types of numerical approaches, based on sparse approximation, are investigated: Pursuit methods and convex optimization techniques. These approaches are discussed in Chapter 5 in detail.

- Greedy pursuit methods search for an approximate solution by iteratively picking the components that contribute to sparsity most. Orthogonal matching pursuit (OMP) is a greedy method. It iteratively attempts to refine a sparse solution. The iterations are continued until a predetermined sparsity level is reached. Stagewise orthogonal matching pursuit (StOMP) is another type of greedy method based on OMP. It simply differs from OMP by selecting multiple columns at each iteration, namely stage, which makes it faster than OMP to converge. Regularized orthogonal matching pursuit (ROMP) is a modified form of OMP which does not possess a threshold value

for sparsity level; instead it selects the columns having similar dot products with the residual vector. Despite the fact that these methods are able to converge in very short runtime, they exhibit some challenges, e.g., they do not guarantee for a sparse solution [37-39].

- Convex optimization techniques replace ℓ_0 “norm” with l_1 -norm, which converts the inverse problem into a constrained convex optimization problem, hence, it can be solved by exploiting standard optimization tools [35]. Alternating direction method of multipliers (ADMM) is one possible approach and has been used for various imaging problems [40-43]. It is a form of augmented Lagrangian method (ALM) which handles solution of the optimization problem more efficiently by splitting it into smaller components. ADMM splits primal variables, augments the Lagrangian of the optimization problem (as in method of multipliers) and carries out iterative variable minimization steps. There also exist split augmented Lagrangian shrinkage algorithm (SALSA) [43-44] and constrained-SALSAs (C-SALSA-1 and C-SALSA-2) [41]. These techniques transform the unconstrained expression of the problem into a constrained one by performing variable splitting and using an ALM, specifically ADMM.

The literature also contains other algorithmic approaches such as Bayesian framework [45-46], non-convex optimization [47], and brute force [48]. However, they are not covered in the scope of this work. Non-convex optimization generally does not have theoretical guarantees. Brute force is only applicable for small scale inverse problems, although it is algorithmically correct for all cases.

All reconstruction algorithms, including the sparsity-based ones, attempt to solve the inverse problem through successive solutions of the forward problem and each forward problem solution step corresponds to a matrix-vector multiplication. As the dimensions of the imaging domain gets larger, number of the point scatterers increases, therefore, computational complexity of the forward problem increases. This also increases the run-time and limits the application of the algorithms unless a

fast matrix-vector multiplication method is introduced. When the forward problem is computed directly, the operation count and memory requirement are respectively proportional to $O(IN^2)$ and $O(N^2)$, where N is the number of unknowns and I is the iteration count. Note that some algorithms include multiple forward problem computations within each iteration, which multiplies the computational complexity. However, by applying some efficient tools for computation of the forward problem, significant reduction can be acquired for the runtime and memory requirement per iteration. In the literature, these tools are referred to as “fast algorithms”. “Conjugate gradient – fast Fourier transform” and “fast multipole method” are widely used fast algorithms. The former algorithm is briefly mentioned below only for completeness of the literature review, whereas the latter is studied throughout the thesis.

- Conjugate Gradient – Fast Fourier Transform (CG-FFT) was the first method developed for accelerating the computation of forward problems, especially in the field of computational electromagnetics. Although its simple structure yields an efficient solution, the range of its applications is limited due to the requirement of staircase approximation for geometrical modeling [49]. Later, precorrected-FFT [50] and its variants [51] are developed to eliminate this approximation. These methods perform very effectively on planar and inhomogeneous objects, reducing the complexity to $O(N \log N)$. However, they lack efficiency for the case of impenetrable objects [52].
- Fast Multipole Methods (FMM) is another method that accelerates the matrix-vector multiplication, which reduces the computational complexity and can be used for solving large scale scattering problems with less memory requirement and runtime per iteration. FMM was first proposed by Rokhlin and its usage is extended for several electromagnetic scattering problems [53-54]. In contrast to conventional approaches such as method of moments (MOM), the interactions between the source and observation locations are calculated in a group-by-group manner. Since only the interactions between neighboring locations are calculated directly and stored, FMM reduces the

memory usage. For groups that are sufficiently far away from each other, group interactions are calculated by translating the total effect of the group to the center of the other group by using the addition theorem, which provides significant reduction in the operation count. Implementation of FMM reduces the memory requirement and CPU time to $O(IN^{3/2})$. Multi-level fast algorithm (MLFMA) is later developed in order to further reduce the computational complexity to $O(N \log N)$ [55-57]. The details about the implementation of the FMM are discussed in Chapter 4, while its application to near-field MIMO radar imaging problems are given in Chapters 4, 5 and 6.

CHAPTER 3

MIMO ARRAYS AND FORWARD PROBLEM

3.1 Literature Review

3.1.1 MIMO Array

The MIMO array concept was first introduced by Von Ramm et al. in 1975 for the practice of ultrasonic imaging [59]. By the use of different inter-element spacing for transmitting and receiving sub-arrays, they showed that grating lobes of the sub-arrays can be eliminated. In [60], Cooley and Robinson suggested a technique to avoid redundancy of synthetic focus datasets obtained using conventional aperture designs. By replacing two-way imaging system with a one-way array of virtual elements, it was demonstrated that complete subsets containing all information required for the image reconstruction can be acquired. In [61], a synthetic aperture ultrasonic imaging system containing a two-way sparse array topology, namely co-array, is patented. In [62], Lockwood et al. demonstrated a new method to design sparse periodic arrays by optimizing aperture functions of transmitting/receiving sub-arrays. Ahmet et al. [63] and Yang et al. [64] studied on different MIMO array topologies and compared their performances for UWB short-range applications. Zhuge et al. proposed a 2-D curvilinear structure, which performs better than similar configurations having the same number of antennas and aperture size [65]. In [11], an optimal design approach for MIMO array is presented by specifying the reconstruction quality as an optimization criterion.

3.1.2 MIMO Radar

Usage of MIMO arrays in modern radar systems was first mentioned by Fishler et al. in 2004 [66]. Their publication established a standard approach for radar systems and became a beacon for the researchers working in the field of radar engineering. The authors proposed a MIMO radar architecture that comprises a transmitting sub-array of widely-spaced antenna elements, whereas the elements of receiving sub-array is placed tightly. In this way, each transmitting element is able to illuminate the targets in a different angle so that the problem of target scintillation (a physical phenomenon where radar cross section of the target changes rapidly as it moves) is avoided or reduced significantly. Later, the same authors compared the MIMO radar system with conventional radar systems in order to emphasize its apparent advantages, leading to strong interest in this new approach. In [67-71], MIMO radar systems with colocated antenna elements are considered. In [72], Xu and Li proposed a MIMO radar system having well-separated sub-arrays with tightly-spaced antenna elements and investigated advantages of this configuration.

3.1.3 MIMO Radar Imaging Applications

In the last two decades, as the radar has been applied to various imaging applications, MIMO radar systems have started to make ground among them. In 2006, Bliss and Forsythe suggested using MIMO radar for imaging purposes for the first time and employed it to detect cancerous breast tissue [73]. Chen et al. followed this idea and further developed it for the detection and classification of breast lesions [74]. MIMO radar has also been integrated to SAR imaging systems. In [75], an early concept of MIMO-SAR is used for an interferometry application. In [76,77], detection of moving targets and SAR spotlight mode are respectively investigated. [1] introduces a MIMO-SAR-based imaging system for concealed weapon systems and extends the usage of MIMO radar systems for security applications. Literature also contains many other application fields of MIMO radar imaging such as sub-surface

surveillance [78,79], automotive [80], anti-personnel mine detection [81], tsunami wave monitoring [82], through-wall sensing [83], water accumulation monitoring in human body [84], etc.

As the growing literature suggests, MIMO radar technology, in conjunction with large operational bandwidth, has strong potential for the development of state-of-the-art of modern radar, specifically in remote sensing applications.

3.2 Imaging Geometry

Fig. 3.1 sketches imaging geometry for the MIMO array-based near field imaging radar, which is used throughout this thesis. In this configuration, the backscattered data is collected by sequential transmission from each transmitting antenna in association with simultaneous reception by all receiving antennas. A two dimensional plus-shaped MIMO array illuminates the target(s), which is placed in the near field of the antenna array.

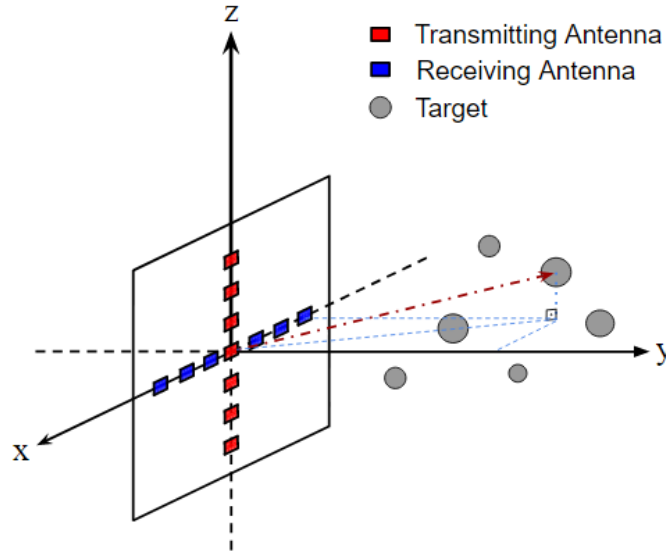


Figure 3.1. Plus-shaped 2-D planar MIMO array.

The array is placed at $y = 0$ plane. The receiving antennas are positioned along the x -axis and their locations are denoted by $(x_R, 0, z_R)$, while the transmitting antennas

are placed along the z -axis and their locations are denoted by $(x_T, 0, z_T)$, composing a plus-shaped MIMO radar. The received signal is represented as a function of four spatial coordinates x_R, z_R, x_T, z_T and fast time t .

The targets residing in the imaged volume are approximated by a cloud of point scatterers and their reflectivity characteristics are distributed discretely on these scatterers. Although imaging problem is fundamentally an electromagnetic scattering phenomenon with vector nature, we use a simple scalar model based on Born approximation. According to this approximation, each point scatterer directly reflects the transmitted signal, neglecting their interaction with the other scatterers. Thus, contribution from multiple reflections between the point scatterers are not included in the received signal [125]. In the literature, this approximation is successfully adopted for wide variety of radar imaging applications [1,2,12,17,64,65,122]. The received signal at the position of any receiving antenna due to a point scatterer located in the imaging scene is given as

$$s(x_T, z_T, x_R, z_R, t) = \iiint \frac{1}{4\pi R_T R_R} f(x, y, z) p\left(t - \left[\frac{R_T}{c} + \frac{R_R}{c}\right]\right) dx dy dz \quad (3.1)$$

where $p(t)$ is the transmitted pulse in time domain, c is the speed of light, and $f(x, y, z)$ is the complex-valued three dimensional reflectivity distribution function defined on the image volume. The distances from the transmitting and the receiving antennas to any point (x, y, z) in the image volume are denoted by R_T and R_R , respectively, and they are given by

$$R_T = \sqrt{(x_T - x)^2 + y^2 + (z_T - z)^2}, \quad (3.2)$$

$$R_R = \sqrt{(x_R - x)^2 + y^2 + (z_R - z)^2}. \quad (3.3)$$

The time domain received signal can be expressed in temporal frequency domain by applying Fourier transform to (3.1), which is given as

$$s(x_T, z_T, x_R, z_R, k) = 4\pi p(k) \iiint \frac{e^{-jkR_T}}{4\pi R_T} \frac{e^{-jkR_R}}{4\pi R_R} f(x, y, z) dx dy dz \quad (3.4)$$

where $p(k)$ is the Fourier transform of the transmitted pulse with $k = \omega/c$ being the wavenumber that is related to the temporal frequency by $\omega = 2\pi f$.

Since the reconstruction process will be carried out digitally, a discrete forward model is required. Here, we use a predefined grid to discretize the imaging volume and define the 3-D reflectivity field in terms of voxels. In the literature, one can also find grid-free reconstruction methods, specifically for direction of arrival estimation [133,134]. The continuous models given in (3.1) and (3.4) can be written in a discrete form as

$$\tilde{s}_{T_m, R_n, q, k_l} = 4\pi p(k_l) \sum_{q=1}^{N_V} \frac{e^{-jk_l R_{T_m, q}}}{4\pi R_{T_m, q}} \frac{e^{-jk_l R_{q, R_n}}}{4\pi R_{q, R_n}} f_q \quad (3.5)$$

where $\tilde{s}_{T_m, R_n, q, k_l}$ is the received signal due to the q^{th} voxel obtained at the l^{th} frequency step using the pair of the m^{th} transmitting antenna and the n^{th} receiving antenna. The transmitting antennas radiate N_F discrete frequencies, which are equally spaced by frequency step of Δf , in the operational bandwidth. $R_{T_m, q}$ denotes the distance from the m^{th} transmitting antenna to the center of the q^{th} voxel and R_{q, R_n} denotes the distance from the center of the q^{th} voxel to the n^{th} receiving antenna. Furthermore, it is assumed that there are N_T transmitting, N_R receiving antennas, and N_V voxels.

Recall that $\tilde{s}_{T_m, R_n, q, k_l}$ in (3.5) neglects the multiple reflections among the voxels. The transmitted pulse is assumed to be directly reflected by each voxel to the corresponding receiving antenna without any contribution from the rest of the voxels.

The discrete model constitutes a linear system as given in (3.6). The reflectivity values belonging to voxels are stacked into the vector \mathbf{f} in some lexicographic order and the measurements are listed in the same order in the right-hand-side vector $\tilde{\mathbf{s}}$. The matrix $\mathbf{A} \in \mathbb{C}^{M \times N}$ is the observation matrix and its total number of rows M is equal to $N_T \times N_R \times N_F$, whereas the number of columns N is equal to N_V . The expanded form of the linear system is also given in (3.7).

$$\mathbf{A}\mathbf{f} = \tilde{\mathbf{s}} \quad (3.6)$$

$$4\pi \begin{bmatrix} p(k_1) \frac{e^{-jk_1 R_{T_1,1}}}{4\pi R_{T_1,1}} \frac{e^{-jk_1 R_{1,R_1}}}{4\pi R_{1,R_1}} & \dots & \dots & p(k_1) \frac{e^{-jk_1 R_{T_1,N_V}}}{4\pi R_{T_1,N_V}} \frac{e^{-jk_1 R_{N_V,R_1}}}{4\pi R_{N_V,R_1}} \\ \vdots & \vdots & \vdots & \vdots \\ p(k_1) \frac{e^{-jk_1 R_{T_1,1}}}{4\pi R_{T_1,1}} \frac{e^{-jk_1 R_{1,R_{N_R}}}}{4\pi R_{1,R_{N_R}}} & \dots & \dots & p(k_1) \frac{e^{-jk_1 R_{T_1,N_V}}}{4\pi R_{T_1,N_V}} \frac{e^{-jk_1 R_{N_V,R_{N_R}}}}{4\pi R_{N_V,R_{N_R}}} \\ \vdots & \vdots & \vdots & \vdots \\ p(k_1) \frac{e^{-jk_1 R_{T_{N_T},1}}}{4\pi R_{T_{N_T},1}} \frac{e^{-jk_1 R_{1,R_{N_V}}}}{4\pi R_{1,R_{N_V}}} & \dots & \dots & p(k_1) \frac{e^{-jk_1 R_{T_{N_T},S}}}{4\pi R_{T_{N_T},S}} \frac{e^{-jk_1 R_{S,R_{N_R}}}}{4\pi R_{S,R_{N_R}}} \\ \vdots & \vdots & \vdots & \vdots \\ p(k_l) \frac{e^{-jk_l R_{T_{N_T},1}}}{4\pi R_{T_{N_T},1}} \frac{e^{-jk_l R_{1,R_{N_V}}}}{4\pi R_{1,R_{N_V}}} & \dots & \dots & p(k_l) \frac{e^{-jk_l R_{T_{N_T},S}}}{4\pi R_{T_{N_T},S}} \frac{e^{-jk_l R_{S,R_{N_R}}}}{4\pi R_{S,R_{N_R}}} \end{bmatrix} \begin{bmatrix} f_1 \\ \vdots \\ \vdots \\ f_{N_V} \end{bmatrix} = \begin{bmatrix} \tilde{s}_1 \\ \vdots \\ \vdots \\ \tilde{s}_M \end{bmatrix} \quad (3.7)$$

In an iterative solution to (3.7), $N_T \times N_R \times N_F \times N_V$ operations must be performed for the solution of each forward problem. Standard iterative linear system solvers consist of multiple forward problems within their structures. As the dimensions of the system increases, the solution becomes quite inefficient due to the requirements for excessive amount of computational resources and memory.

3.2.1 Point Spread Function (PSF)

Point spread function is a significant figure of merit that characterizes the resolving performance of an imaging system. It describes the response of the system to a point scatterer and provides information about the resolution limit of the system.

As shown in Fig. 3.2, a single point scatterer is placed 55 cm away from the center of the array, which is composed of 30 transmitting and 30 receiving antennas. The separation between the antennas elements is 2.5 cm, and thus the total aperture size of the array is 72.5 cm \times 72.5 cm. Operational bandwidth ranges from 7 GHz to 13 GHz with steps of 1 GHz consisting of 7 frequencies. The imaged space is scanned along a linear path from $x = -5$ cm to $x = +5$ cm, with 51 spatial steps, so, the PSF of the plus-shaped MIMO array along x -axis is obtained. Given these

specifications, the linear system (3.7) is implemented and solved directly. Fig. 3.3 depicts the reconstructed PSF, which is sinc-shaped.

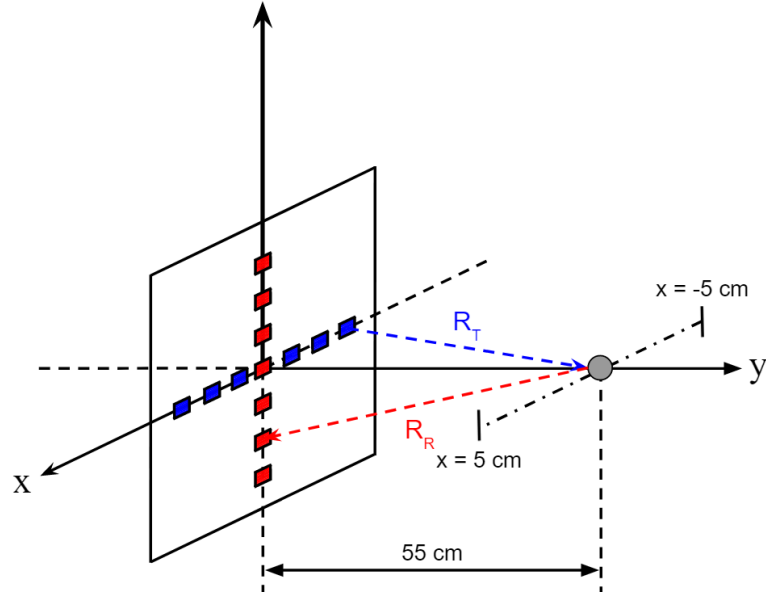


Figure 3.2. Single point scatterer illuminated by plus-shaped MIMO array.

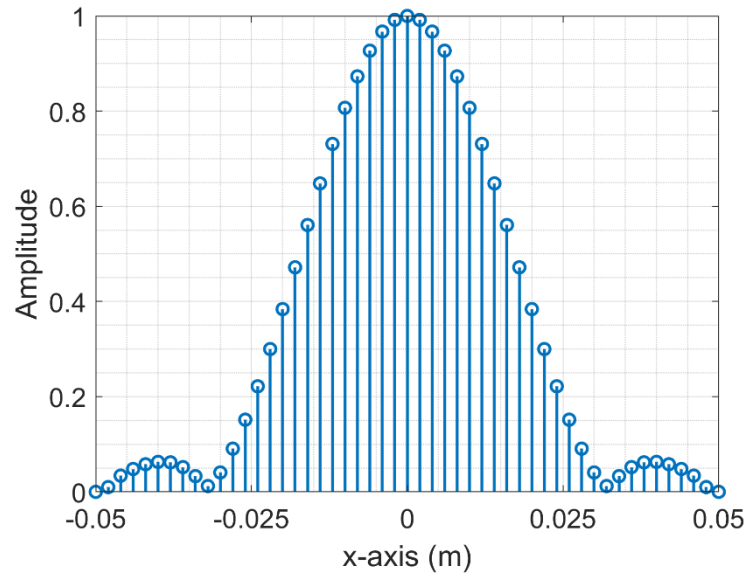
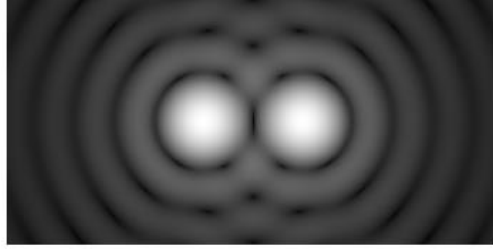


Figure 3.3. PSF of the plus-shaped MIMO array along x -axis.

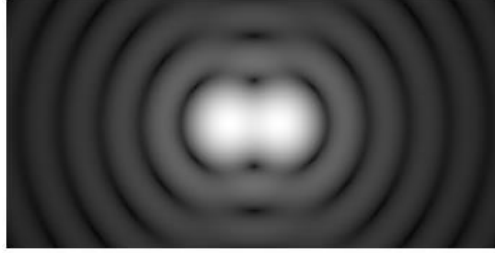
3.2.2 Down-Range and Cross-Range Resolutions

The minimum resolvable detail that can be captured by the imaging system is estimated by Rayleigh criterion. According to this criterion, two point sources placed in close proximity of each other are regarded as resolvable when the first minimum of the response of first point source coincides with the maximum of the second one. If the spacing between the point sources is greater than the minimum resolvable distance, they are well-resolved and if they are closer, they are unresolved. Note that this criterion applies when the point sources are of equal strength. Fig. 3.4 depicts all cases for diffraction patterns generated by two point light sources passing through a circular aperture, as suggested by Lord Rayleigh.

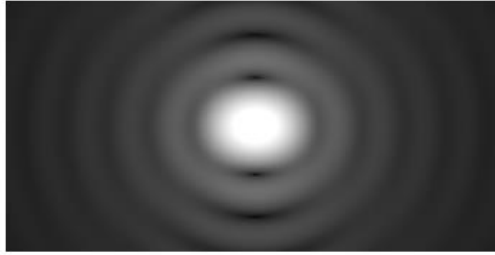
This phenomenon can be demonstrated by two imaging scenarios, as shown in Fig. 3.5(a) and 3.5(b). In both scenarios, the same imaging configuration is adopted as the one used for the PSF demonstration above. In the first scenario, the point scatterers are separated by 2.5 cm, while they are separated by 6 cm in the second scenario. The imaged space in the first scenario is discretized by 71 spatial steps from $x = -4$ cm to $x = +4$ cm, whereas 81 spatial steps from $x = -8$ cm to $x = +8$ cm are used for the second scenario. Again, the linear system (3.7) is implemented for both of the scenarios, they are solved directly. The reconstructed images are given in in Fig. 3.5(c) and 3.5(d). It can be seen that the minimum resolvable distance (or the Rayleigh criterion) that the MIMO array can provide is around 2.5 cm. Above this distance, the point scatterers appear to be well-resolved while they are not resolved otherwise.



(a)



(b)



(c)

Figure 3.4. Airy diffraction patterns generated by light from two point sources passing through a circular aperture. (a) Well-resolved case, (b) sources are at a distance determined by Rayleigh criterion, and (c) unresolved case.

This result can also be mathematically supported. Theoretical cross-range resolution is determined by the wavelength at the center frequency λ_c , distance to the target R , and aperture width of the array in orthogonal dimensions as

$$\delta_h = \frac{\lambda_c R}{L_{T,h} + L_{R,h}} \quad (3.14)$$

and

$$\delta_v = \frac{\lambda_c R}{L_{T,v} + L_{R,v}}. \quad (3.15)$$

$L_{T,h}$ and $L_{R,h}$ are widths of the transmitting and receiving arrays along horizontal axis, whereas $L_{T,v}$ and $L_{R,v}$ are widths along vertical axis. The down-range resolution, on the other hand, is determined by speed of light and the operational bandwidth as

$$\delta_y = \frac{c}{B}. \quad (3.16)$$

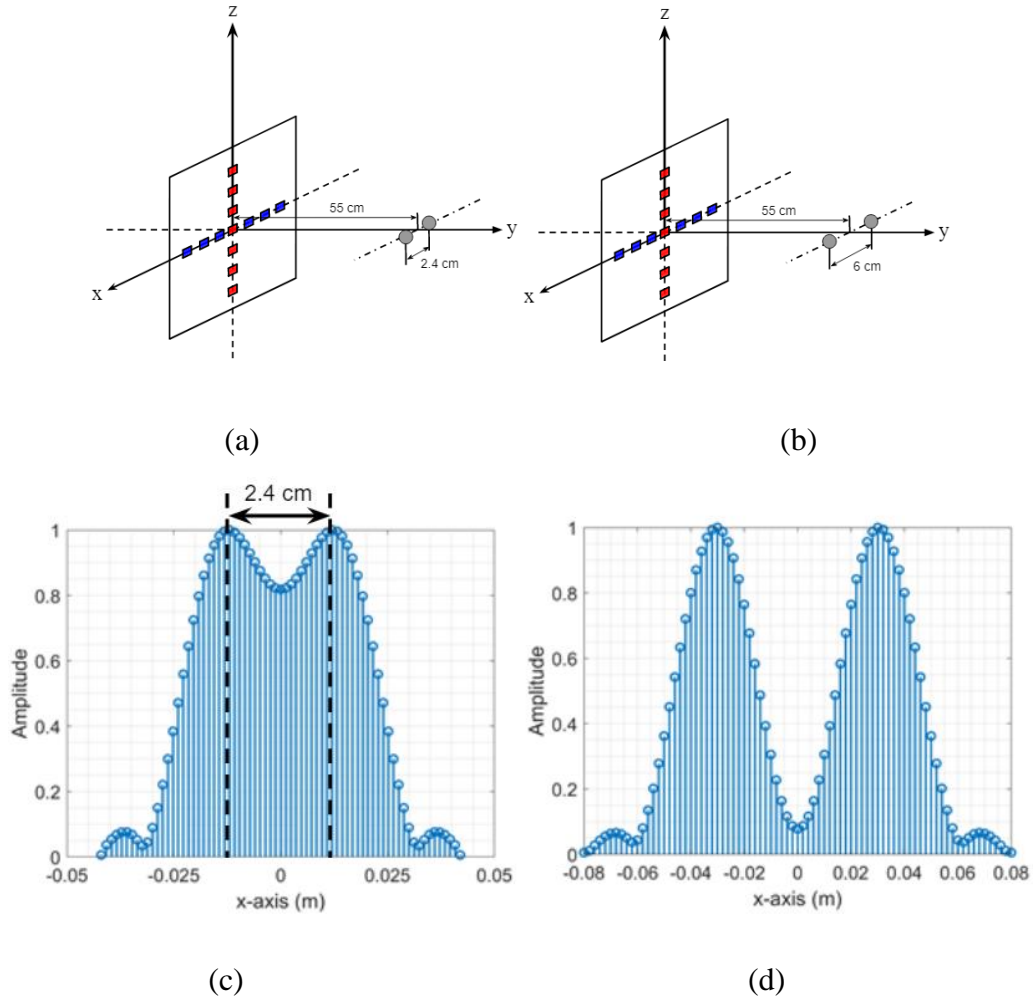


Figure 3.5. Imaging environment with (a) 2.4 cm spacing between the point scatterers and (b) 6 cm spacing between the point scatterers. (c) Rayleigh criterion and (d) well-resolved case for the plus-shaped MIMO array.

For the radar system specifications given in the previous subsection, the cross-range resolutions in the orthogonal directions can be calculated as 2.4 cm, which is consistent with the obtained Rayleigh criterion depicted in Fig. 3.6(c). The down-range resolution is calculated as 2.5 cm at the center frequency of the operational bandwidth.

CHAPTER 4

FAST MULTIPOLE METHOD

Direct computation of a forward problem within an iterative solver requires $O(IN^2)$ operation count and $O(N^2)$ memory usage. Therefore, as the dimensions of the linear system (e.g. number of transceiver pairs, number of voxels) increases, computational complexities are encountered in solving the imaging problem. These complexities motivated the researchers to find more efficient computation methods.

In this chapter, the fast multipole method is described, which is capable of reducing the complexity of the problem solution by accelerating it with less memory usage. This method was first proposed by Rokhlin and Greengard for reducing the complexity of classic N -body problem, which was initially developed for the evaluation of potential fields and gravitational forces in systems with large numbers of particles [85,86]. The authors' approach was to rapidly evaluate the gravitational potential functions of a group of nearby particles by rewriting them in terms of multipole expansions and combining them into a single function belonging to that entire group. Thus, the interaction between that group and any other particle that is sufficiently away from that group can be calculated with the use of the multipole expansions. In other words, the FMM groups the nearby particles and carries out the calculations by treating them as if they form a single object [86].

We can consider the imaging problem in the same context, i.e., observation matrix of the linear system can be viewed as one type of N -body problem, whose entries represent the interactions between the transceiver pairs and the voxels of the discretized imaging space. Despite the fact that the observation matrix is full, the amplitude of the interaction diminishes with the increasing distance between the interacting parts, which makes the group-by-group approach of the FMM very reasonable. This chapter will mathematically show that the FMM can be applied to

a near-field MIMO imaging problem, enabling faster matrix-vector computation in an iterative solver and reducing storage requirement. This will allow us to solve larger imaging problems that could not be solved with standard computational resources.

4.1 The FMM Formulation

The FMM formulation starts with using addition theorem to express the three dimensional Green's function in terms of multipole expansions.

4.1.1 Addition Theorem

Three dimensional Green's function with $e^{j\omega t}$ time convention ($\omega = 2\pi f$ and f is operating frequency) is given as

$$G(\mathbf{r}, \mathbf{r}') = \frac{e^{-jk|\mathbf{r}-\mathbf{r}'|}}{4\pi|\mathbf{r}-\mathbf{r}'|} \quad (4.1)$$

where \mathbf{r} and \mathbf{r}' respectively represent field and source vectors. If a small offset vector \mathbf{x} is added to the field point, (4.1) can be rewritten as

$$\frac{e^{-jk|\mathbf{r}-\mathbf{r}'+\mathbf{x}|}}{4\pi|\mathbf{r}-\mathbf{r}'+\mathbf{x}|} = \frac{e^{-jk|\mathbf{R}+\mathbf{x}|}}{4\pi|\mathbf{R}+\mathbf{x}|} \quad (4.2)$$

where $\mathbf{R} = \mathbf{r} - \mathbf{r}'$. Provided that $|\mathbf{x}| < |\mathbf{R}|$, the addition theorem can be written as

$$\frac{e^{-jk|\mathbf{R}+\mathbf{x}|}}{4\pi|\mathbf{R}+\mathbf{x}|} = -\frac{jk}{4\pi} \sum_{l=0}^{\infty} (-1)^l (2l+1) j_l(k|\mathbf{x}|) h_l^{(2)}(k|\mathbf{R}|) P_l(\hat{\mathbf{x}} \cdot \hat{\mathbf{R}}) \quad (4.3)$$

where $j_l(x)$ and $P_l(x)$ denote the spherical Bessel function and the Legendre polynomial of order l , respectively. In (4.3), $h_l^{(2)}(x)$ is the spherical Hankel function of the second kind and order l , given as

$$h_l^{(2)}(x) = \sqrt{\frac{\pi}{2x}} H_{l+\frac{1}{2}}^{(2)}(x). \quad (4.4)$$

Note that (4.3) can be interpreted as a wave radiating from a source point, which is displaced from its original location by a small vector \mathbf{x} . Inserting the elementary identity that converts (4.3) into a surface integral on a unit sphere [57]

$$4\pi j^l(-j_l)(k|\mathbf{x}|)P_l(\hat{\mathbf{x}} \cdot \hat{\mathbf{R}}) = \oint e^{-jk\hat{\mathbf{k}} \cdot \mathbf{x}} P_l(\hat{\mathbf{k}} \cdot \hat{\mathbf{R}}) d^2\mathbf{k} \quad (4.5)$$

where $\hat{\mathbf{k}}$ is unit vector in radial direction, we obtain

$$\frac{e^{-jk|\mathbf{R}+\mathbf{x}|}}{4\pi|\mathbf{R}+\mathbf{x}|} = \frac{-jk}{(4\pi)^2} \oint e^{-jk\hat{\mathbf{k}} \cdot \mathbf{x}} \sum_{l=0}^{\infty} (-j)^l (2l+1) h_l^{(2)}(k|\mathbf{R}|) P_l(\hat{\mathbf{k}} \cdot \hat{\mathbf{R}}) d^2\mathbf{k} \quad (4.6)$$

where integration and summation are interchanged which is valid as long as the summation is truncated at some finite order N . When the truncation is applied, following approximation is obtained.

$$\frac{e^{-jk|\mathbf{R}+\mathbf{x}|}}{4\pi|\mathbf{R}+\mathbf{x}|} = \oint e^{-jk\hat{\mathbf{k}} \cdot \hat{\mathbf{x}}} T_N(k, \hat{\mathbf{k}}, \mathbf{R}) d^2\mathbf{k} \quad (4.7)$$

where $T_N(k, \hat{\mathbf{k}}, \mathbf{R})$ is called the translation function, and has the form

$$T_N(k, \hat{\mathbf{k}}, \mathbf{R}) = \frac{-jk}{(4\pi)^2} \sum_{l=0}^N (-j)^l (2l+1) h_l^{(2)}(k|\mathbf{R}|) P_l(\hat{\mathbf{k}} \cdot \hat{\mathbf{R}}). \quad (4.8)$$

This function converts outgoing waves at a source point into incoming spherical waves at a field point.

4.1.2 Wave Translation

As illustrated in Fig. 4.1, $\mathbf{R} = \mathbf{r} - \mathbf{r}'$ can be expressed as a sum of three vectors: $\mathbf{r} - \mathbf{r}' = \mathbf{v}_1 + \mathbf{w} + \mathbf{v}_2$. Using this expression, we obtain

$$\frac{e^{-jk|\mathbf{r}-\mathbf{r}'|}}{4\pi|\mathbf{r}-\mathbf{r}'|} = \oint e^{-jk\hat{\mathbf{k}} \cdot (\mathbf{v}_1 + \mathbf{v}_2)} T_N(k, \hat{\mathbf{k}}, \mathbf{w}) d^2\mathbf{k} \quad (4.9)$$

where

$$T_N(k, \hat{\mathbf{k}}, \mathbf{w}) = \frac{-jk}{(4\pi)^2} \sum_{l=0}^N (-j)^l (2l+1) h_l^{(2)}(k|\mathbf{w}|) P_l(\hat{\mathbf{k}} \cdot \hat{\mathbf{w}}). \quad (4.10)$$

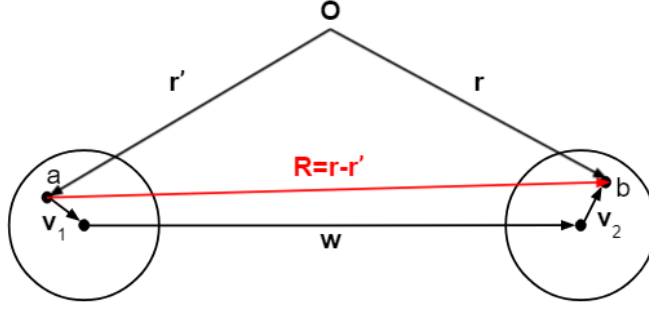


Figure 4.1. Expression of $\mathbf{r} - \mathbf{r}'$ as a sum of three vectors.

(4.10) shows that the translation function depends only on \mathbf{w} , which is a very significant result. It tells us that if \mathbf{r} and \mathbf{r}' is displaced by very small vectors (\mathbf{v} and \mathbf{w} , respectively), the translation function remains unchanged. Hence, interaction between any two points in the computation domain can be carried out using the same translation function. Rewriting (4.9) in a more compact form as

$$\frac{e^{-jk|\mathbf{r}-\mathbf{r}'|}}{4\pi|\mathbf{r}-\mathbf{r}'|} = \oint\!\!\!\oint A(\mathbf{r}', \hat{\mathbf{k}}) T_N(k, \hat{\mathbf{k}}, \mathbf{w}) D(\mathbf{r}, \hat{\mathbf{k}}) d^2\mathbf{k} \quad (4.11)$$

where $A(\mathbf{r}', \hat{\mathbf{k}})$ is the aggregation function defined at the source point \mathbf{r}' as

$$A(\mathbf{r}', \hat{\mathbf{k}}) = e^{-jk\hat{\mathbf{k}}\cdot\mathbf{v}_1} \quad (4.12)$$

and $D(\mathbf{r}, \hat{\mathbf{k}})$ is the disaggregation function defined at the observation point \mathbf{r} as

$$D(\mathbf{r}, \hat{\mathbf{k}}) = e^{-jk\hat{\mathbf{k}}\cdot\mathbf{v}_2}. \quad (4.13)$$

When \mathbf{r} or \mathbf{r}' is displaced to another location, only aggregation and disaggregation functions have to be calculated. Sum of the three dimensional Green's functions due to multiple sources at points \mathbf{r}'_n can be evaluated at field point \mathbf{r} by

$$\sum_{n=1}^{N_S} \frac{e^{-jk|\mathbf{r}-\mathbf{r}'_n|}}{4\pi|\mathbf{r}-\mathbf{r}'_n|} = \oint\!\!\!\oint D(\mathbf{r}, \hat{\mathbf{k}}) T_N(k, \hat{\mathbf{k}}, \mathbf{w}) \sum_{n=1}^{N_S} A_n(\mathbf{r}', \hat{\mathbf{k}}) d^2\mathbf{k} \quad (4.14)$$

where N_S is the number of source points and the aggregation functions $A_n(\mathbf{r}', \hat{\mathbf{k}})$ are

$$A_n(\mathbf{r}', \hat{\mathbf{k}}) = e^{-jk\hat{\mathbf{k}}\cdot\mathbf{v}_n}. \quad (4.15)$$

The expression given in (4.14) is what enables the fast matrix-vector product computation. The radiated waves from all source points are aggregated at the group center (e.g., geometric center). This aggregated wave is then carried to another group center that is far enough ($|\mathbf{x}| < |\mathbf{R}|$) by translation function. Finally, the translated wave is multiplied with the disaggregation function and integrated over unit sphere to find local field at point \mathbf{b} , which yields the desired sum.

4.1.3 Truncation Number

Accurate evaluation of (4.9) depends on truncating the transfer function at some limit N , which is equal to the number of multipoles that will be included in the calculations. It is a source of numerical error in the FMM, since the exact mathematical expression of addition theorem is an infinite sum.

In [54], Rokhlin defined the following formula to determine N for single precision computations:

$$N = kD + 5 \log(kD + \pi) \quad (4.16)$$

whereas for the double precision

$$N = kD + 10 \log(kD + \pi) \quad (4.17)$$

where $D = |\mathbf{x}|$ from (4.9). Another way for the control of truncation error is to utilize excess bandwidth formula (EBF). Chew et al. [57] and Song and Chew [87] proposed the following formula to determine the truncation number:

$$N \approx kD + 1.8(d_0)^{2/3}(kD)^{1/3}, \quad (4.18)$$

where, d_0 is the desired number of digits for accuracy.

4.1.4 Integration

The integration in (4.11) over the unit sphere can be calculated numerically by using quadrature rule, with sufficient number of points in elevation (θ) and azimuth (ϕ) dimensions. In this way, aggregation, disaggregation and translation functions are computed and stored at discrete angles. Optimum number of points and the quadrature rule should be determined by the number of spherical harmonic included in (4.11).

The spherical harmonic coefficients a_n^m can be calculated by the following integral:

$$a_n^m = \int_0^{2\pi} \int_0^\pi f(\theta, \phi) Y_n^{m*}(\theta, \phi) \sin\theta d\theta d\phi, \quad (4.19)$$

which can be rewritten as

$$a_n^m = \int_0^{2\pi} e^{-jm\phi} d\phi \int_0^\pi f(\theta, \phi) P_n^m(\cos\theta) \sin\theta d\theta. \quad (4.20)$$

In [126], it is proposed that integration of a function of form (4.20) can be evaluated optimally by N -point Gauss-quadrature rule in θ , while ϕ can be sampled uniformly by $2N + 1$ points.

4.2 FMM for Near-Field MIMO Imaging Problem

As shown in (3.7), the entries of the system matrix obtained at l^{th} frequency step are in the form of

$$4\pi p(k_l) \frac{e^{-jk_l R_{T_{m,q}}} e^{-jk_l R_{q,R_n}}}{4\pi R_{T_{m,q}} 4\pi R_{q,R_n}}$$

which are product of two three-dimensional Green's functions. This is the key factor that allows a two-stage FMM-applied solution for the forward problem. Here, the first three-dimensional Green's function represents the path that the transmitted signal traverses between the transmitting antenna and the target and it is treated by the first stage of FMM. The second three-dimensional Green's function represents

the propagation of the reflected signal back to the receiving antenna and the second stage of the FMM is applied to this part. The stages are illustrated below in Fig. 4.2.

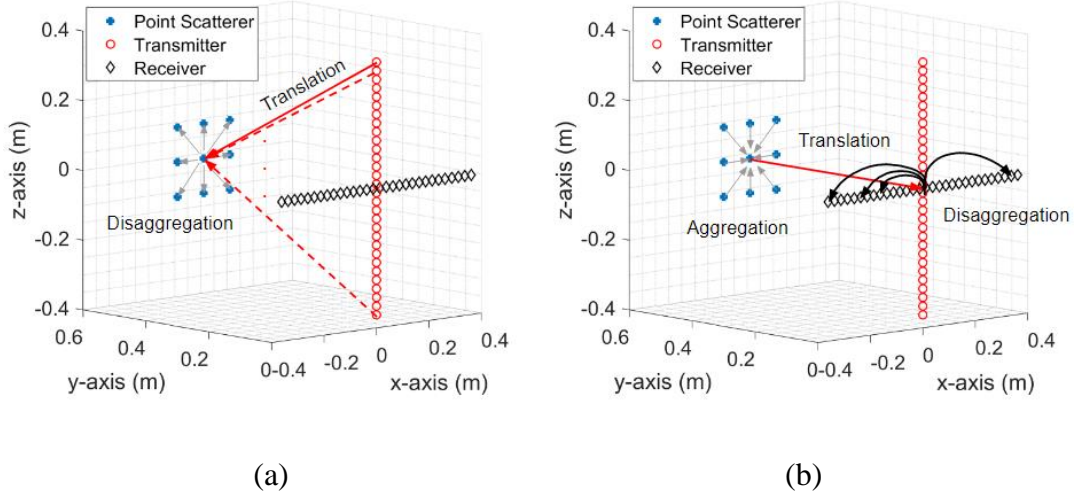


Figure 4.2. Two-stage FMM. a) 1st stage and b) 2nd stage [127].

4.2.1 The First Stage

Considering that only one transmitting antenna operates at a time in our imaging model, the aggregation step is not included in this stage, as opposed to classical FMM application. The transmitted signals from each transmitting antenna are carried to the geometric center of the scatterers in the imaged space by separate translation functions. Then, the translated signals are disaggregated to each voxel position. This stage can be represented by excluding aggregation function from (4.11) as

$$\tilde{S}_{T_m,q,k_l,FMM} = \oint\!\!\!\oint T_{N,m}(k_l, \hat{\mathbf{k}}, \mathbf{R}_{Tm}) D_q(k_l, \hat{\mathbf{k}}, \mathbf{r}_q) f_q d^2\mathbf{k}, \quad (4.21)$$

where

$$T_{N,m}(k_l, \hat{\mathbf{k}}, \mathbf{R}_{Tm}) = \frac{-jk}{(4\pi)^2} \sum_{l=0}^N (-j)^l (2l+1) h_l^{(2)}(k|\mathbf{R}_{Tm}|) P_l(\hat{\mathbf{k}} \cdot \hat{\mathbf{R}}_{Tm}) \quad (4.22)$$

$$D_q(k_l, \hat{\mathbf{k}}, \mathbf{r}_q) = e^{-jk_l \hat{\mathbf{k}} \cdot \mathbf{r}_q}. \quad (4.23)$$

In (4.22), R_{Tm} is the distance from m^{th} transmitting antenna to the geometric center of the image domain and r_q is the distance from q^{th} voxel to that center.

Total number of operations required in this stage is $N_T \times N_V \times N_F$, where N_T , N_V , N_F respectively denote number of transmitting antennas, number of voxels, and number of frequency steps as defined separately in Section 3.2, since (4.21) must be repeated for each transmitting antenna and voxel position alongside with each frequency step.

4.2.2 The Second Stage

Since multiple reflections between the voxels are ignored, scattered signals can be aggregated at the center of the image volume using aggregation function. The aggregated scattered signal is then carried to the geometric center of the receiving sub-array (center of the plus-shaped MIMO array in our case) with the use of a common translation function. This stage can mathematically be expressed as follows

$$\tilde{s}_{r_q, R_r, r_n, k_l, FMM} = \oint A_q(k_l, \hat{\mathbf{k}}, \mathbf{r}_q) T_N(k_l, \hat{\mathbf{k}}, \mathbf{R}_r) D_n(k_l, \hat{\mathbf{k}}, \mathbf{r}_n) f_q d^2 \mathbf{k} \quad (4.23)$$

where

$$A_q(k_l, \hat{\mathbf{k}}, \mathbf{r}_q) = e^{ik_l \hat{\mathbf{k}} \cdot \mathbf{r}_q}, \quad (4.24)$$

$$D_n(k_l, \hat{\mathbf{k}}, \mathbf{r}_n) = e^{ik_l \hat{\mathbf{k}} \cdot \mathbf{r}_n}, \quad (4.25)$$

and

$$T_N(k_l, \hat{\mathbf{k}}, \mathbf{R}_r) = \frac{-jk}{(4\pi)^2} \sum_{l=0}^N (-j)^l (2l+1) h_l^{(2)}(k|\mathbf{R}_r|) P_l(\hat{\mathbf{k}} \cdot \hat{\mathbf{R}}_r). \quad (4.26)$$

In (4.23), R_r is the distance from the geometric center of the image volume to the geometric center of the receiving sub-array and r_n is the displacement from geometric center of the receiving sub-array to the n^{th} receiving antenna.

This stage takes shorter runtime than the first stage, because it involves only one translation function. (4.23) must be calculated for each voxel, receiving antenna

position, and frequency steps. Therefore, the number of calculations that must be carried out in this stage is equal to $N_V \times N_R \times N_F$, where N_R is the number of receiving antennas as defined in Section 3.2.

In an iterative solver, each iteration requires the application of the forward operator (multiplication of the observation matrix \mathbf{A} with a vector) and/or its adjoint (multiplication of \mathbf{A}^H with a vector). The above stages describe how the FMM can be adopted for the solution of the forward problem. The same method can be followed for the calculation of the adjoint operator by simply exchanging order of the stages, i.e., in the first stage, transmitted signals are aggregated at the center of the array and translated to the center of the imaged scene. Then in the second stage, the reflected signals are separately translated back to the center of the array by individual translation functions and distributed over the receiving antennas by disaggregation step.

Finally, overall operations required for the calculation of one matrix-vector multiplication is obtained as $(N_T + N_R) \times N_V \times N_F$, while direct multiplication requires $N_T \times N_R \times N_V \times N_F$ operations. This improvement results in an efficient solution for imaging problems with large array aperture in terms of CPU time and memory requirement.

Note that the developed FMM-based method does not depend on the MIMO array geometry, since it derives its efficiency from the number of antennas on the array, instead of arrangement of the sub-arrays on the aperture.

4.3 Numerical Example

A simple imaging scenario is created for evaluating performance of the FMM. A plus shaped MIMO array as shown in Fig. (4.2) is used with 30 vertically placed transmitting antennas and 30 horizontally placed receiving antennas. The overall aperture of the array is $72.5 \text{ cm} \times 72.5 \text{ cm}$ and spacing between the antennas is 2.5 cm ($\sim 0.83\lambda_c$, $f_c = 10 \text{ GHz}$). The scene contains an array of 9 point scatterers

located on a grid of 2.4 cm on each side on the $y = 55$ cm plane. Operational frequency bandwidth ranges from 7 GHz to 13 GHz with 7 frequency steps of 1 GHz. The reflectivity level of the all point scatterers are set to 1.

Table 4.1 Algorithmic steps of conjugate gradient least squares.

Conjugate Gradient Least Squares (CGLS)	
Input: $\mathbf{A} \in \mathbb{C}^{M \times N}$, $\mathbf{b} \in \mathbb{C}^M$, initial guess $\mathbf{x}_0 \in \mathbb{C}^N$, $\mathbf{tol} \in \mathbb{R}$, and maximum number of iterations $\mathbf{maxit} \in \mathbb{R}$.	
Output: an approximate solution $\mathbf{x}_{sol} \in \mathbb{C}^N$.	
$\mathbf{r}_0 = \mathbf{b} - \mathbf{A}\mathbf{x}_0$ $\mathbf{s}_0 = \mathbf{p}_0 = \mathbf{A}^H \mathbf{r}_0$ $\gamma_0 = \ \mathbf{s}_0\ ^2$ for $i = 0, \dots, \mathbf{maxit}$ $\mathbf{q}_i = \mathbf{A}\mathbf{p}_i$ $\alpha_i = \gamma_i / \ \mathbf{q}_i\ ^2$ $\mathbf{x}_{i+1} = \mathbf{x}_i + \alpha_i \mathbf{p}_i$ $\mathbf{r}_{i+1} = \mathbf{r}_i - \alpha_i \mathbf{q}_i$ If converged within \mathbf{tol} , then stop. $\mathbf{s}_{i+1} = \mathbf{A}^H \mathbf{r}_{i+1}$ $\gamma_{i+1} = \ \mathbf{s}_{i+1}\ ^2$ $\beta_i = \gamma_{i+1} / \gamma_i$ $\mathbf{p}_{i+1} = \mathbf{s}_{i+1} + \beta_i \mathbf{p}_i$ end $\mathbf{x}_{sol} = \mathbf{x}_{i+1}$	

The linear system belonging to the imaging problem is solved by conjugate gradient least squares algorithm (CGLS) whose steps are given in Table 4.1. The FMM is applied in the 1st, 2nd, 4th, and 8th steps, where forward operator and its adjoint are multiplied by a vector. The truncation number is determined by (4.16) to be 9. Translation, aggregation and disaggregation functions are separately calculated beforehand and stored in memory. Then, they are recalled into the main code, thus, it is aimed to further reduce the time consumption of the solver. Absolute values of the reconstructed reflectivity values obtained with the application of FMM are given for two different truncation orders in Table 4.2. As a result of the truncation order,

FMM approach yields an error and it can be mathematically measured by the mean absolute percentage error (MAPE), which is given as

$$\text{MAPE} = \frac{100\%}{n} \sum_{t=1}^n \left| \frac{a_t - f_t}{a_t} \right|$$

where a_t is the t^{th} component of the exact solution, f_t is the t^{th} component obtained with FMM, and n is the dimension of the solution vectors. The MAPE of this imaging scenario when $N = 9$ is calculated as 2.35%. This error can be decreased to 1.27% with $N = 19$. However, increasing truncation order will remove the efficiency that FMM formulation provides in terms of CPU time.

Table 4.2 Reflectivity values obtained using FMM and direct matrix multiplication.

		Reflectivity								
		f_1	f_2	f_3	f_4	f_5	f_6	f_7	f_8	f_9
Exact Solution		1.0000	1.0000	1.0000	1.0000	1.0000	1.0000	1.0000	1.0000	1.0000
FMM Solution	$N = 9$	1.0200	1.0508	1.0199	1.0041	1.0203	1.0047	1.0199	1.0519	1.0196
	$N = 19$	1.0110	1.0415	1.0097	1.0013	1.0098	1.0019	1.0101	1.0228	1.0065

An inverse scattering problem is the problem of determining characteristics of an object based on information of how it scatters the incoming radiation. It means that exact location of the target is unknown and one must scan the volume of interest in three dimensions with spatial steps that is smaller than cross range resolution. This, in result, leads to a highly ill-conditioned observation matrix that must be treated with some regularization techniques. Since any regularization method is not applied in this stage, the spatial steps are kept equal to the Rayleigh criterion (2.4 cm), hence, the observation matrix is well-conditioned.

Finally, the improvement that the FMM provides is demonstrated by repeating the same target scenario for different number of antenna elements. Fig. 4.3 depicts CPU time (in seconds) and memory requirement (in Mbytes) per matrix-vector product as a function of number of antenna elements (i.e., $N_T = N_R$). As expected, complexities of both CPU time and memory requirement are proportional to $O(N_T + N_R)$, when

the FMM is applied in the solution of the imaging problem. The FMM outperforms the direct matrix-vector product above a crossover point, which depends on truncation order, imaging geometry, etc. Note that Fig. 4.3(b) plots the average memory usage that is monitored on the task manager during runtime.

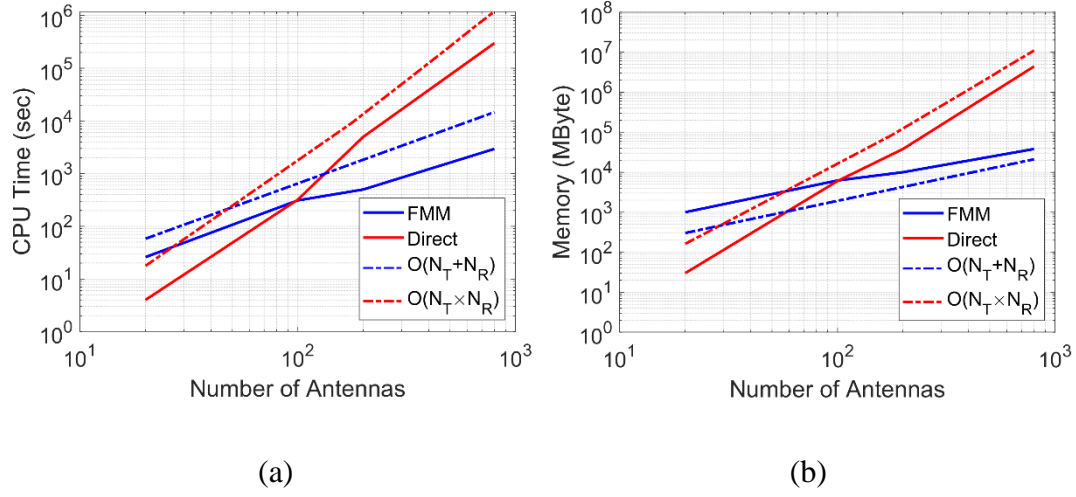


Figure 4.3. (a) CPU time, (b) memory requirement per matrix-vector product with respect to the number of the antennas for the FMM and the direct method.

CHAPTER 5

SPARSE SOLUTION TO IMAGING PROBLEMS

Sparsity-based algorithms have been widely applied to imaging problems lately [89-92]. In all these problems, it is aimed to represent the measurement data sparsely by using minimum number of vectors from a set of vectors, namely dictionary¹. The search for identifying the most useful vectors to establish the sparsest solution is computationally very intensive (NP-hard). In the literature, therefore, much effort has been made to find low complexity algorithms, which give close solutions to those that can be achieved by exhaustive search.

For the solution of near-field MIMO imaging problems, two major categories of sparsity-based algorithms will be addressed in the scope of this chapter: Greedy pursuit methods and convex optimization techniques. The algorithms falling into these two categories are very practical in terms of implementation and computation. They not only have the ability of sparsifying the solution, but also regularize it. While greedy methods are based on ℓ_0 “norm”, convex optimization methods are constructed using ℓ_1 -norm.

This chapter will first introduce some of the now-standard sparsity-based algorithms. Then, it will show how FMM formulation will be applied into these algorithms and demonstrate its performance through several near-field imaging scenarios.

¹ Assume that $\mathbf{A} \in \mathbb{C}^{M \times N}$ is a complex matrix whose columns have unit ℓ_2 -norm, i.e., $\|\mathbf{A}_i\|_2 = 1$ for $i = 1, \dots, N$. This matrix is called *dictionary*.

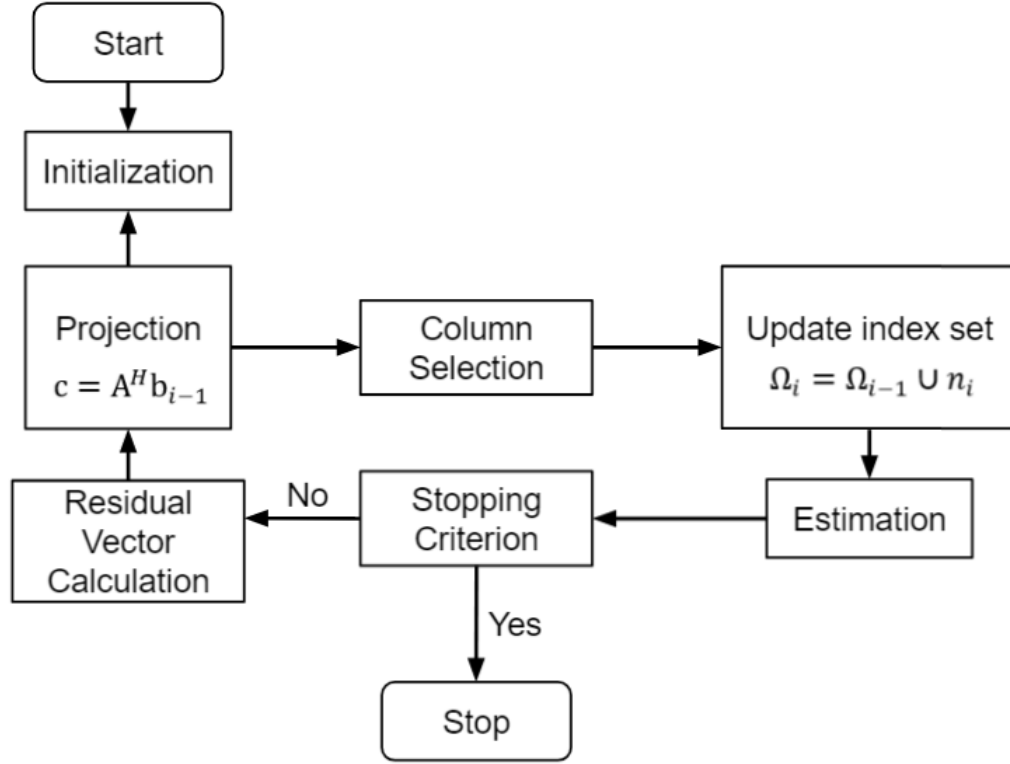


Figure 5.1. Block diagram for greedy pursuit algorithms [93].

5.1 Greedy Pursuit Methods

A pursuit method basically abandons the exhaustive search and attempts to estimate a solution vector by modifying (or eliminating) one or multiple of its components at each iteration, hence, the solution is improved in terms of sparsity and regularization. Matching pursuit (MP), orthogonal matching pursuit (OMP), stagewise orthogonal matching pursuit (StOMP), regularized orthogonal matching pursuit (ROMP), and compressive sampling matching pursuit (CoSaMP) can be listed among such methods in the literature. The main difference between these methods is the approach that is used in each of them for determining the number of useful columns in the dictionary. For example, MP and OMP select only one column at each iteration, whereas StOMP, ROMP, and CoSaMP select multiple columns. In addition, they differ in calculating the residual vector and estimating non-zero components of the

solution vector [93]. Fig. 5.1 illustrates a block diagram for a generic greedy pursuit method.

5.1.1 Matching Pursuit

If the matrix of the linear system is composed of large number of columns, it is an NP-hard problem to search for columns that gives the sparsest representation of the solution. In 1993, Mallat and Zhang proposed a greedy solution for such a problem, namely matching pursuit. This solution successively stores the indices of the columns, whose projections on the solution are the strongest, into an index set [94].

In order to find sparse \mathbf{x} solution for $\mathbf{Ax} = \mathbf{b}$ problem, matching pursuit algorithm starts with a zero solution vector $\mathbf{x}_0 = \emptyset$, and at i^{th} iteration, it finds the column $\mathbf{a}_{n_i} \in \mathbf{A}$ that has the strongest projection on the residual vector \mathbf{r}_{i-1} by

$$n_i = \underset{l}{\operatorname{argmax}} |\mathbf{a}_l^H \mathbf{r}_{i-1}|, \quad l = 1, 2, \dots, N. \quad (5.1)$$

Let \mathbf{D}_i be a dictionary matrix, which is updated by \mathbf{a}_{n_i} at each iteration, and Ω_i be the index set, where the indices of the selected columns are stored. After i^{th} iteration, \mathbf{D}_i and Ω_i can be defined by

$$[\mathbf{D}_{i-1}, \mathbf{a}_{n_i}],$$

$$\text{and } \Omega_i = \Omega_{i-1} \cup n_i,$$

respectively. Then, residual vector is calculated by

$$\mathbf{r}_i = \mathbf{r}_{i-1} - \frac{(\mathbf{a}_{n_i}^H \mathbf{r}_{i-1}) \mathbf{a}_{n_i}}{\|\mathbf{a}_{n_i}\|_2^2} \quad (5.2)$$

and the corresponding component of the solution vector is estimated by

$$\mathbf{x}_i(n_i) = \mathbf{x}_{i-1}(n_i) \frac{(\mathbf{a}_{n_i}^H \mathbf{r}_{i-1})}{\|\mathbf{a}_{n_i}\|_2^2}. \quad (5.3)$$

One stopping criterion that can be used for the matching pursuit algorithm is $\|\mathbf{r}_i\|_2 \leq \epsilon$ [93].

5.1.2 Orthogonal Matching Pursuit (OMP)

Orthogonal matching pursuit shares the same principle as MP method. It picks one column of \mathbf{A} at each iteration, which best approximates the residual. However, it does not simply update the residual by solving (5.2), instead it projects the estimate orthogonally onto the updated dictionary, which accounts for the term “orthogonal” [95-97].

Table 5.1 Algorithmic steps of orthogonal matching pursuit (OMP)

Orthogonal Matching Pursuit (OMP) [34]	
Task: Approximate the solution of	$\min_{\mathbf{x}} \ \mathbf{x}\ _0$ subject to $\mathbf{Ax} = \mathbf{b}$
Input: A matrix $\mathbf{A} \in \mathbb{R}^{M \times N}$ and a vector $\mathbf{b} \in \mathbb{R}^M$	
Output: A sparse solution $\mathbf{x} \in \mathbb{R}^N$.	
1) Initialize: Set counter $i = 0$. Set the index set $\Omega_0 = \emptyset$. Set the residual vector $\mathbf{r}_0 = \mathbf{b} - \mathbf{Ax}_0$.	
2) Identify: Find a column \mathbf{n}_i of \mathbf{A} that is most strongly correlated with the residual vector: $\mathbf{n}_i = \underset{l}{\operatorname{argmax}} \langle \mathbf{r}_{i-1}, \mathbf{a}_{n_l} \rangle , \quad l = 1, 2, \dots, N \text{ and}$ $\Omega_i = \Omega_{i-1} \cup \mathbf{n}_i.$	
3) Estimate: Find the best coefficients for approximating the signal with the columns chosen so far. $\mathbf{x}_i = \underset{\mathbf{y}}{\operatorname{argmin}} \ \mathbf{b} - \mathbf{A}_{\Omega_i} \mathbf{y}\ _2.$	
4) Iterate: Update the residual: $\mathbf{r}_i = \mathbf{b} - \mathbf{A}_{\Omega_i} \mathbf{x}_i.$ Increment i . Repeat (2) - (4) until stopping criterion is reached.	
5) Output: $\mathbf{x}(n) = \mathbf{x}_i(n)$ for $n \in \Omega_i$ and $\mathbf{x}(n) = \mathbf{0}$ otherwise.	

The steps of the OMP algorithm are given in Table 5.1. Identification step is computationally the most expensive part of the algorithm with the complexity of $O(sMN)$, where s is the desired number of nonzeros in the approximated solution. For an exhasutive search, this step would take $O(MN^s s^2)$. The most basic approach for identifying the columns that are strongly correlated to the residual vector is calculating maximum inner product by matrix-vector product $\mathbf{A}^H \mathbf{r}_{i-1}$, which costs $O(MN)$.

The estimation step consists in solving a minimization problem. This step costs $O(IM)$, where I is the number of iterations that takes till the algorithm is stopped. The updated residual is also obtained as a result of this step, therefore, it does not require an extra calculation and does not increase the complexity of the algorithm.

There are several stopping criteria that might be used for the OMP algorithm, which are given below:

- Iterate till desired number of non-zero components in the solution vector is reached. If the solution vector is desired to be s -sparse, then the iterations are stopped when iteration number reaches the desired sparsity level.
- Stop when $\|\mathbf{r}_i\| \leq \epsilon$ is reached.
- Stop when $\|\mathbf{A}^H \mathbf{r}_{i-1}\|_\infty \leq \epsilon$ is reached [34].

Provided that the dictionary represents the measurement data exactly, OMP is capable of solving the problem with $\mathbf{r}_I = \emptyset$ after I iterations. However, this solution is not sparse. In general, greedy pursuit methods prioritize rate of convergence and regularization of the solution, instead of sparsity.

5.1.3 Stagewise Orthogonal Matching Pursuit (StOMP)

Stagewise orthogonal pursuit method, introduced by Donoho et al. in 2012 [98], is an improved form of OMP. Contrary to OMP, this method selects multiple column indices at each iteration that the authors called stage. As in OMP, StOMP implements

the algorithm upon the observation vector $\mathbf{y} = \mathbf{A}^H \mathbf{b}$, where \mathbf{b} is the measurement vector, i.e., $\mathbf{b} = \mathbf{A}\mathbf{x}$. But, instead of selecting the largest component of \mathbf{y} at each iteration, it follows a threshold strategy, selecting all components above a threshold value $t_s \sigma_s$ where σ_s is noise level that can be defined by

$$\sigma_s = \|r_i\|_2 / \sqrt{M}$$

and t_s takes values in the range $2 \leq t_s \leq 3$. Then, a minimization problem is solved in order to update the residual vector. StOMP algorithm continues to run till a fixed number of stages reached, whereas OMP requires to iterate by the number of desired

Table 5.2 Algorithmic steps for stagewise orthogonal matching pursuit

Stagewise Orthogonal Matching Pursuit (StOMP) [99]

Task: Approximate the solution of $\min_{\mathbf{x}} \|\mathbf{x}\|_0$ **subject to** $\mathbf{A}\mathbf{x} = \mathbf{b}$

Input: A matrix $\mathbf{A} \in \mathbb{C}^{M \times N}$ and a vector $\mathbf{b} \in \mathbb{C}^M$

Output: A sparse solution $\mathbf{x} \in \mathbb{C}^N$.

- 1) **Initialize:** Set counter $i = 0$.
 Set the index set $\Omega_0 = \emptyset$.
 Set the residual vector $\mathbf{r}_0 = \mathbf{b} - \mathbf{A}\mathbf{x}_0$.
- 2) **Identify:** Using the observation vector $\mathbf{y} = \mathbf{A}^H \mathbf{r}$, set

$$J = \{j: |y_j| > t_i \sigma_i\}$$
- 3) **Update:** Add the set J to index set Ω : $\Omega \leftarrow \Omega \cup J$ and update the estimate and residual by

$$\mathbf{x} = (\mathbf{A}_\Omega^H \mathbf{A}_\Omega)^{-1} \mathbf{A}_\Omega^H \mathbf{b}$$
 and $\mathbf{r} = \mathbf{b} - \mathbf{A}\mathbf{x}$,
 respectively.

sparsity level [99]. The algorithmic steps for StOMP are given in Table 5.2.

Despite the fact that it shares a similar structure to OMP, StOMP outperforms OMP in terms of runtime, since it selects multiple components at each iteration. However, in practical applications, selecting the threshold value and its implementation into

the algorithm might be difficult. Besides, different threshold values may lead to different solutions [98-101].

5.1.4 Other Matching Pursuit Methods

Literature has modern MP-based methods, which have been suggested recently for the improvement of standard greedy pursuit methods. They are developed to work better in specific situations and focus on some of the following features:

- Selecting multiple useful columns at each iteration,
- eliminating the columns that do not improve the solutions,
- solving the minimization problem at the estimation step in a computationally efficient way.

Regularized orthogonal matching pursuit (ROMP) [101], and compressive sampling matching pursuit (CoSaMP) [102,103] are the most popular modern pursuit methods. They are modifications of OMP that investigate various approaches for the

Table 5.3 Algorithmic steps of regularized orthogonal matching pursuit.

Regularized Orthogonal Matching Pursuit (ROMP) [93]	
Task: Approximate the solution of $\min_x \ x\ _0$	subject to $Ax = b$
Input: A matrix $A \in \mathbb{C}^{M \times N}$ and a vector $b \in \mathbb{C}^M$	
Output: A sparse solution $x \in \mathbb{C}^N$.	
<p>6) Initialize: Set counter $i = 0$. Set the index set $\Omega_0 = \emptyset$. Set the residual vector $r_0 = b - Ax_0$.</p> <p>7) Identify: $\Omega_i = \{s\text{-biggest indices in } c_i = A^H r_{i-1}\}$</p> <p>8) Regularize: Among all subsets $J_i \subset \Omega_i$, choose J_i with the maximal energy $\ c(J_i)\ _2$.</p> <p>9) Update: Add the set J_i to the index set: $\Omega_i = \Omega_i \cup J_i$. Calculate</p> $x_i = A(\Omega_i)^H b$ <p>and update the residual vector</p> $r_i = b - A(\Omega_i)x_i.$	

improvement of column selection. Full form of their algorithms are given in Table 5.3 and Table 5.4, respectively.

ROMP was first suggested in [101]. In its identification step, it first calculates projection vector $\mathbf{c}_i = \mathbf{A}^H \mathbf{r}_{i-1}$ ($\mathbf{r}_0 = \mathbf{b}$) to find coordinates of s biggest coefficients in \mathbf{c}_i and stack them into a set J . Then in regularization step, it searches in J for coordinates that corresponding coefficient's magnitude is greater than half the largest coefficient's magnitude. These coordinates correspond to indices of the selected columns in each iteration. This is where ROMP differs from StOMP, which uses a predetermined threshold value, in selecting columns. Also, in theory, runtime of ROMP is comparable to OMP, but it converges faster in practical cases [93].

Table 5.4 Algorithmic steps of compressive sampling matching pursuit

Compressive Sampling Matching Pursuit (CoSaMP) [93]	
Task: Approximate the solution of $\min_{\mathbf{x}} \ \mathbf{x}\ _0$	subject to $\mathbf{A}\mathbf{x} = \mathbf{b}$
Input: A matrix $\mathbf{A} \in \mathbb{C}^{M \times N}$ and a vector $\mathbf{b} \in \mathbb{C}^M$	
Output: A sparse solution $\mathbf{x} \in \mathbb{C}^N$.	
<p>10) Initialize: Set counter $i = 0$. Set the index set $\Omega_0 = \emptyset$. Set the residual vector $\mathbf{r}_0 = \mathbf{b} - \mathbf{A}\mathbf{x}_0$.</p>	
<p>11) Identify: A proxy of the residual vector from the current samples is formed and the largest components of the proxy $\mathbf{c}_i = \mathbf{A}^H \mathbf{r}_{i-1}$ are located. The first $2s$ entries of \mathbf{c}_i with the largest absolute values are selected, and the selected indices compose J_i.</p>	
<p>12) Support Merge: The set of newly identified components is united with the set of components that appears in the current approximation. $\Omega_i = J_i \cup \text{supp}(\mathbf{x}_{i-1})$ is identified as the augmentation of the support of the previous estimate \mathbf{x}_{i-1} with the $2s$ indices corresponding to the entries \mathbf{c}_i with the largest absolute values.</p>	
<p>13) Estimate: A least squares problem is solved to approximate the signal</p> $\mathbf{y}_i = \mathbf{A}(\Omega_i)^H \mathbf{b}.$	
<p>14) Prune: Keep the largest s components of \mathbf{y}_i, which is assigned as \mathbf{x}_i.</p>	
<p>15) Update: Update the residual vector</p> $\mathbf{r}_i = \mathbf{b} - \mathbf{A}(\Omega_i) \mathbf{x}_i.$	

CoSaMP was first introduced in [102], which incorporates all three items given above. As in StOMP and ROMP, it selects multiple columns at each iteration, which have the largest correlation with the measurement vector \mathbf{b} . To do this, coordinates of the first $2s$ coefficients of the projection with the biggest magnitude are sought to compose the set of indices belonging to the useful columns of the dictionary. In [103], Dai and Milenkovic proposed an algorithm that they called sub-space pursuit and it offers similar theoretical guarantees with CoSaMP. The other variants of CoSaMP are studied in [104]. In [135], perturbed OMP is proposed, where controlled perturbations are performed on the selected columns so that orthogonal residual can be decreased at each iteration.

5.1.5 Numerical Examples

Due to its compact structure and ease of implementation, we choose OMP algorithm for the demonstration of two near-field imaging scenarios with point scatterers. Fig. 5.2(a) shows the first imaging scenario, where PSF of the plus-shaped MIMO array is obtained in a similar way to that shown in Chapter 3, but this time it is reconstructed by OMP algorithm. The point scatterer is placed 55 cm away from the center of the array. The imaging setup scans a linear path at $y = 55$ cm, extending from $x = -20$ cm to $x = +20$ cm, with 101 spatial steps. Fig 5.3(a) plots normalized PSF with the sparsity level of 101, implying that approximated solution is not sparse.

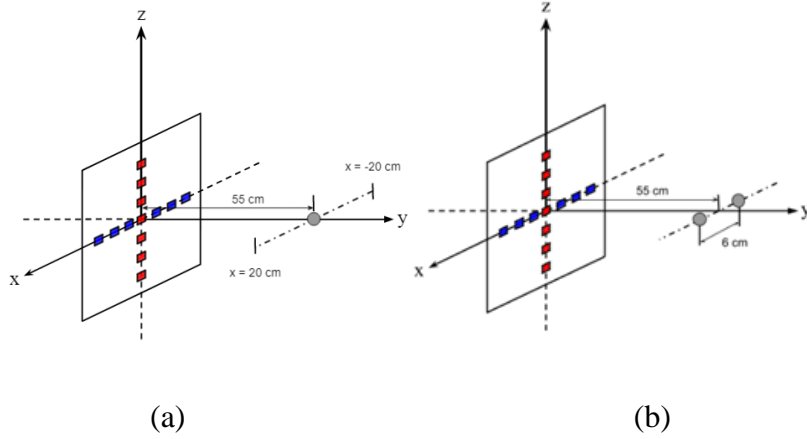


Figure 5.2. Imaging geometry (a) for one point scatterer and (b) for two point scatterers.

As discussed earlier, the sparsity level of the solution can be determined with the number of iterations that OMP algorithm takes. For different sparsity levels, the approximate solutions are plotted in Fig. 5.3(b) and Fig. 5.3(c). It can be seen that the algorithm keeps the largest s components and forces the rest to be zero. As the sparsity level is reduced to 1, the solution contains only the largest value, whose index corresponds to exact location of the point scatterer.

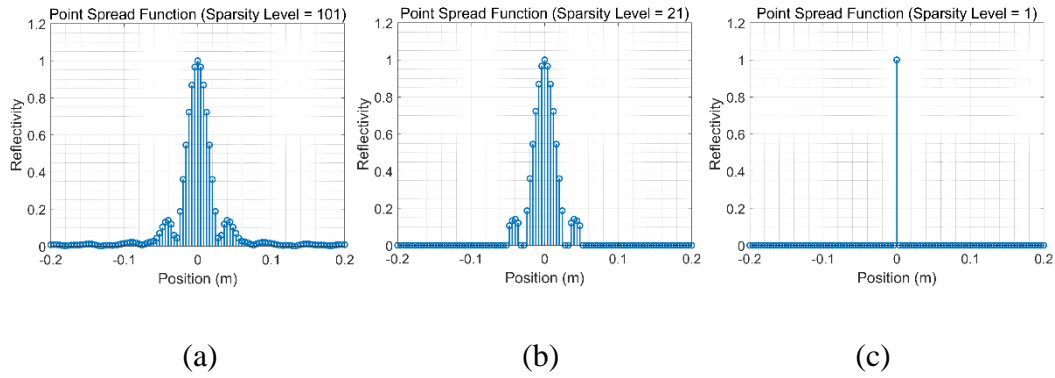


Figure 5.3. Reconstructed point spread functions for different sparsity levels: (a) 101-sparse, (b) 21-sparse, (c) 1-sparse.

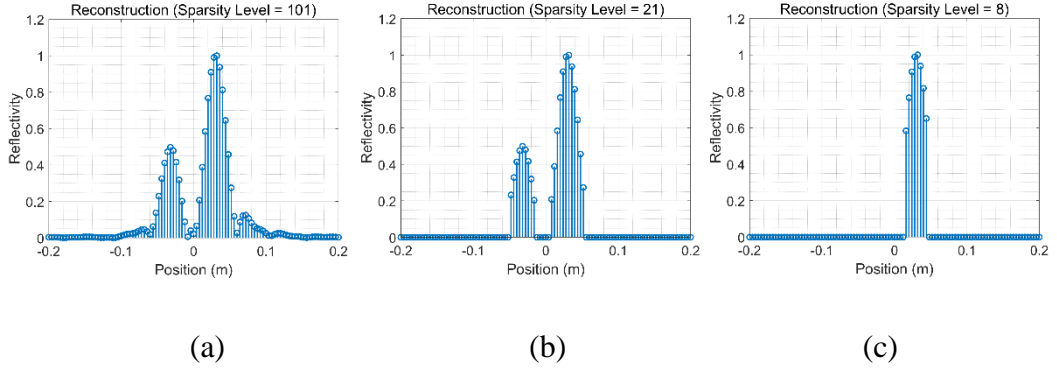


Figure 5.4. Reconstructed solutions for different sparsity levels: (a) 101-sparse, (b) 21-sparse, (c) 8-sparse.

However, the same result as obtained in Fig. 5.3(c) may not be achieved for an imaging scene containing multiple point scatterers with different reflectivity levels. To demonstrate such an imaging scenario, two point scatterers that are 6 cm apart from each other are considered, as shown in Fig. 5.2(b). The point scatterer located at $x = -3$ cm (scatterer #1) has reflectivity level of 0.5, while the other is located at $x = +3$ cm (scatterer #2) and its reflectivity is 1.0. Fig. 5.4(a) shows the reconstructed non-sparse solution. As the sparsity level is reduced to 21, two point scatterers can still be solved. But, only scatterer #2 can be obtained when the sparsity level is below 9. Scatterer #1 disappears in the reconstruction since its highest reflectivity level is lower than 8 largest component of the scatterer #2's response. Therefore, for such a scenario, it is not possible to extract the sparsest solution that yields the reflectivity levels at the exact locations of the scatterers, as obtained in the first scenario.

5.1.6 Application of FMM in OMP Algorithm

- Identification step:

In the identification step, OMP includes adjoint operator, where maximum inner product is calculated by $\mathbf{A}^H \mathbf{r}_{i-1}$. For a large scale imaging problem, this step will be computationally very demanding, therefore, we use FMM to calculate the matrix-vector product.

- Estimation step:

Estimation step solves $\mathbf{x}_i = \underset{\mathbf{y}}{\operatorname{argmin}} \|\mathbf{b} - \mathbf{A}_{\Omega_i} \mathbf{y}\|_2$ at each iteration, where \mathbf{A}_{Ω_i} involves columns that has the largest projection on the residual vector at i^{th} iteration. As the algorithm iterates, identified columns are stacked in Ω . So, number of columns in \mathbf{A}_{Ω_i} increases at each iteration. Provided that desired solution is non-sparse, this step will solve the minimization problem $\mathbf{x}_i = \underset{\mathbf{y}}{\operatorname{argmin}} \|\mathbf{b} - \mathbf{A} \mathbf{y}\|_2$ in the last iteration, since $\mathbf{A}_{\Omega_i} = \mathbf{A}$ at that step. Here, we solve this minimization problem with an inner iteration by CGLS, where forward operator and its adjoint is calculated by using FMM formulation.

The second imaging scenario is simulated again for demonstrating FMM. While FMM is applied in both identification and estimation steps in non-sparse (101-sparse) case, it is applied to only identification step in 21-sparse and 8-sparse cases. Fig. 5.5 shows the normalized reconstructions when FMM is applied. As can be seen, the solutions are in good agreement with those obtained without FMM, except for the truncation error, which is measured here by MAPE. When non-sparse solutions are compared, MAPE is calculated as $\sim 0.9\%$.

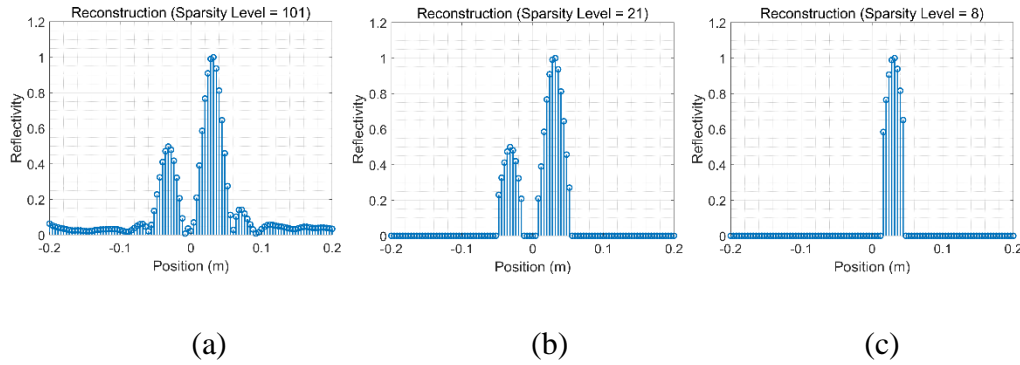


Figure 5.5. Reconstructed solutions with FMM for different sparsity levels: (a) 101-sparse, (b) 21-sparse, (c) 8-sparse.

5.2 Convex Optimization Techniques

Another approach to find a sparse solution to an inverse problem is replacing ℓ_0 “norm” in (2.24) with l_1 -norm, yielding a convex optimization problem in unconstrained form

$$\min_{\mathbf{x}} \|\mathbf{Ax} - \mathbf{b}\|_2^2 + \lambda \|\mathbf{x}\|_1. \quad (5.4)$$

(5.4) is referred to as “least absolute shrinkage and selection operator (LASSO)” and it can be redefined in a constrained form [105]

$$\min_{\mathbf{x}} \|\mathbf{x}\|_1 \quad \text{subject to} \quad \|\mathbf{Ax} - \mathbf{b}\|_2 \leq \varepsilon. \quad (5.5)$$

where, ε is the error tolerance due to noisy measurement data and it is estimated by signal-to-noise ratio (SNR) of the received signal. Both (5.4) and (5.5) do not have an analytical solution, therefore, wide variety of research contributions have been added into the literature to develop new algorithms, which can give optimally sparse solutions for them. Lately, “alternating direction method of multipliers” (ADMM) and “constrained split augmented Lagrangian shrinkage algorithm (C-SALSA-1 and C-SALSA-2) have been the most studied algorithms, especially in imaging application.

5.2.1 Alternate Direction Method of Multipliers (ADMM)

5.2.1.1 Background

Before investigating ADMM, four concepts must be studied in order to gain insight about its background: (i) Dual ascent, (ii) dual decomposition, (iii) method of multipliers, and (iv) variable splitting.

(i) Dual Ascent

General form of an equality-constrained convex optimization problem is given by

$$\begin{aligned} & \text{minimize } f(\mathbf{x}) \\ & \text{subject to } \mathbf{Ax} = \mathbf{b} \end{aligned} \quad (5.6)$$

where $f: \mathbb{C}^N \rightarrow \mathbb{C}$ is a convex (objective) function. The Lagrangian form of (5.6) is

$$L(\mathbf{x}, \mathbf{y}) = f(\mathbf{x}) + \mathbf{y}^T (\mathbf{Ax} - \mathbf{b}) \quad (5.7)$$

and its dual function is

$$g(\mathbf{y}) = \inf_{\mathbf{x}} L(\mathbf{x}, \mathbf{y}) = -f^*(-\mathbf{A}^T \mathbf{y}) - \mathbf{b}^T \mathbf{y} \quad (5.8)$$

where \mathbf{y} is dual variable (or Lagrangian multiplier) and f^* is convex conjugate of f [107,108]. The dual problem has the form of

$$\text{maximize } g(\mathbf{y}). \quad (5.9)$$

Dual ascent method solves (5.9) by gradient ascent. Presumed to be differentiable, gradient of the dual function $\nabla g(\mathbf{y})$ can be calculated by first solving $\mathbf{x}^+ = \underset{\mathbf{x}}{\text{argmin}} L(\mathbf{x}, \mathbf{y})$, then substituting \mathbf{x}^+ into $\nabla g(\mathbf{y}) = \mathbf{Ax}^+ - \mathbf{b}$. The dual ascent consists of iterating the following updates till convergence is achieved:

$$\mathbf{x}^{k+1} := \underset{\mathbf{x}}{\text{argmin}} L(\mathbf{x}, \mathbf{y}) \quad (5.10)$$

$$\mathbf{y}^{k+1} := \mathbf{y}^k + \alpha^k (\mathbf{Ax}^{k+1} - \mathbf{b}) \quad (5.11)$$

where α^k is step size and k is iteration count. (5.10) is referred to as \mathbf{x} -minimization step, whereas (5.11) is dual variable update step. If α^k is chosen appropriately, dual function $g(\mathbf{y})$ increases gradually at each iteration, i.e., $g(\mathbf{y}^{k+1}) > g(\mathbf{y}^k)$, therefore, this method is called “dual ascent” [107].

(ii) Dual Decomposition

Assume that function f is separable such that

$$f(\mathbf{x}) = \sum_{i=1}^N f_i(\mathbf{x}_i) \quad (5.12)$$

where $\mathbf{x}_i \in \mathbb{C}^{n_i}$ are subvectors of \mathbf{x} . Splitting \mathbf{A} into submatrices as $\mathbf{A} = [\mathbf{A}_1 \dots \mathbf{A}_N]$, equality constraint can be rewritten as

$$\mathbf{Ax} = \sum_{i=1}^N \mathbf{A}_i \mathbf{x}_i. \quad (5.13)$$

Lagrangian form of (5.13), which is also separable in \mathbf{x} , can be given as

$$L(\mathbf{x}, \mathbf{y}) = \sum_{i=1}^N L_i(\mathbf{x}_i, \mathbf{y}) = \sum_{i=1}^N (f_i(\mathbf{x}) + \mathbf{y}^T \mathbf{A}_i \mathbf{x}_i - (1/N) \mathbf{y}^T \mathbf{b}). \quad (5.14)$$

(5.10) can be decomposed into N separate parts that can be computed in parallel, leading to following updates to be iterated:

$$\mathbf{x}_i^{k+1} := \underset{\mathbf{x}}{\operatorname{argmin}} L_i(\mathbf{x}_i, \mathbf{y}^k) \quad (5.15)$$

$$\mathbf{y}^{k+1} := \mathbf{y}^k + \alpha^k (\mathbf{Ax}^{k+1} - \mathbf{b}). \quad (5.16)$$

The \mathbf{x} -minimization step given in (5.15) is solved separately, but in parallel, for each part ($i = 1, \dots, N$). So, this procedure is called “dual decomposition”.

(iii) Method of Multipliers

In order to make the dual ascent method robust, Lagrangian form given in (5.7) can be augmented by

$$L_\rho(\mathbf{x}, \mathbf{y}) = f(\mathbf{x}) + \mathbf{y}^T (\mathbf{Ax} - \mathbf{b}) + (\rho/2) \|\mathbf{Ax} - \mathbf{b}\|_2^2 \quad (5.17)$$

where $\rho > 0$ is denoted as penalty parameter. When $\rho = 0$ or a feasible solution \mathbf{x} is introduced into the problem, (5.17) corresponds to the standard Lagrangian expression. The augmented Lagrangian can be associated with the following problem:

$$\begin{aligned} & \text{minimize } f(\mathbf{x}) + (\rho/2) \|\mathbf{Ax} - \mathbf{b}\|_2^2 \\ & \text{subject to } \mathbf{Ax} = \mathbf{b}. \end{aligned} \quad (5.18)$$

The modified problem can be solved by applying dual ascent, which yields the following update equations:

$$\mathbf{x}^{k+1} := \underset{\mathbf{x}}{\operatorname{argmin}} L_\rho(\mathbf{x}, \mathbf{y}^k) \quad (5.19)$$

$$\mathbf{y}^{k+1} := \mathbf{y}^k + \rho(\mathbf{A}\mathbf{x}^{k+1} - \mathbf{b}). \quad (5.20)$$

This algorithm is named the “method of multipliers” and it differs from the standard dual ascent by carrying out \mathbf{x} -minimization step with augmented Lagrangian and using penalty parameter ρ instead of α^k . Unlike standard dual ascent, method of multipliers has the advantage of converging under milder conditions, i.e., it converges even when f is not strictly convex. Therefore, its convergence rate is comparably higher than standard dual ascent [106].

(iv) Variable Splitting

Consider following unconstrained problem

$$\min_{\mathbf{x}} f_1(\mathbf{x}) + f_2(\mathbf{G}\mathbf{x}) \quad (5.21)$$

where $\mathbf{G} \in \mathbb{C}^{M \times N}$, $f_1: \mathbb{C}^N \rightarrow \mathbb{C}$, and $f_2: \mathbb{C}^N \rightarrow \mathbb{C}$. In variable splitting, a new variable $\mathbf{z} = \mathbf{G}\mathbf{x}$ is defined as the argument of f_2 and the unconstrained problem becomes

$$\min_{\mathbf{x}, \mathbf{z}} f_1(\mathbf{x}) + f_2(\mathbf{z}) \quad \text{subject to} \quad \mathbf{z} = \mathbf{G}\mathbf{x}. \quad (5.22)$$

Purpose of variable splitting is that it may be easier to solve (5.22) than the unconstrained problem of (5.21) in some cases [41].

5.2.1.2 ADMM Algorithm

ADMM is developed to bring decomposability of the dual ascent method and high convergence rate of the method of multipliers together. It solves a problem in the following form:

$$\begin{aligned} & \text{minimize } f(\mathbf{x}) + g(\mathbf{z}) \\ & \text{subject to } \mathbf{A}\mathbf{x} + \mathbf{B}\mathbf{z} = \mathbf{c} \end{aligned} \quad (5.23)$$

where $\mathbf{x} \in \mathbb{C}^N$, $\mathbf{z} \in \mathbb{C}^M$, $\mathbf{A} \in \mathbb{C}^{p \times N}$, $\mathbf{B} \in \mathbb{C}^{p \times M}$, and $\mathbf{c} \in \mathbb{C}^p$. In ADMM, \mathbf{x} is split into \mathbf{x} and \mathbf{z} , and the objective function is distributed over them. Augmented Lagrangian form of (5.23) is given as

$$L_\rho(\mathbf{x}, \mathbf{y}, \mathbf{z}) = f(\mathbf{x}) + g(\mathbf{z}) + \mathbf{y}^T (\mathbf{Ax} + \mathbf{Bz} - \mathbf{c}) + (\rho/2) \|\mathbf{Ax} + \mathbf{Bz} - \mathbf{c}\|_2^2. \quad (5.24)$$

ADMM involves the following updates in its iterations:

$$\mathbf{x}^{k+1} := \underset{\mathbf{x}}{\operatorname{argmin}} L_\rho(\mathbf{x}, \mathbf{z}^k, \mathbf{y}^k) \quad (5.25)$$

$$\mathbf{z}^{k+1} := \underset{\mathbf{z}}{\operatorname{argmin}} L_\rho(\mathbf{x}^{k+1}, \mathbf{z}, \mathbf{y}^k) \quad (5.26)$$

$$\mathbf{y}^{k+1} := \mathbf{y}^k + \rho(\mathbf{Ax}^{k+1} + \mathbf{Bz}^{k+1} - \mathbf{c}) \quad (5.27)$$

where $\rho > 0$. Method of multipliers for (5.23) is written as

$$(\mathbf{x}^{k+1}, \mathbf{z}^{k+1}) := \underset{\mathbf{x}, \mathbf{z}}{\operatorname{argmin}} L_\rho(\mathbf{x}, \mathbf{z}, \mathbf{y}^k)$$

$$\mathbf{y}^{k+1} := \mathbf{y}^k + \rho(\mathbf{Ax}^{k+1} + \mathbf{Bz}^{k+1} - \mathbf{c})$$

where augmented Lagrangian is minimized with respect to the variables in the same update. On the other hand, ADMM updates the variables sequentially (or in an alternating fashion), and the method takes its name from this “alternating direction” [106].

The LASSO problem given in (5.4) can be rewritten in ADMM form as

$$\text{minimize } f(\mathbf{x}) + g(\mathbf{z})$$

$$\text{subject to } \mathbf{x} - \mathbf{z} = \mathbf{0},$$

where $f(\mathbf{x}) = \|\mathbf{Ax} - \mathbf{b}\|_2^2$ and $g(\mathbf{z}) = \lambda \|\mathbf{z}\|_1$. Finally, the update equations for LASSO problem are obtained as [106]

$$\mathbf{x}^{k+1} := (\mathbf{A}^T \mathbf{A} + \rho \mathbf{I})^{-1} (\mathbf{A}^T \mathbf{b} + \rho(\mathbf{z}^k - \mathbf{u}^k)), \quad (5.28)$$

$$\mathbf{z}^{k+1} := S_{\lambda/\rho}(\mathbf{x}^{k+1} + \mathbf{u}^k), \quad (5.29)$$

$$\mathbf{u}^{k+1} := \mathbf{u}^k + \mathbf{x}^{k+1} - \mathbf{z}^{k+1}. \quad (5.30)$$

The z-update in (5.29) is carried out by soft-thresholding operator $S_{\lambda/\rho}$, which is mathematically defined as

$$S_{\lambda/\rho}(\mathbf{x}^{k+1} + \mathbf{u}^k) := \begin{cases} \mathbf{x}_i + \mathbf{u}_i - \lambda/\rho, & |\mathbf{x}_i + \mathbf{u}_i| \geq \lambda/\rho \\ \mathbf{x}_i + \mathbf{u}_i + \lambda/\rho, & |\mathbf{x}_i + \mathbf{u}_i| \leq -\lambda/\rho \\ 0 & \text{else} \end{cases} \quad (5.31)$$

Table 5.5 Algorithmic steps of ADMM

ADMM [40,44]
1. Set $\mathbf{k} = \mathbf{0}$, choose $\rho > \mathbf{0}$, \mathbf{z}_0 , \mathbf{u}_0
2. repeat
3. $\mathbf{x}_{k+1} = \underset{\mathbf{x}}{\text{argmin}} \ \mathbf{A}\mathbf{x} - \mathbf{b}\ _2^2 + \frac{\rho}{2} \ \mathbf{x} - \mathbf{z}_k - \mathbf{u}_k\ _2^2$
4. $\mathbf{z}_{k+1} = S_{\lambda/\rho}(\mathbf{x}_{k+1} + \mathbf{u}_k)$
5. $\mathbf{u}_{k+1} = \mathbf{u}_k - \mathbf{x}_{k+1} + \mathbf{z}_{k+1}$
6. $\mathbf{k} \leftarrow \mathbf{k} + 1$
7. until some stopping criterion is satisfied.

Table 5.5 gives algorithmic steps of ADMM. Note that optimal value of regularization parameter λ is found by a search algorithm (e.g. cross-validation), since it governs sparsity of the solution indirectly [111,112]. This multiplies computation time by the number of trials for different λ values. When $\lambda \geq \|\mathbf{A}^H \mathbf{b}\|_\infty$, the solution of (5.4) becomes zero vector [34].

Convergence rate of ADMM depends strongly on the choice of Lagrangian penalty parameter, ρ . If ρ is selected suitably, the algorithm converges within a small number of iterations, while poor ρ values increases the number of iterations and slows down the convergence rate [128].

One stopping criterion for ADMM that can be found in the literature depends on primal and dual residuals of the optimization problem. At k^{th} iteration step, they are denoted by

$$\mathbf{e}_{p,k} = (\mathbf{x}_k - \mathbf{z}_k)$$

and

$$\mathbf{e}_{d,k} = -\rho(\mathbf{z}_k - \mathbf{z}_{k-1}),$$

respectively. The algorithm is stopped when the primal and dual residuals both satisfy predetermined stopping criteria that depends on imaging application. The stopping criteria can be chosen as $\|\mathbf{e}_{p,k}\|_2 \leq \epsilon^{\text{pri}}$ and $\|\mathbf{e}_{d,k}\|_2 \leq \epsilon^{\text{dual}}$ where

$$\begin{aligned}\epsilon^{\text{pri}} &= \sqrt{N}\epsilon^{\text{abs}} + \epsilon^{\text{rel}}\max\{\|\mathbf{x}_k\|_2, \|\mathbf{z}_k\|_2\}, \\ \epsilon^{\text{dual}} &= \sqrt{N}\epsilon^{\text{abs}} + \epsilon^{\text{rel}}\mu\|\mathbf{d}_k\|_2.\end{aligned}$$

Furthermore, $\epsilon^{\text{abs}} > 0$ and $\epsilon^{\text{rel}} > 0$ are the absolute and relative tolerances, respectively [128].

5.2.1.3 Application of FMM in ADMM

3rd step of ADMM algorithm solves a minimization problem and it will get computationally very demanding for a large-scale imaging problem. Here, we solve this minimization problem with an inner iteration by using CGLS, where multiplication of a vector with the observation matrix \mathbf{A} and its Hermitian \mathbf{A}^H are efficiently calculated by FMM formulation.

5.2.2 Constrained Split Augmented Lagrangian Shrinkage Algorithm (C-SALSA)

In [40] and [44], split augmented Lagrangian shrinkage algorithm (SALSA) is suggested to solve image restoration and reconstruction problems, which are in unconstrained form as given in (5.4). In SALSA, the problem is converted into constrained form by variable splitting and tackled by an augmented Lagrangian based method, specifically ADMM. C-SALSA, on the other hand, solves the constrained problem of (5.5) by converting it into an unconstrained problem. The conversion is realized by adding an indicator function of the feasible set

$\{x : \|\mathbf{Ax} - \mathbf{b}\| \leq \varepsilon\}$ into the objective function. The obtained unconstrained problem is then transformed into a new constrained problem with the application of variable splitting process, which is given as

$$\min_{\mathbf{x}} \phi(\mathbf{x}) \text{ subject to } \|\mathbf{Ax} - \mathbf{b}\| \leq \varepsilon \quad (5.32)$$

where $\phi(\mathbf{x})$ is a regularization function. It acts as a transform operator that is chosen with respect to the scattering characteristics of the imaged scene. For example, it can be chosen as l_1 -norm for point scatterers with background, while discrete gradient operator can be chosen for extended targets (a target that occupies more than one voxel), which has the following form:

$$\phi = \begin{bmatrix} D_x \\ D_y \\ D_z \end{bmatrix} \quad (5.33)$$

where D_x , D_y , and D_z denote difference operators along the respective directions. This operation is called “total variation (TV)” of the unknown and yields a reconstruction with sharp edges and boundaries of the targets are obtained without smoothing. TV is mathematically expressed as

$$TV(|\mathbf{x}|) = \sum_{i,j,k} |\nabla(|\mathbf{x}|)| \quad (5.34)$$

where

$$|\nabla(|\mathbf{x}|)| = \sqrt{D_x(|\mathbf{x}|)^2 + D_y(|\mathbf{x}|)^2 + D_z(|\mathbf{x}|)^2} \quad (5.35)$$

and

$$\begin{aligned} D_x(|\mathbf{x}|) &= |\mathbf{x}[i+1, j, k]| - |\mathbf{x}[i, j, k]|, \\ D_y(|\mathbf{x}|) &= |\mathbf{x}[i, j+1, k]| - |\mathbf{x}[i, j, k]|, \\ D_z(|\mathbf{x}|) &= |\mathbf{x}[i, j, k+1]| - |\mathbf{x}[i, j, k]| \end{aligned} \quad (5.36)$$

where $\mathbf{x}[i, j, k]$ is the i, j, k^{th} voxel of the imaged scene. There exist two variants of C-SALSA algorithm, depending on choice of the regularization function $\phi(\mathbf{x})$.

When $\phi(\mathbf{x}) = \|\mathbf{x}\|_1$, the constrained problem (5.32) can be solved by the first variant of C-SALSA, namely C-SALSA-1 algorithm and its steps are given in Table 5.6. On the other hand, when $\phi(\mathbf{x}) = TV(|\mathbf{x}|)$, the second variant of C-SALSA, namely C-SALSA-2, can be used for solving (5.32). Its algorithmic steps are given in Table 5.7. These two variants differ at their 3rd and 4th steps, where the regularization function is applied.

Table 5.6 Algorithmic steps of constrained split augmented Lagrangian shrinkage-I

Constrained Split Augmented Lagrangian Shrinkage Algorithm-1 (C-SALSA-1) [109]	
1.	Set $\mathbf{k} = \mathbf{0}$, choose $\rho > \mathbf{0}$, $\mathbf{z}_0^{(1)}$, $\mathbf{z}_0^{(2)}$, $\mathbf{d}_0^{(1)}$, $\mathbf{d}_0^{(2)}$
2.	repeat
3.	$\mathbf{r}_k = \mathbf{z}_0^{(1)} + \mathbf{d}_0^{(1)} + \mathbf{A}^H(\mathbf{z}_0^{(2)} + \mathbf{d}_0^{(2)})$
4.	$\mathbf{x}_{k+1} = (\mathbf{I} + \mathbf{A}^H \mathbf{A})^{-1} \mathbf{r}_k$
5.	$\mathbf{z}_{k+1}^{(1)} = \mathbf{S}_{1/\rho}(\phi \mathbf{x}_{k+1} - \mathbf{d}_k^{(1)}, \frac{1}{\rho})$
6.	$\mathbf{z}_{k+1}^{(2)} = \mathbf{b} + \begin{cases} \mathbf{A} \mathbf{x}_{k+1} - \mathbf{d}_k^{(2)} - \mathbf{b}, & \text{if } \ \mathbf{A} \mathbf{x}_{k+1} - \mathbf{d}_k^{(2)} - \mathbf{b}\ _2 \leq \varepsilon \\ \varepsilon \frac{(\mathbf{A} \mathbf{x}_{k+1} - \mathbf{d}_k^{(2)} - \mathbf{b})}{\ \mathbf{A} \mathbf{x}_{k+1} - \mathbf{d}_k^{(2)} - \mathbf{b}\ _2}, & \text{if } \ \mathbf{A} \mathbf{x}_{k+1} - \mathbf{d}_k^{(2)} - \mathbf{b}\ _2 > \varepsilon \end{cases}$
7.	$\mathbf{d}_{k+1}^{(1)} = \mathbf{d}_k^{(1)} - \mathbf{x}_{k+1} + \mathbf{z}_{k+1}^{(1)}$
8.	$\mathbf{d}_{k+1}^{(2)} = \mathbf{d}_k^{(2)} - \mathbf{A} \mathbf{x}_{k+1} + \mathbf{z}_{k+1}^{(2)}$
9.	$\mathbf{k} \leftarrow \mathbf{k} + \mathbf{1}$
10.	until some stopping criterion is satisfied.

Table 5.7 Algorithmic steps of constrained split augmented Lagrangian Shrinkage-II

Constrained Split Augmented Lagrangian Shrinkage Algorithm-2
(C-SALSA-2) [109]

1. Set $k = 0$, choose $\rho > 0$, $\mathbf{z}_0^{(1)}$, $\mathbf{z}_0^{(2)}$, $\mathbf{d}_0^{(1)}$, $\mathbf{d}_0^{(2)}$
 2. **repeat**
 3. $\mathbf{r}_k = \Phi^H(\mathbf{z}_0^{(1)} + \mathbf{d}_0^{(1)}) + \mathbf{A}^H(\mathbf{z}_0^{(2)} + \mathbf{d}_0^{(2)})$
 4. $\mathbf{x}_{k+1} = (\Phi^H\Phi + \mathbf{A}^H\mathbf{A})^{-1}\mathbf{r}_k$
 5. $\mathbf{z}_{k+1}^{(1)} = \mathcal{S}_{1/\rho}(\Phi\mathbf{x}_{k+1} - \mathbf{d}_k^{(1)}, \frac{1}{\rho})$
 6. $\mathbf{z}_{k+1}^{(2)} = \mathbf{b} + \begin{cases} \mathbf{Ax}_{k+1} - \mathbf{d}_k^{(2)} - \mathbf{b}, & \text{if } \|\mathbf{Ax}_{k+1} - \mathbf{d}_k^{(2)} - \mathbf{b}\|_2 \leq \varepsilon \\ \varepsilon \frac{(\mathbf{Ax}_{k+1} - \mathbf{d}_k^{(2)} - \mathbf{b})}{\|\mathbf{Ax}_{k+1} - \mathbf{d}_k^{(2)} - \mathbf{b}\|_2}, & \text{if } \|\mathbf{Ax}_{k+1} - \mathbf{d}_k^{(2)} - \mathbf{b}\|_2 > \varepsilon \end{cases}$
 7. $\mathbf{d}_{k+1}^{(1)} = \mathbf{d}_k^{(1)} - \Phi\mathbf{x}_{k+1} + \mathbf{z}_{k+1}^{(1)}$
 8. $\mathbf{d}_{k+1}^{(2)} = \mathbf{d}_k^{(2)} - \mathbf{Ax}_{k+1} + \mathbf{z}_{k+1}^{(2)}$
 9. $k \leftarrow k + 1$
 10. **until** some stopping criterion is satisfied.
-

5.2.2.1 Application of FMM in C-SALSA

As can be seen from Tables 5.6 and 5.7, the 3rd, 4th, 6th, and 8th steps of C-SALSA-1 and C-SALSA-2 algorithms consist of multiplication of a vector with the observation matrix \mathbf{A} and its Hermitian \mathbf{A}^H . Among all, 4th step is computationally most demanding one, since it contains the inversion of $(\Phi^H\Phi + \mathbf{A}^H\mathbf{A})$. We rewrite this step as follows

$$(\Phi^H\Phi + \mathbf{A}^H\mathbf{A})\mathbf{x}_{k+1} = \Phi^H(\Phi\mathbf{x}_{k+1}) + \mathbf{A}^H(\mathbf{Ax}_{k+1}) = \mathbf{r}_k. \quad (5.37)$$

Since \mathbf{r}_k is already known from 3rd step, solution of the linear system in (5.37) is more efficient and can be done iteratively. In this step, we apply two consecutive FMMs to evaluate $\mathbf{A}^H(\mathbf{A}\mathbf{x}_{k+1})$ operation, i.e.,

- 1st FMM $\rightarrow \mathbf{A}\mathbf{x}_{k+1}$
- 2nd FMM $\rightarrow \mathbf{A}^H(\cdot)$, where inside the parenthesis is the result of the 1st FMM operation.

It is not necessary to form the discrete gradient operators given in (5.36) explicitly. Instead, filtering the unknown vector \mathbf{x} with derivative kernel $[-1 \ 0 \ 1]$ along respective directions is computationally more efficient.

5.3 Numerical Examples

We considered two types of near-field imaging scenarios regarding the dimensionality of the targets: 1-D targets (point scatterers) and extended targets. The images are reconstructed using one of the augmented Lagrangian based algorithms (ADMM or C-SALSA) that fits best to the target characteristics. In all scenarios, plus-shaped MIMO array configuration is used. The operational frequency bandwidth (7 – 13 GHz band) is kept the same and number of frequency steps (1 GHz) are deliberately specified as low as possible so that we can investigate how the algorithms and sparsity constraint performs when the linear system has under-determined nature. Also, all targets are placed at the same distance ($y = 55$ cm) from the MIMO array so that imaging system will exhibit the same resolution capability for each of them. In order to demonstrate focusing capability of the sparsity-based algorithms, the same problems are also solved by conventional CGLS algorithm.

As illustrated in Fig. 5.6, incident signal power and signal-to-noise ratio is defined in the reconstructions as

$$S = N_T N_R N_F \left(\frac{1}{N_V} \sum_{\substack{q=1 \\ f_q \neq 0}}^{N_V} \frac{f_q}{R_{Tm,q}^2 R_{Rn,q}^2} \right). \quad (5.38)$$

$$SNR = 10 \log_{10} \left(\frac{S}{N} \right) \quad (5.39)$$

where the term in the parenthesis denotes the average power reflected back from the imaged scene. The total power is calculated by $N_T N_R N_F$ times this quantity, since imaging problem involves N_T transmitters, N_R receivers, and N_F frequency steps. Also, N_V denotes number of voxels. Note that this definition strongly depends on the shape and reflectivity distribution of the scene due to the fact that averaging is realized over only non-empty voxels.

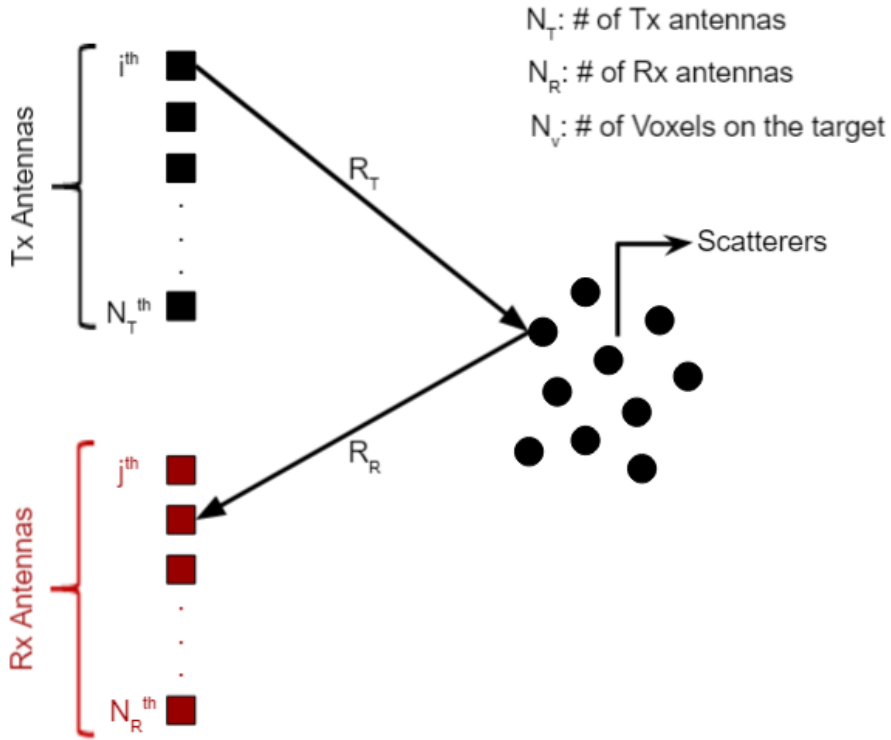


Figure 5.6. Illustration of incident signal power calculation.

In addition, quality assessment of the reconstructed images is realized by peak signal-to-noise ratio (PSNR), which is defined as

$$PSNR = 10 \log_{10} \left(\frac{MAX_I^2}{MSE} \right) \quad (5.40)$$

where, MAX_I is maximum pixel/voxel value of reconstructed reflectivity image and MSE is mean squared error which can be simply defined as the mean of the square

of the difference between the $m \times n$ actual image I and \hat{I} , which is the image reconstructed from the noisy measurement as

$$\text{MSE} = \frac{1}{mn} \sum_{i=1}^m \sum_{j=1}^n [I(i, j) - \hat{I}(i, j)]^2. \quad (5.41)$$

All simulations given below are realized with 30 dB input SNR unless otherwise is stated.

a. Point Scatterers

In all of the point scatterer scenarios demonstrated below, the related imaging problems are implemented based on (5.4) and solved using ADMM algorithm with the application of the FMM. Note that these problems can also be solved by C-SALSA-1 algorithm, however, we preferred to use ADMM in order to demonstrate applicability of FMM in different sparsity-based algorithms.

In the first scenario, a single point scatterer, as shown in Fig. 5.2(a), is considered. The image is reconstructed on a linear path parallel to x-axis, extending from $x = -12$ cm to $x = +12$ cm with 51 equal spatial steps, since they are placed on a line. In this way, it is aimed to obtain a short runtime. The reflectivity level of the point scatterer is set to 1. Fig. 5.7 plots normalized reconstructed 1-D solution with

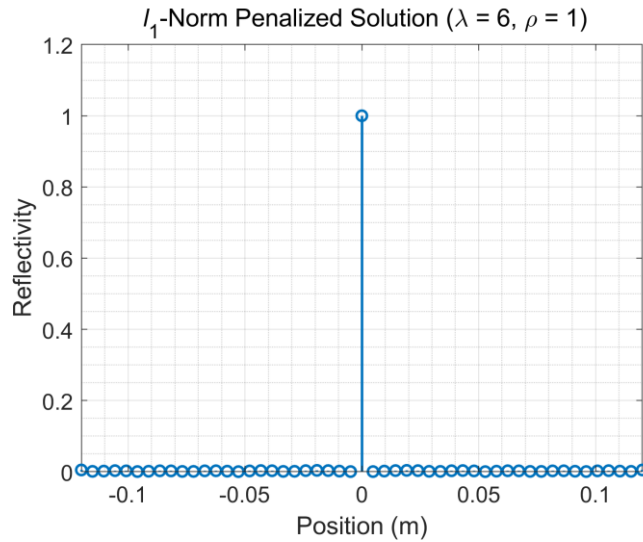


Figure 5.7. Normalized reconstructed solution for scattering from one point scatterer.

regularization parameter $\lambda = 6$ and penalty parameter $\rho = 1$. Unlike OMP, which has to carry out as many iteration steps as the predetermined sparsity level and does not guarantee a sparse solution, ADMM is able to converge to a solution with optimum sparsity (which corresponds to the sparsest solution for this example) under a standard stopping criterion.

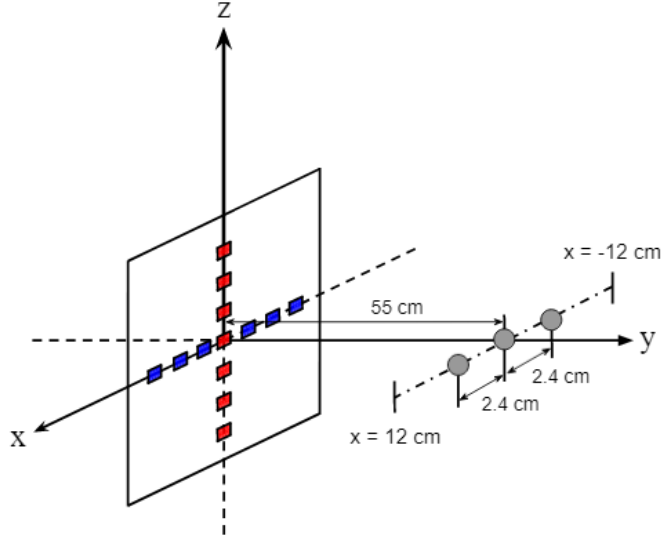


Figure 5.8. Imaging configuration for three point scatterers.

The second scenario contains an imaging problem with three point scatterers. Fig. 5.8 illustrates the corresponding imaging environment. The point scatterer at $x = 0$ m has reflectivity level of 1, while the scatterers at $x = 2.4$ cm and $x = -2.4$ cm have the reflectivity level of 0.5. 1-D solution is reconstructed on a linear path parallel to x-axis with the same length and spatial steps as in the previous numerical example. The problem is also solved by CGLS in order to demonstrate effectiveness of convex optimization technique.

The normalized solutions reconstructed by ADMM and CGLS are given in Fig. 5.9(a) and Fig. 5.9(b), respectively. As can be seen, the sparsest solution can be obtained using a convex optimization technique with regularization parameter $\lambda = 6$ and penalty parameter $\rho = 1$. On the other hand, in the CGLS solution, each point scatterer's reflectivity is reconstructed like a sinc function, and hence, sidelobes of

point scatterer with the highest reflectivity coincide with the main lobe of the adjacent ones. This leads to a solution where point scatterers are not resolved individually. The results indicate that theoretical cross range resolution, which is determined using Rayleigh criterion, can be achieved by convex optimization techniques. Besides, pSNRs are respectively calculated as 41.33 dB and 9.89 dB for ADMM and CGLS, supporting our findings.

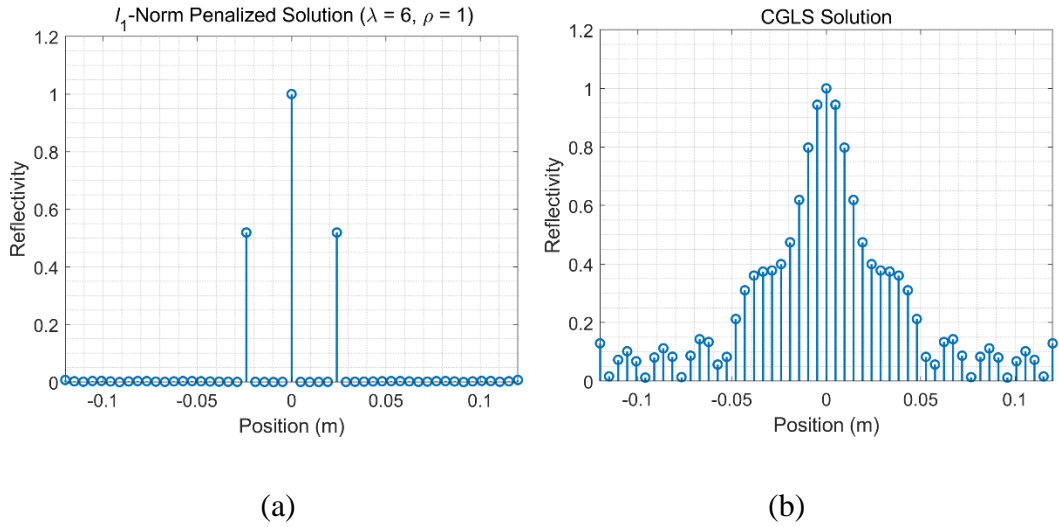


Figure 5.9. (a) ADMM solution and (b) CGLS solution.

Last scenario is based on point scatterers that are distributed on a plane. In this scenario, the imaged scene has an array of 9 point scatterers placed on a grid of 2.5 cm on x - and z -directions on $y = 55$ cm plane, as shown in Fig. 5.10. The reflectivity of the point scatterer at the center is set to 0.5, while the rest has a reflectivity of 1. Fig. 5.11(a) shows actual reflectivity image of the scene. The reconstructed images are formed on $y = 55$ cm with a resolution of 2.5 mm in both directions, yielding 1681 pixels in total. The reconstructions are normalized by the largest value and corresponding images obtained by CGLS and ADMM are given in Fig. 5.11(b) and Fig. 5.11(c). The resulting images show that resolving capability of the imaging system can be obtained using both CGLS and ADMM. However, when the problem is solved by ADMM, we can obtain a well-focused image as opposed to CGLS. This emphasizes the superior focusing performance of sparsity-based

algorithms. Finally, quality of the reconstructed images is quantitatively evaluated by calculating their PSNRs, which are 42.17 dB and 12.36 dB for ADMM and CGLS, respectively.

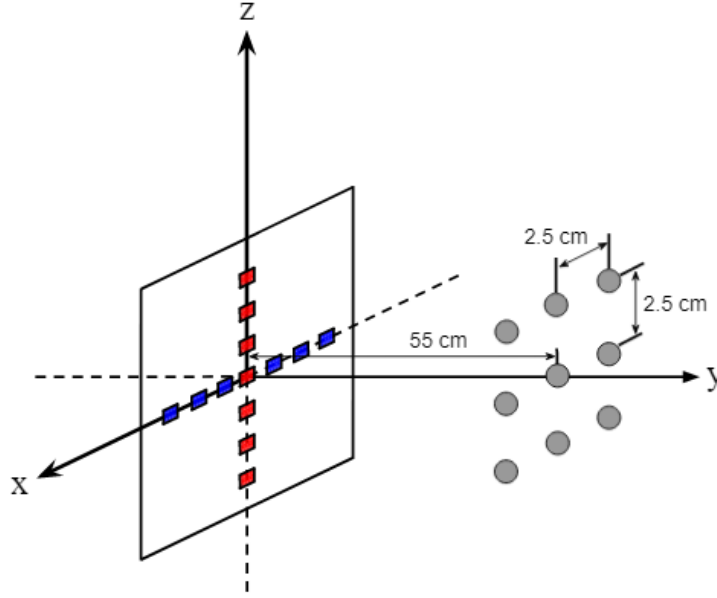


Figure 5.10. Imaging configuration for nine point scatterers.

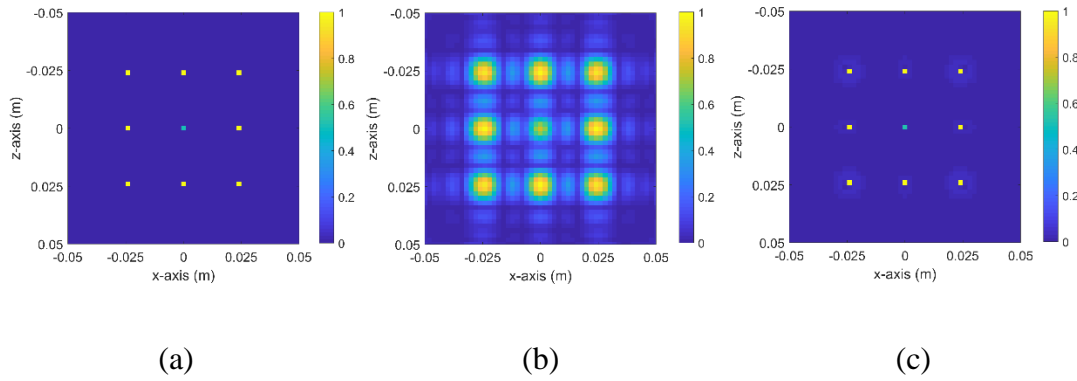


Figure 5.11. Imaging results for the first scenario: (a) Actual reflectivity of the point scatterers, (b) CGLS reconstruction, and (c) FMM-based ADMM reconstruction. The reconstructions are normalized by the largest value, therefore, they share the same colorbar.

b. Extended Targets

We investigate the extended targets in three categories: (i) 2-D targets in 2-D image space, (ii) 2-D targets in 3-D image space, and (iii) 3-D targets in 3-D image space. All imaging problems are implemented by (5.2) in the form

$$\min_{\mathbf{x}} TV(|\mathbf{x}|) \quad \text{subject to} \quad \|\mathbf{A}\mathbf{x} - \mathbf{b}\|_2 \leq \varepsilon$$

and they are solved by C-SALSA-2 algorithm with the use of FMM.

(i) 2-D targets in 2-D imaged space:

- Hexagonal Target

A hexagon-shaped target, whose true reflectivity image is given in Fig. 5.12(a), is imaged by the MIMO array. It is placed into a plane of size 40 cm \times 40 cm at $y = 55$ cm, and the image is reconstructed using 4 mm \times 4 mm pixels, giving 10201 pixels in total. Reflectivity characteristics of the target is specified as follows: Outer part's reflectivity is 1, while it is set to 0.6 for the inner parts except for U-shaped section, whose reflectivity is 0.4. Fig. 5.12(b) and Fig. 5.12(c) show the normalized reconstructed images obtained by CGLS and C-SALSA-2, respectively, where the color scale shows magnitude of the reflectivity distribution of the imaged scene along x - and z -directions.

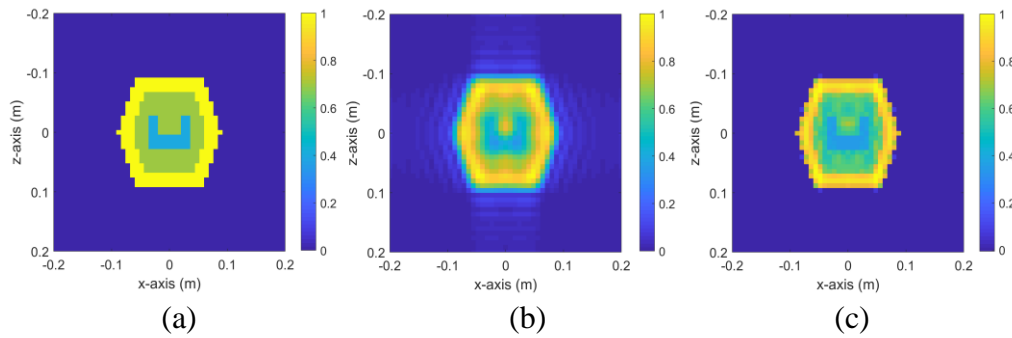


Figure 5.12. Imaging results for the hexagonal target: (a) Actual reflectivity of the hexagonal target, (b) CGLS reconstruction, and (c) FMM-based C-SALSA-2 reconstruction. The reconstructions are normalized by the largest value, therefore, they share the same color bar.

When CGLS is used, the boundaries of the target and U-shaped section are blurry in the reconstructed image. However, solving the problem using C-SALSA-2 algorithm with total variation constraint yields a well-focused image, which possesses all details of the target. Besides, background of the target is much clearer compared to CGLS reconstruction. The pSNRs are respectively calculated as 22.95 dB and 36.23 dB for CGLS and C-SALSA-2, which quantitatively supports our observations.

(ii) 2-D targets in 3-D imaged space:

- Rectangles

Three rectangles of size $8\text{ cm} \times 8\text{ cm}$ forms the image space as sketched in Fig. 5.13, and they are placed with 5 cm spacing along y -direction. Physical dimensions of the image space is $40\text{ cm} \times 40\text{ cm} \times 15\text{ cm}$ and it is roughly discretized by $8\text{ mm} \times 8\text{ mm} \times 2.5\text{ cm}$ voxels, giving 18207 voxels in total. Reflectivity value of each plane is selected as 1.0. 2-D cuts of the reconstructed 3-D image are given in Fig. 5.14 and Fig. 5.15, and the 3-D image is shown in Fig. 5.16. All of the 2-D images are normalized by the largest reflectivity value that is estimated within the imaged space. It must be noted that the color scale for 2-D images are not kept same to show small non-zero values between the layers.

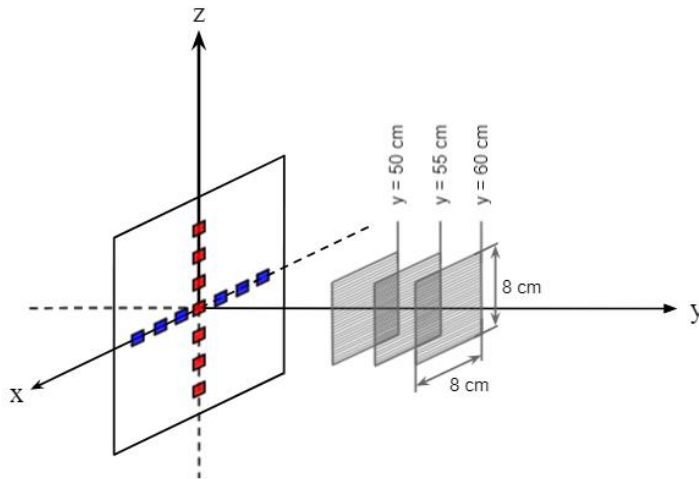


Figure 5.13. Imaging configuration for rectangular planes.

The reconstructed images of the rectangles are more focused and boundaries are sharper when the problem is solved by C-SALSA-2 algorithm. By reorganizing the solution vector in lexicographic order, 3-D image of the scene is constructed. Fig. 5.16 depicts the reconstructed rectangles in 3-D form, revealing that true shape of the targets can be acquired by C-SALSA-2 algorithm, whereas CGLS cannot yield a similar result. Surface of the rectangles are smoother, and their edges and vertices are more distinct, when the problem is solved with C-SALSA-2. Average reflectivity level on the planes that contain no scattering object (1st, 3rd, 5th, and 7th planes) is

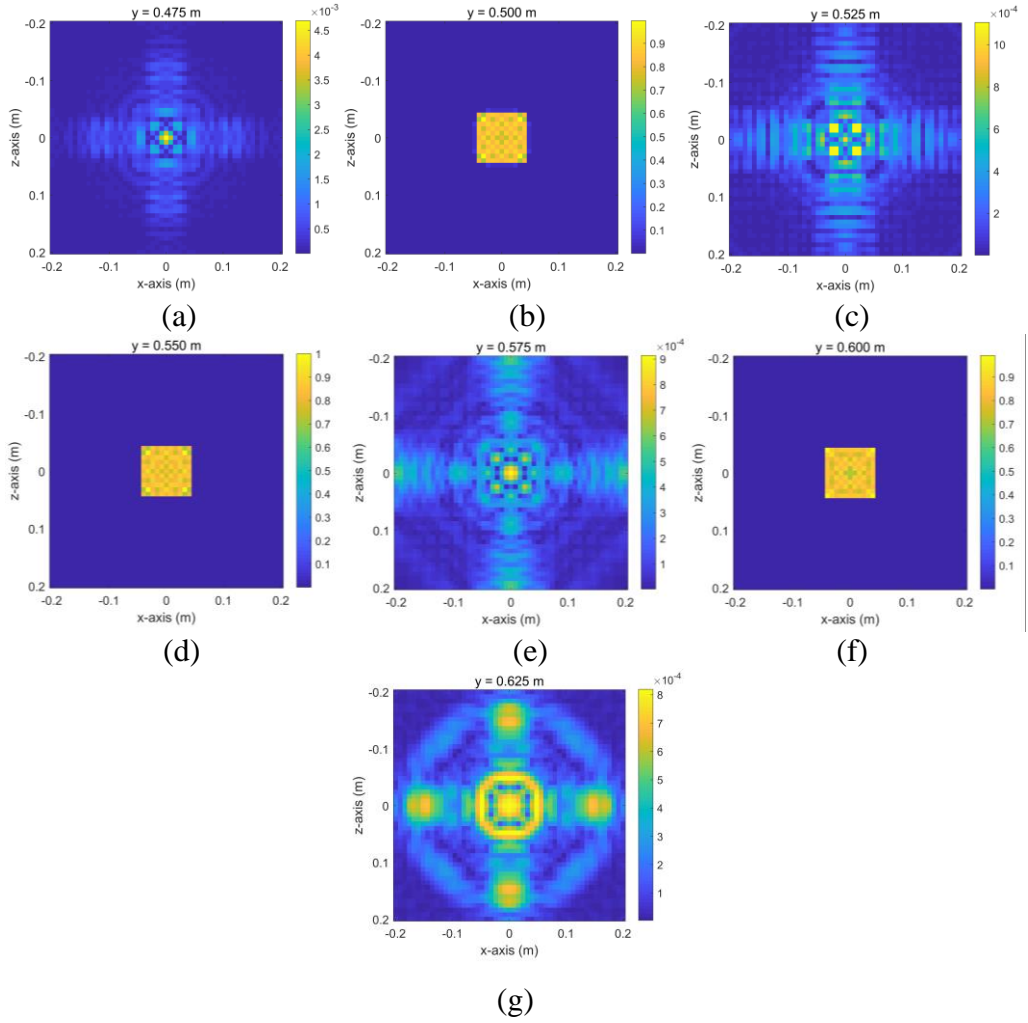


Figure 5.14. FMM-based C-SALSA-2 reconstructions belonging to the corresponding planes at (a) $y = 47.5$ cm, (b) $y = 50$ cm, (c) $y = 52.5$ cm, (d) $y = 55$ cm, (e) $y = 57.5$ cm, (f) $y = 60$ cm, and (g) $y = 62.5$ cm.

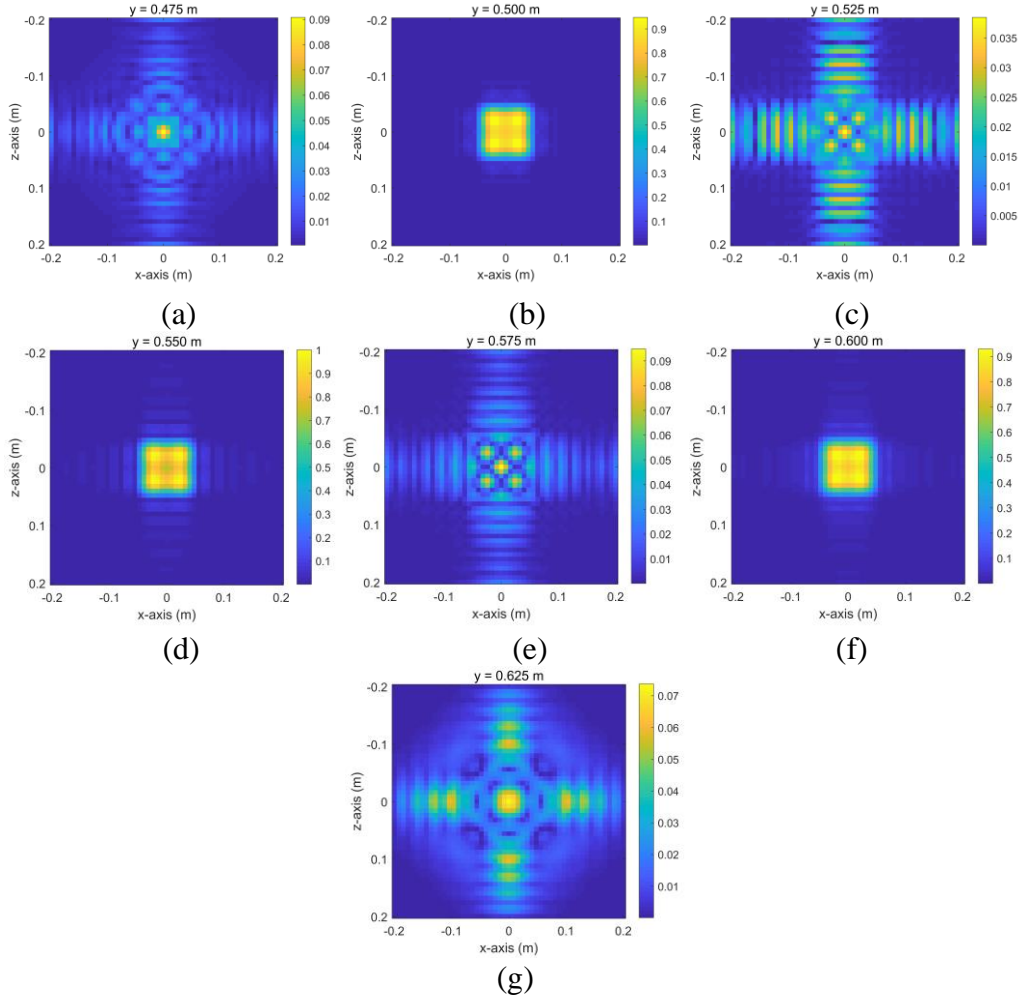


Figure 5.15. CGLS reconstructions belonging to the corresponding planes at (a) $y = 47.5$ cm, (b) $y = 50$ cm, (c) $y = 52.5$ cm, (d) $y = 55$ cm, (e) $y = 57.5$ cm, (f) $y = 60$ cm, and (g) $y = 62.5$ cm.

much smaller in C-SALSA-2 solution than those obtained by conventional CGLS ($\sim 15 \times 10^{-4}$ with C-SALSA-2 and ~ 0.092 with CGLS), leading to clearer 3-D reconstruction. Finally, calculated PSNRs are 35.44 dB and 19.67 dB for C-SALSA-2 and CGLS reconstructions, respectively.

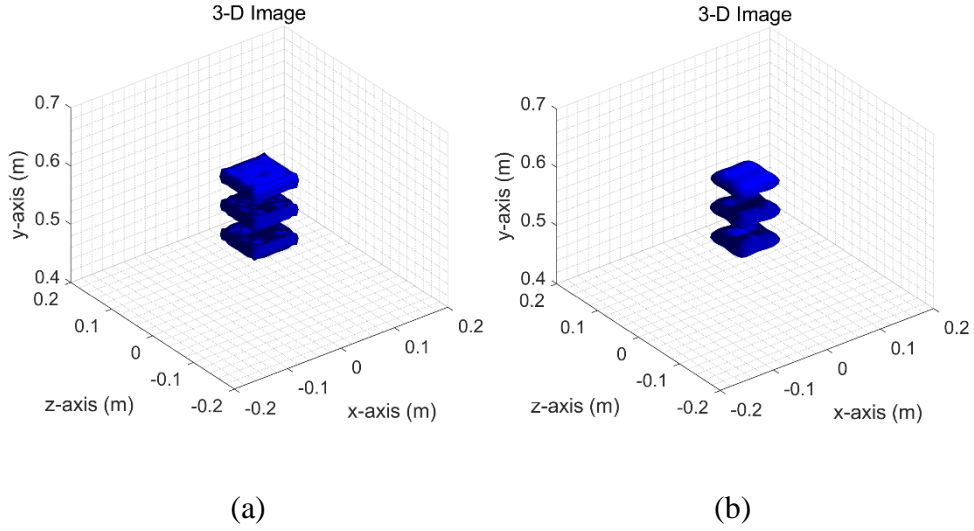


Figure 5.16. (a) FMM-based C-SALSA-2 solution and (b) CGLS solution.

(iii) 3-D targets in 3-D space

- Concentric Cylinders:

Three concentric cylinders, with their common axis along down-range direction, is placed between $y = 52.5$ cm and $y = 57.5$ cm planes. Diameters of the cylinders, from inner to outer, are 4 cm, 8 cm, and 12 cm, respectively, and corresponding reflectivity values are selected as 0.2, 0.6, 1.0. The image space is a volume of $40 \text{ cm} \times 40 \text{ cm} \times 25 \text{ cm}$ and roughly discretized by voxels of size $8 \text{ mm} \times 8 \text{ mm} \times 2.5 \text{ cm}$, giving 28611 voxels overall. The target's image is first provided as 2-D cuts of the cross-sections ($y = 52.5$ cm, $y = 55$ cm, and $y = 57.5$ cm), and then as a 3-D reconstruction. The first column of Fig. 5.17 depicts actual reflectivity distributions on each slice, while the second and the third columns show images reconstructed using CGLS and C-SALSA-2, respectively. In addition, C-SALSA-2 solution is arranged lexicographically to give a 3-D image of the target, which is shown in Fig. 5.18.

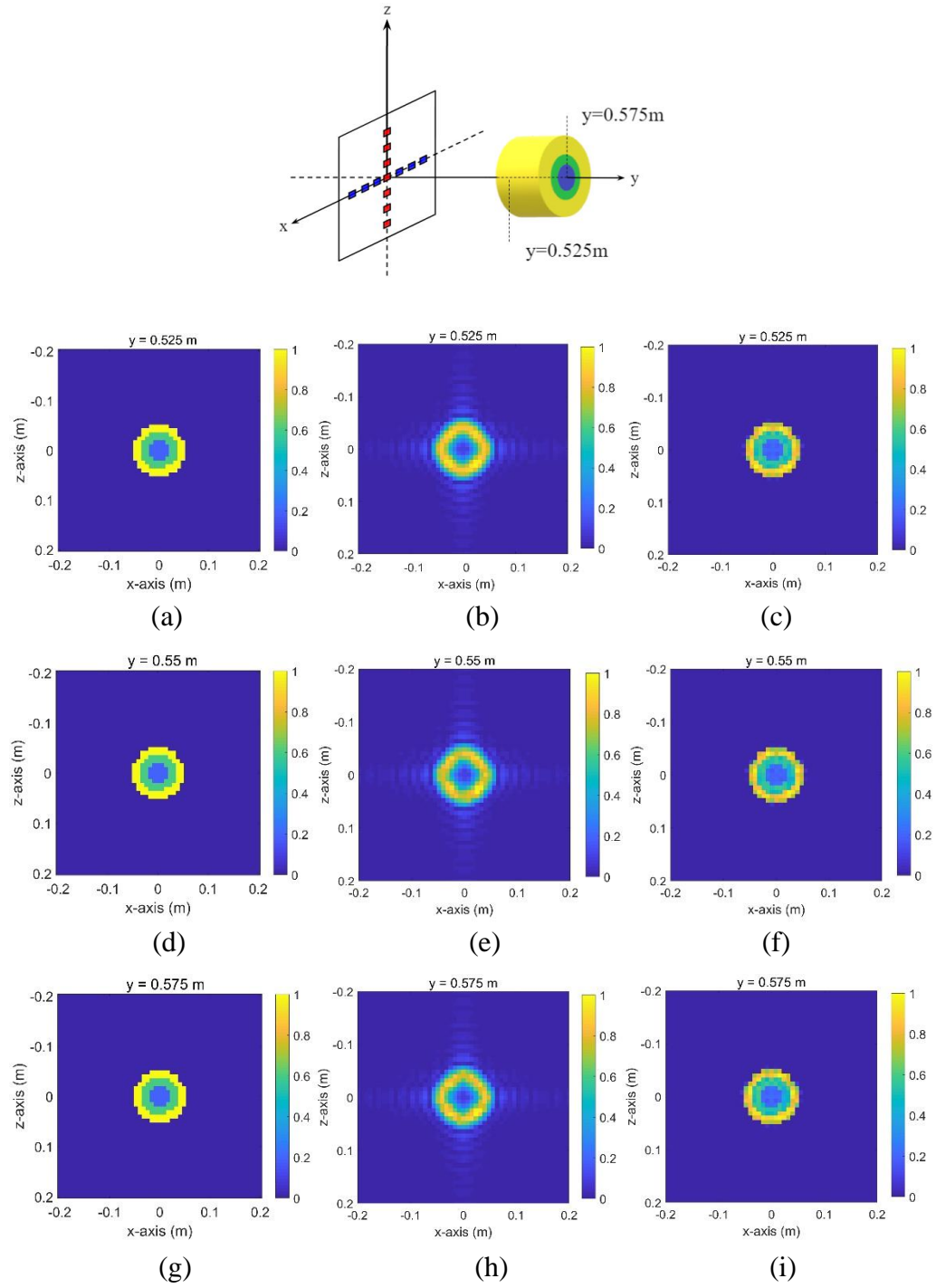


Figure 5.17. Reconstructed images of the concentric cylinders. The left, the middle and the right columns respectively show actual reflectivity of the cylinders, CGLS reconstruction and FMM-based C-SALSA-2 reconstruction.

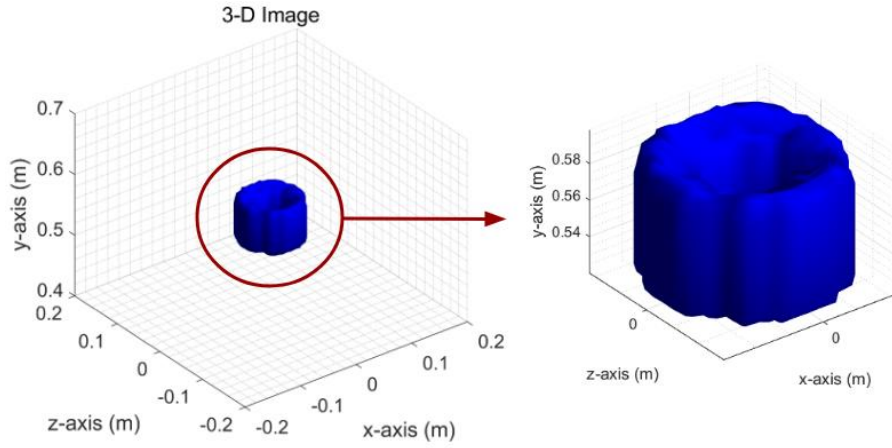


Figure 5.18. 3-D reconstruction of the concentric cylinders.

5.4 Additional Analysis

Performance of the FMM-based sparse reconstruction is further investigated by simulating the imaging problems with different input SNRs. For this purpose, CGLS and C-SALSA-2 reconstructions with concentric cylinders are repeated, each time reducing input SNR from 50 dB to 0 dB in 5 dB steps. Fig. 5.19 shows pSNR as a function of input SNR, revealing the behavior of both algorithms in the presence of

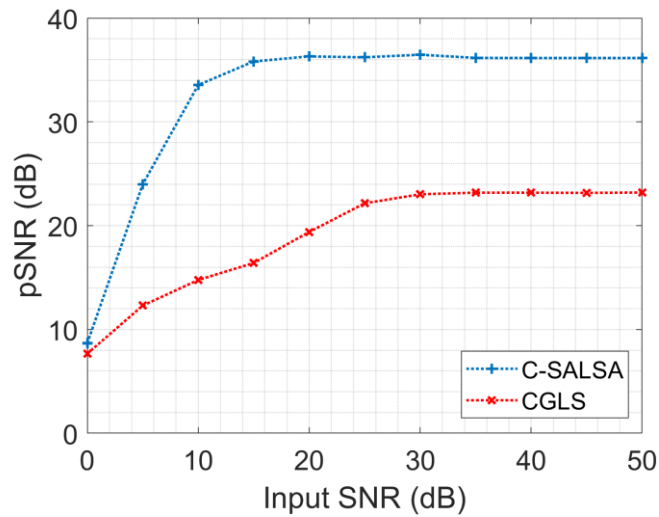


Figure 5.19. Performance of the sparsity-based reconstruction in the presence of noise, when compared to CGLS.

noise. As can be seen, C-SALSA-2 is capable of providing pSNR above 20 dB, although input SNR is 5 dB. On the other hand, the performance of CGLS is not very good in the presence of noise in the input signal, since it lacks regularization term and corresponding pSNR continuously deteriorates as the input SNR reduces below 25 dB.

Finally, in order to demonstrate the improvement that FMM grants on the solutions, the imaging problems are re-simulated for different number of antennas. Fig. 5.20 plots CPU time (in seconds) and memory requirement (in MBytes) as a function of number of antennas (i.e., $N_T = N_R$). As expected, the graphs show that FMM provides reduced CPU time and lower memory usage with $O(N_T + N_R)$ above a crossover point, when compared to direct matrix-vector product method, which is proportional to $O(N_T \times N_R)$. It must be noted that the crossover point depends on several things such as the type of imaging geometry, structure of the forward problem, how the FMM is truncated, etc. Note that Fig. 5.20(b) plots the average memory usage that is monitored on the task manager during runtime.

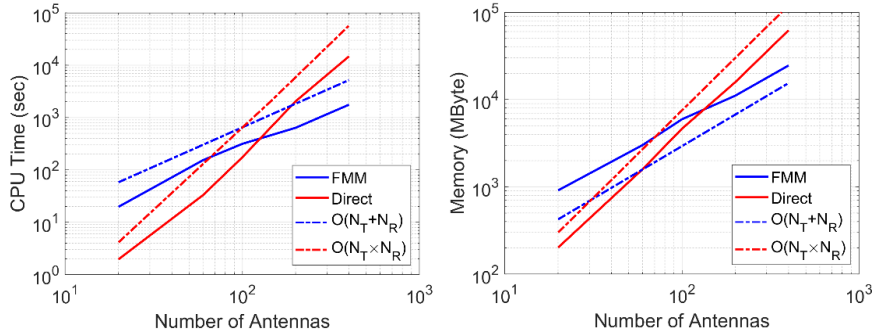


Figure 5.20. Comparison of the FMM and direct matrix-vector product in terms of (a) CPU time and (b) memory.

Although the sparse solution can be mathematically accelerated, the improvement depends on the number of antennas on the MIMO array. It is practically not feasible to continuously increase the number of antennas due to hardware considerations. In order to exploit the power of the FMM efficiently, we need to take multiple reflections among the voxels into account, which are ignored in our solutions so far.

CHAPTER 6

DISCRETE DIPOLE APPROXIMATION

In order to calculate multiple reflections among the voxels, we preferred using “Discrete Dipole Approximation” (DDA) method. DDA method was first introduced by Purcell and Pennypacker [113] to model the scattering from arbitrarily-shaped targets and has been applied to various scattering problems, ranging from graphite grains [114] to porous dust particles [115,116]. DDA simply replaces the solid target by an array of dipoles, which are in interaction with each other and spacing between them is smaller than wavelength. Each dipole possesses a dipole moment in response to incident plane wave and fields scattered from all other dipoles. A consistent solution for the dipole moments can be acquired as a solution to the resulting matrix equation, which is a set of coupled linear equations [114].

On the contrary to the previous chapters, $e^{-i\omega t}$ time convention is used for the mathematical background of DDA and FMM formulation throughout this chapter.

6.1 Mathematical Background

An object with the properties $Y_1 = \sigma_1 - i\omega\epsilon_1$ and $Z_1 = -i\omega\mu_1$ occupies a volume V in an infinite space with the properties $Y_0 = \sigma_0 - i\omega\epsilon_0$ and $Z_0 = -i\omega\mu_0$, and sources \mathbf{J}^0 and \mathbf{M}^0 . Outside the volume V , total fields satisfy Maxwell’s equations by [117]

$$\nabla \times \mathbf{E} = -Z_0 \mathbf{H} - \mathbf{M}^0 \quad (6.1)$$

and

$$\nabla \times \mathbf{H} = Y_0 \mathbf{E} + \mathbf{J}^0, \quad (6.2)$$

whereas inside the volume V , the equations are

$$\nabla \times \mathbf{E} = -Z_1 \mathbf{H} \quad (6.3)$$

and

$$\nabla \times \mathbf{H} = -Y_1 \mathbf{E}. \quad (6.4)$$

Equations (6.3) and (6.4) can be rewritten by

$$\nabla \times \mathbf{E} = -Z_0 \mathbf{H} - \mathbf{M}^1 \quad (6.5)$$

and

$$\nabla \times \mathbf{H} = Y_0 \mathbf{E} + \mathbf{J}^1, \quad (6.6)$$

respectively, where \mathbf{J}^1 and \mathbf{M}^1 are the equivalent sources within the volume V , replacing the actual scattering object. The scattered fields, then, can be obtained by auxiliary vector potentials \mathbf{A}^s and \mathbf{F}^s

$$\mathbf{A}^s = \frac{\mu_0}{4\pi} \int \frac{\mathbf{J}^1(\mathbf{r}') e^{ik_0 R}}{R} dV', \quad (6.7)$$

$$\mathbf{F}^s = \frac{\epsilon_0}{4\pi} \int \frac{\mathbf{M}^1(\mathbf{r}') e^{ik_0 R}}{R} dV' \quad (6.8)$$

where $R = |\mathbf{r} - \mathbf{r}'|$ is the distance from the source point \mathbf{r}' to the observation point \mathbf{r} . If the object is much smaller than the wavelength, (6.7) and (6.8) can be approximated by

$$\mathbf{A}^s = \frac{\mu_0}{4\pi} \frac{\mathbf{J}^1 e^{ik_0 R}}{R} V \quad (6.9)$$

and

$$\mathbf{F}^s = \frac{\epsilon_0}{4\pi} \frac{\mathbf{M}^1 e^{ik_0 R}}{R} V, \quad (6.10)$$

respectively. The vector potentials of electric and magnetic dipoles are written as

$$\mathbf{A} = \frac{-i\omega\mu_0}{4\pi} \mathbf{p} \frac{e^{ik_0 R}}{R} \quad (6.11)$$

and

$$\mathbf{F} = \frac{-i\omega\epsilon_0}{4\pi} \mathbf{m} \frac{e^{ik_0 R}}{R}. \quad (6.12)$$

Equations (6.11) and (6.12), when compared to (6.9) and (6.10), indicate that a small scatterer can be represented by electric and magnetic dipoles whose moments are

$$\mathbf{p} = \frac{\mathbf{J}^1 V}{-i\omega} \quad (6.13)$$

and

$$\mathbf{m} = \frac{\mathbf{M}^1 V}{-i\omega}, \quad (6.14)$$

respectively. It is an important result that (6.13) and (6.14) do not depend on the shape of the object.

DDA is based on evaluating (6.9) and (6.10) by applying Riemann sums. Dividing the volume V into N sub-volumes (dimensions of each is much smaller than the wavelength), these equations can be approximated by

$$\mathbf{A}^S \approx \frac{-i\omega\mu_0}{4\pi} \sum_i \frac{e^{ik_0 R}}{R} \mathbf{p}_i dV_i \quad (6.15)$$

$$\mathbf{F}^S \approx \frac{-i\omega\epsilon_0}{4\pi} \sum_i \frac{e^{ik_0 R}}{R} \mathbf{m}_i dV_i. \quad (6.16)$$

Apparently, (6.15) and (6.16) replace each sub-volume by electric and magnetic dipoles, respectively.

6.2 Formulation

Let $\mu_{d,i} = \mu_0$ and $\epsilon_{d,i}$ ($i = 1, \dots, N$) be constitutional parameters belonging to N small dielectric (non-magnetic) scatterers, which are replaced by dipoles with dipole moments \mathbf{p}_i and dipole polarizabilities α_i located at \mathbf{r}_i . Total field impinging on the j^{th} dipole can be written as [117]

$$\mathbf{E}(\mathbf{r}_j) = \mathbf{E}^{inc}(\mathbf{r}_j) + \sum_{\substack{i=1 \\ i \neq j}}^N \mathbf{E}_i^{sca}(\mathbf{r}_j) \quad (6.17)$$

where $\mathbf{E}_i^{sca}(\mathbf{r}_j)$ is the field at \mathbf{r}_j that is scattered by i^{th} dipole and it is mathematically expressed as

$$\mathbf{E}_i^{sca}(\mathbf{r}_j) = \frac{i\omega}{k_0^2} [k_0^2 + \nabla\nabla] \mathbf{A} = \frac{1}{4\pi\epsilon_0} [k_0^2 + \nabla\nabla] \frac{e^{ik_0 r_{ij}}}{r_{ij}} \mathbf{p}_i. \quad (6.18)$$

The polarizability α is what relates dipole moment \mathbf{p} to electric field \mathbf{E} induced on a small scatterer in the form of

$$\mathbf{p} = \alpha \mathbf{E}. \quad (6.19)$$

When (6.17) is multiplied by α_j , we have

$$\mathbf{p}_j = \alpha_j \mathbf{E}^{inc}(\mathbf{r}_j) - \sum_{\substack{i=1 \\ i \neq j}}^N \frac{\alpha_j k_0^3}{4\pi\epsilon_0} \left[\bar{\mathbf{I}} + \frac{\nabla\nabla}{k_0^2} \right] \frac{e^{jk_0 r_{ij}}}{r_{ij}} \mathbf{p}_i, \quad (6.20)$$

which yields a linear system with N linear equations and N unknowns. The same procedure can also be followed for small magnetic scatterers to find magnetic dipole moments, which is given as

$$\mathbf{m}_j = \beta_j \mathbf{H}^{inc}(\mathbf{r}_j) - \frac{\beta_j k_0^3}{4\pi\mu_0} \left[\bar{\mathbf{I}} + \frac{\nabla\nabla}{k_0^2} \right] \frac{e^{ik_0 r_{ij}}}{r_{ij}} \mathbf{m}_i \quad (6.21)$$

with β_j being magnetic polarizability.

6.3 Polarizability (α)

In DDA, it is significant to establish a relation between the relative dielectric constant of the scattering medium and the polarizabilities. Purcell and Pennypacker used Clausius-Mosotti (CM) relation [113]

$$\alpha^{(0)} = 4\pi a^3 \epsilon_0 \frac{\epsilon_r - 1}{\epsilon_r + 2} \quad (6.22)$$

in their original work, where each dipole is represented by a dielectric sphere of radius a and relative permittivity of ϵ_r . Note that this relation is exact in the zero-frequency limit ($k_0 a \rightarrow 0$) [118].

In [114], Draine showed that radiative reaction correction, which is neglected in (6.22), can be included in the relation when $k_0 a$ is finite, hence, the polarizability is obtained by

$$\alpha = \frac{\alpha^{(nr)}}{1 - \frac{i}{6\pi\epsilon_0} \frac{\alpha^{(nr)}}{a^3} (k_0 a)^3} \quad (6.23)$$

where $\alpha^{(nr)}$ is the polarizability without radiative reaction correction, namely non-radiative polarizability. Draine suggested using the following relation to substitute $\alpha^{(nr)}$ in (6.23) [114]

$$\alpha^{(nr)} \approx \alpha^{(0)} \quad (6.24)$$

therefore, (6.23) can be referred to as Classius-Mosotti plus radiative reaction (CMRR).

In [119,120], vector integral equation was discretized using the method of moments and it was demonstrated that this approach is equivalent to DDA except for the definition of polarizabilities. In regard to this approach, $\alpha^{(nr)}$ can be substituted as

$$\alpha^{(nr)} \approx \frac{\alpha^{(0)}}{1 + b_1 (\alpha^{(0)}/a^3) (k_0 a)^2} \quad (6.25)$$

where

$$b_1 = -\left(\frac{4\pi}{3}\right)^{(1/3)} \frac{1}{4\pi\epsilon_0} \quad (6.26)$$

and this relation is called vector integral equation formulation (VIEF).

The most popular form of $\alpha^{(nr)}$ was developed by Draine and Goodman, namely lattice dispersion relation, in 1993 and it is given as [121]

$$\alpha^{(nr)} \approx \frac{\alpha^{(0)}}{1 + (\alpha^{(0)}/a^3) [c_1 + \epsilon_r c_2 + \epsilon_r c_3 S] (k_0 a^2)} \quad (6.27)$$

where

$$c_1 = -\frac{1.8915316}{4\pi\epsilon_0}$$

$$c_2 = \frac{0.168469}{4\pi\epsilon_0}$$

$$c_3 = -\frac{1.7700004}{4\pi\epsilon_0}$$

and $S \equiv \sum_{j=1}^3 (\hat{a}_{d,j} \cdot \hat{a}_{p,j})^2$ is a term that carries information about direction and polarization of the incident plane wave with $\hat{a}_{d,j}$ and $\hat{a}_{p,j}$ being unit vectors for direction and polarization, respectively. For randomly oriented dipoles, expected value of S is $1/5$ and the relation will be called “isotropized lattice dispersion relation (ILDR)” [117].

6.4 Implementation of DDA

Let \mathbf{E}_j be the total electric field impinging on a dipole at location \mathbf{r}_j due to the incident electric field $\mathbf{E}_{inc,j}$ and the electric fields scattered from the rest of the dipoles. Using (6.17) and (6.18), a linear system can be constructed in the following form:

$$\mathbf{E}_j = \mathbf{E}_{inc,j} - \sum_{k \neq j} \mathbf{A}_{jk} \mathbf{P}_k \quad (6.28)$$

where \mathbf{A}_{jk} is the tensor with off-diagonal elements of interaction matrix \mathbf{A} , representing the interaction between receiving dipole at \mathbf{r}_j and scattering dipole at \mathbf{r}_k . This off-diagonal block can mathematically be expressed as

$$\mathbf{A}_{jk} = \frac{\exp(jkr_{jk})}{r_{jk}} \left[k^2 (\mathbf{r}_{jk} \mathbf{r}_{jk} - \mathbf{I}_3) + \frac{jkr_{jk}-1}{r_{jk}^2} (3\mathbf{r}_{jk} \mathbf{r}_{jk} - \mathbf{I}_3) \right], j \neq k \quad (6.29)$$

where r_{jk} is the distance from \mathbf{r}_j to \mathbf{r}_k and \mathbf{r}_{jk} is the unit vector in the direction from \mathbf{r}_j to \mathbf{r}_k . From (6.19), diagonal terms can be defined as

$$\mathbf{A}_{jj} = \alpha_j^{-1}, \quad (6.30)$$

Figure 6.1. System of equations for DDA.

which can be substituted into (6.28) as

$$\mathbf{E}_{inc,j} = \mathbf{A}_{jj}\mathbf{p}_j + \sum_{k \neq j} \mathbf{A}_{jk}\mathbf{p}_k. \quad (6.31)$$

The terms \mathbf{A}_{jj} and \mathbf{A}_{jk} can be combined into the same matrix \mathbf{A} since their non-zero entries do not overlap. Resulting linear system is well-determined, containing $3N$ coefficients of the N dipoles \mathbf{p}_j yielding $3N$ linear equations. Fig. 6.1 illustrates the resulting matrix equation.

For clarification, \mathbf{A}_{12} is the tensor that represents the interaction between spatial components of the receiving dipole at \mathbf{r}_1 and scattering dipole at \mathbf{r}_2 . \mathbf{A}_{12} can be defined as

$$\mathbf{A}_{12} = -\frac{k_0^2 \exp(ik_0 r_{12})}{r_{12}} \begin{bmatrix} \beta_{12} + \gamma_{12} r_{12,x}^2 & \gamma_{12} r_{12,x} r_{12,y} & \gamma_{12} r_{12,x} r_{12,z} \\ \gamma_{12} r_{12,y} r_{12,x} & \beta_{12} + \gamma_{12} r_{12,y}^2 & \gamma_{12} r_{12,y} r_{12,z} \\ \gamma_{12} r_{12,z} r_{12,x} & \gamma_{12} r_{12,z} r_{12,y} & \beta_{12} + \gamma_{12} r_{12,z}^2 \end{bmatrix} \quad (6.32)$$

where

$$r_{12} = [(x_1 - x_2)^2 + (y_1 - y_2)^2 + (z_1 - z_2)^2]^{1/2}, \quad (6.33)$$

$$r_{12,x} = \frac{x_1 - x_2}{r_{12}}, \quad r_{12,y} = \frac{y_1 - y_2}{r_{12}}, \quad r_{12,z} = \frac{z_1 - z_2}{r_{12}} \quad (6.34)$$

$$\beta_{12} = [1 - (k_0 r_{12})^{-2} + j(k_0 r_{12})^{-1}], \quad (6.35)$$

and

$$\gamma_{12} = [1 - 3(k_0 r_{12})^{-2} + 3j(k_0 r_{12})^{-1}]. \quad (6.36)$$

Once the linear equations given in Fig. 6.1 are solved, the scattered electric field at any point \mathbf{r} , which is relative to the origin, can be calculated by

$$\mathbf{E}_{sca}(k_0 \mathbf{r}) = \frac{1}{4\pi\epsilon_0} \left\{ k_0^2 (\mathbf{r} \times \mathbf{p}) \times \mathbf{r} \frac{e^{ik_0 r}}{r} + [3\mathbf{r}(\mathbf{r} \cdot \mathbf{p}) - \mathbf{p}] \left(\frac{1}{r^3} - \frac{ik_0}{r^2} \right) e^{ik_0 r} \right\}, \quad (6.37)$$

while in the far-zone ($\hat{r} \gg \hat{r}_{jk}$), the $1/r^2$ and $1/r^3$ terms in (6.37) can be neglected since they rapidly diminish with increasing distance. The scattered electric field in the far zone approximates to

$$\mathbf{E}_{sca}(k_0 \mathbf{r}) = \frac{1}{4\pi\epsilon_0} \left\{ k_0^2 (\mathbf{r} \times \mathbf{p}) \times \mathbf{r} \frac{e^{ik_0 r}}{r} \right\}. \quad (6.38)$$

After calculating the scattered field, total field can be determined by the superposition of the incident and the scattered fields as follows

$$\mathbf{E}_{total}(k_0 \mathbf{r}) = \mathbf{E}_{inc}(k_0 \mathbf{r}) + \mathbf{E}_{sca}(k_0 \mathbf{r}). \quad (6.39)$$

6.4.1 Numerical Example

For demonstrating DDA, we considered scattering from a homogeneous lossy dielectric cube with $\epsilon_r = 2.88 + 0.34i$ and it is discretized by 1728 dipoles placed on a cubic lattice with a spacing of $d = 0.1 \lambda$ ($f = 10$ GHz), as shown in Fig. 6.2(a). When the distance between the dipoles is d , each dipole can be approximated by a dielectric sphere of volume d^3 and its radius is defined as

$$a = \left(\frac{3}{4\pi} \right)^{(1/3)} d.$$

For a linearly polarized incident plane wave propagating in y -direction, the scattering problem is implemented in MATLAB and solved using CGLS for all polarizability descriptions (CM, ILDR, VIEF, CMRR). The solution is obtained by

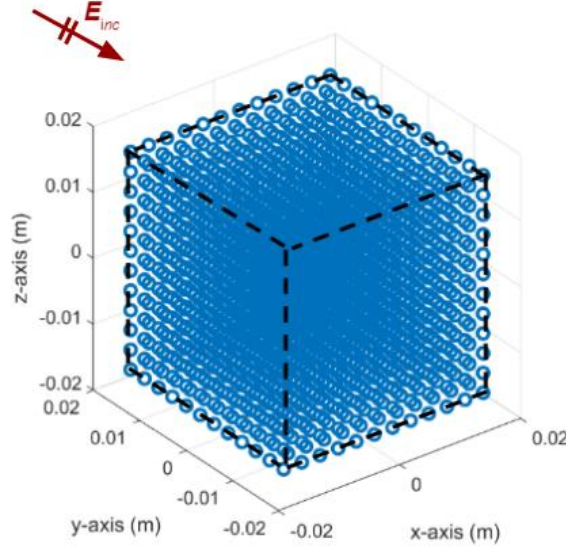


Figure 6.2. Discretized dielectric cube.

iterating CGLS till $|\mathbf{A} \cdot \mathbf{P} - \mathbf{E}_{inc}| < 10^{-3} |\mathbf{E}_{inc}|$ is satisfied. Then, the scattered electric field in the far-zone is calculated using (6.38). Furthermore, in order to validate the accuracy of DDA, the same scattering problem is modeled and simulated in HFSS. Fig. 6.3 plots far-zone scattered electric fields in elevation plane ($\varphi = 90^\circ$), which are derived by DDA formulation, and compare them with the solutions obtained in HFSS. As can be seen, DDA and related polarizability definitions are in good agreement with HFSS, while VIEF gives the closest result.

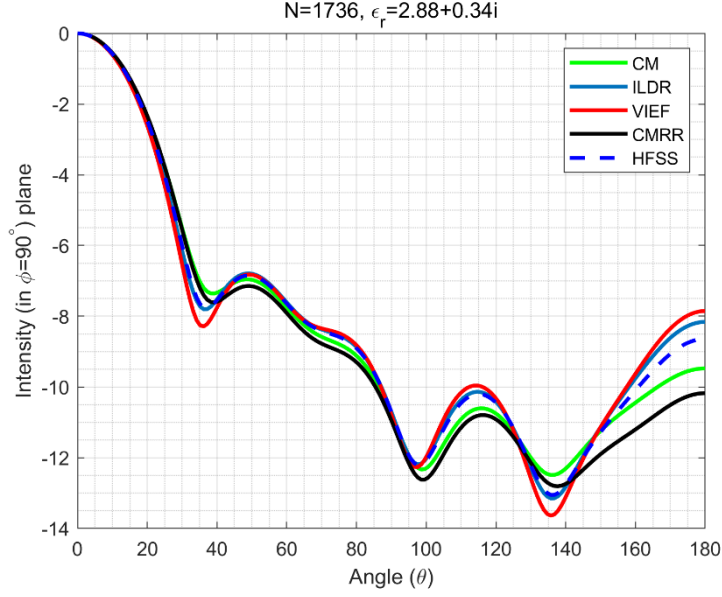


Figure 6.3. Far-zone scattered electric field calculated with CM, ILDR, VIEF, and CMRR (in comparison with HFSS).

6.5 DDA in Near-Field MIMO Imaging

Treating radar imaging problem as an actual electromagnetic scattering phenomenon allows us to investigate how quality of the reconstructions change, when multiple reflections are introduced into the solution.

In DDA, the incident electric field illuminating the target (dipole array) is generally presumed to be a plane wave. However, for a practical cases such as radar imaging, antenna elements of the array exhibit different radiation characteristics (e.g. radiation pattern, directivity, polarization, etc.).

Suppose that transmitting and receiving sub-arrays of the MIMO array is composed of Hertzian dipole antennas. The mathematical expression of the incident electric field that is radiated by the i^{th} Hertzian dipole antenna upon the j^{th} dipole on the target at the l^{th} frequency step is written as

$$\mathbf{E}^{inc}_{i,j} = \mathbf{a}_p i\eta \frac{k_n I_0 e^{ik_l R_{Ti,j}}}{4\pi R_{Ti,j}} \sin\theta_{i,j} \quad (6.40)$$

where, \mathbf{a}_p is unit vector of the incident field, η is intrinsic impedance of the medium, k_l is wavenumber at l^{th} frequency step, $R_{Ti,j}$ is distance between the i^{th} transmitting antenna and the j^{th} dipole, and $\theta_{i,j}$ is angle between the i^{th} transmitting antenna and the j^{th} dipole in elevation plane. Solving the matrix equation in Fig. 6.1 with \mathbf{E}^{inc} as in (6.40) gives an equivalent dipole moment distribution, thus, received electric field \mathbf{E}^{rec} measured at each receiving antenna can be calculated using (6.38). Note that the solution of the matrix equation and calculation of \mathbf{E}^{rec} must be repeated for each transmitting antenna and frequency step. Mathematical expression of \mathbf{E}^{rec} is given below

$$\mathbf{E}^{rec}_{j,m}(k_n \mathbf{r}_m) = \frac{1}{4\pi\epsilon_0} \left\{ k_l^2 (\mathbf{r}_m \times \mathbf{p}) \times \mathbf{r}_m \frac{e^{ik_l r}}{r} \right\} \quad (6.41)$$

where, \mathbf{r}_m is the receiving antenna position that is relative to the origin. We can rearrange the interaction matrix in the following form

$$\begin{aligned} & [A_l]_{[3N \times N_T \times N_R] \times 3N} \\ &= \begin{bmatrix} [A_{l,xx}]_{[N \times N_T \times N_R] \times N} & [A_{l,xy}]_{[N \times N_T \times N_R] \times N} & [A_{l,xz}]_{[N \times N_T \times N_R] \times N} \\ [A_{l,yx}]_{[N \times N_T \times N_R] \times N} & [A_{l,yy}]_{[N \times N_T \times N_R] \times N} & [A_{l,yz}]_{[N \times N_T \times N_R] \times N} \\ [A_{l,zx}]_{[N \times N_T \times N_R] \times N} & [A_{l,zy}]_{[N \times N_T \times N_R] \times N} & [A_{l,zz}]_{[N \times N_T \times N_R] \times N} \end{bmatrix} \end{aligned} \quad (6.42)$$

where sub-matrices represent the interaction between components of dipole moments due to all transceiver pairs at l^{th} frequency step. For example, $[A_{l,xx}]_{[N \times N_T \times N_R] \times N}$ includes the interaction between x -components of the dipole moments for all transceiver pairs at l^{th} frequency step. Finally, for a wideband imaging application, the resulting matrix equation to be solved can be written as

$$\begin{bmatrix} [A_{xx}]_{[N \times N_T \times N_R \times N_F] \times N} & [A_{xy}]_{[N \times N_T \times N_R \times N_F] \times N} & [A_{xz}]_{[N \times N_T \times N_R \times N_F] \times N} \\ [A_{yx}]_{[N \times N_T \times N_R \times N_F] \times N} & [A_{yy}]_{[N \times N_T \times N_R \times N_F] \times N} & [A_{yz}]_{[N \times N_T \times N_R \times N_F] \times N} \\ [A_{zx}]_{[N \times N_T \times N_R \times N_F] \times N} & [A_{zy}]_{[N \times N_T \times N_R \times N_F] \times N} & [A_{zz}]_{[N \times N_T \times N_R \times N_F] \times N} \end{bmatrix} \begin{bmatrix} [\alpha_{x,1}] \\ \vdots \\ [\alpha_{x,N}] \\ [\alpha_{y,1}] \\ \vdots \\ [\alpha_{y,N}] \\ [\alpha_{z,1}] \\ \vdots \\ [\alpha_{z,N}] \end{bmatrix} \\
= \begin{bmatrix} [E_{x,rec}] \\ [E_{y,rec}] \\ [E_{z,rec}] \end{bmatrix}$$

where the unknown is the polarizability α belonging to each component of dipole moments. In a more compact form, (6.43) can be written as

$$[A]_{[(3N \times N_T \times N_R \times N_F) \times 3N]} [\alpha]_{[3N \times 1]} = [E_{rec}]_{[(3N \times N_T \times N_R \times N_F) \times 1]}. \quad (6.44)$$

After solving (6.44), the relation between polarizability and relative dielectric constant distribution of the continuous medium can be established by using one of the CM, ILDR, VIEF, and CMRR relations.

It must be noted that operations required to perform one matrix-vector product to iteratively solve (6.44) is $N_T \times N_R \times N_F \times 9N^2$, which is much larger than the simple approach considered in previous sections and requires much more storage and computation time, therefore, application of an FMM-based method becomes inevitable to make the solution efficient.

6.6 Application of FMM in DDA

Provided that $|\mathbf{x}| < |\mathbf{R}|$, we have

$$\frac{e^{ik|\mathbf{R}+\mathbf{x}|}}{4\pi|\mathbf{R}+\mathbf{x}|} = \oint e^{ik\hat{\mathbf{k}} \cdot \hat{\mathbf{x}}} T_N(k, \mathbf{k}, \mathbf{R}) d^2\mathbf{k} \quad (6.45)$$

where

$$T_N(k, \mathbf{k}, \mathbf{R}) = \frac{ik}{(4\pi)^2} \sum_{l=0}^N i^l (2l+1) h_l^{(1)}(k|\mathbf{R}|) P_l(\mathbf{k} \cdot \hat{\mathbf{R}}). \quad (6.46)$$

Let $\mathbf{r}_{ij} = \mathbf{r}_{i\lambda} + \mathbf{r}_{\lambda\lambda'} + \mathbf{r}_{\lambda'j}$ and $\mathbf{x} = \mathbf{r}_{i\lambda} + \mathbf{r}_{\lambda'j}$, where $\mathbf{r}_{i\lambda}$ is aggregation vector, $\mathbf{r}_{\lambda\lambda'}$ is translation vector, and $\mathbf{r}_{\lambda'j}$ is disaggregation vector. Substituting (6.45) and (6.46) into (6.20) yields

$$\mathbf{p}_j = \alpha_j \mathbf{E}^{\text{inc}}(\mathbf{r}_j) - \frac{\alpha_j k_0^3}{4\pi\epsilon_0} \sum_{i=1}^N \oint_{i \neq j} T_N(k, \mathbf{k}, \mathbf{r}_{\lambda\lambda'}) \left[\bar{\mathbf{I}} + \frac{\nabla\nabla}{k_0^2} \right] e^{i\mathbf{k} \cdot \mathbf{x}} \mathbf{p}_i d^2\mathbf{k},$$

which can be rewritten as

$$\mathbf{p}_j = \alpha_j \mathbf{E}^{\text{inc}}(\mathbf{r}_j) - \frac{\alpha_j k_0^3}{4\pi\epsilon_0} \sum_{i=1}^N \oint_{i \neq j} e^{i\mathbf{k} \cdot \mathbf{r}_{\lambda'j}} T_N(k, \mathbf{k}, \mathbf{r}_{\lambda\lambda'}) e^{i\mathbf{k} \cdot \mathbf{r}_{i\lambda}} [\bar{\mathbf{I}} - \mathbf{k}\mathbf{k}] \mathbf{p}_i d^2\mathbf{k}. \quad (6.47)$$

Note that translation vector $\mathbf{r}_{\lambda\lambda'}$ is what determines the desired accuracy of the FMM formulation. Therefore, for any dipole \mathbf{p}_j , we can denote all other dipoles that do not satisfy $|\mathbf{x}| < |\mathbf{R}|$ condition as neighboring dipoles. The interaction between \mathbf{p}_j and these dipoles should be calculated directly in order to keep the accuracy at the desired level. Rest of the dipoles can be labeled as far dipoles and the interaction between \mathbf{p}_j and these dipoles can be calculated by the FMM formulation. In this way, (6.47) becomes

$$\begin{aligned} \mathbf{p}_j = & \alpha_j \mathbf{E}^{\text{inc}}(\mathbf{r}_j) - \frac{\alpha_j k_0^3}{4\pi\epsilon_0} \sum_{\substack{i \in \mathbb{N}_j \\ i \neq j}}^N \left[\bar{\mathbf{I}} + \frac{\nabla\nabla}{k_0^2} \right] \frac{e^{ik_0 r_{ij}}}{r_{ij}} \mathbf{p}_i \\ & - \frac{\alpha_j k_0^3}{4\pi\epsilon_0} \oint e^{i\mathbf{k} \cdot \mathbf{r}_{\lambda'j}} T_N(k, \mathbf{k}, \mathbf{r}_{\lambda\lambda'}) \sum_{i \notin \mathbb{N}_j}^N \{ e^{i\mathbf{k} \cdot \mathbf{r}_{i\lambda}} [\bar{\mathbf{I}} - \mathbf{k}\mathbf{k}] \cdot \mathbf{m}_i \} d^2\mathbf{k} \end{aligned}$$

where \mathbb{N}_j involves set of indices belonging to the neighbouring dipoles. Similar procedure can also be followed for magnetic dipoles, which yields

$$\mathbf{m}_j = \beta_j \mathbf{H}^{\text{inc}}(\mathbf{r}_j) - \frac{\beta_j k_0^3}{4\pi\mu_0} \sum_{\substack{i \in \mathbb{N}_j \\ i \neq j}}^N \left[\bar{\mathbf{I}} + \frac{\nabla\nabla}{k_0^2} \right] \frac{e^{ik_0 r_{ij}}}{r_{ij}} \mathbf{m}_i$$

$$- \frac{\beta_j k_0^3}{2} \oint\!\!\!\oint e^{i\mathbf{k} \cdot \mathbf{r}_{\lambda'j}} T_N(k, \hat{\mathbf{k}}, \mathbf{r}_{\lambda\lambda'}) \sum_{i \notin \mathbb{N}_j}^N \{e^{i\mathbf{k} \cdot \mathbf{r}_{i\lambda}} [\bar{\mathbf{I}} - \mathbf{k}\mathbf{k}] \cdot \mathbf{m}_i\} d^2\mathbf{k}.$$

The above equations for \mathbf{p}_j and \mathbf{m}_j rely on arranging the dipoles into groups. The effect of all far- dipoles on j^{th} dipole can be calculated by using the summed effect of all other groups on the group that j^{th} dipole belongs to, whereas the effect of the neighboring dipoles can be evaluated directly. Thus, the FMM formulation reduces the memory usage, since only the interactions between the neighboring dipoles are calculated and stored. Furthermore, group-by-group calculation for the effect of the far dipoles provides significant reduction in the operation count [117].

6.6.1 Grouping

Fig. 6.4 depicts the grouping scenario, where the dipoles on the target are grouped into cubical boxes. The scenario includes a source group (golden) and corresponding neighbouring (white) and far (grey) groups along all directions. Each box consists of 8 dipoles, which are represented by dielectric spheres of radius $0.5a$. The adjacent boxes, including diagonal ones, are designated as neighboring boxes and they need direct evaluation, while FMM can be applied for the rest. This arrangement is referred to as “one-box-buffer scheme” in the literature and nearest translation is performed along twice the edge length of the box [88]. In this scenario, distance between the center of the spheres is a and edge length of the boxes is $2a$. As shown in Fig. 6.5, the aggregation and disaggregation vectors are denoted by \mathbf{v}_1 and \mathbf{v}_2 , respectively, i.e., $\mathbf{v} = \mathbf{v}_1 + \mathbf{v}_2$, while translation vector is represented by \mathbf{w} . All vectors are placed between the centers of the spheres.

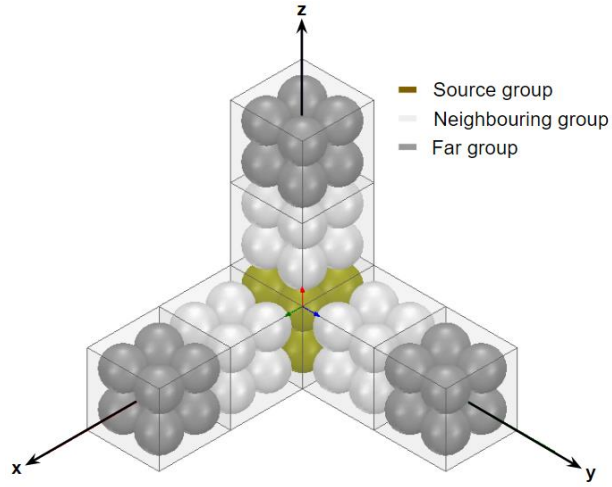


Figure 6.4. Grouping scenario for DDA.

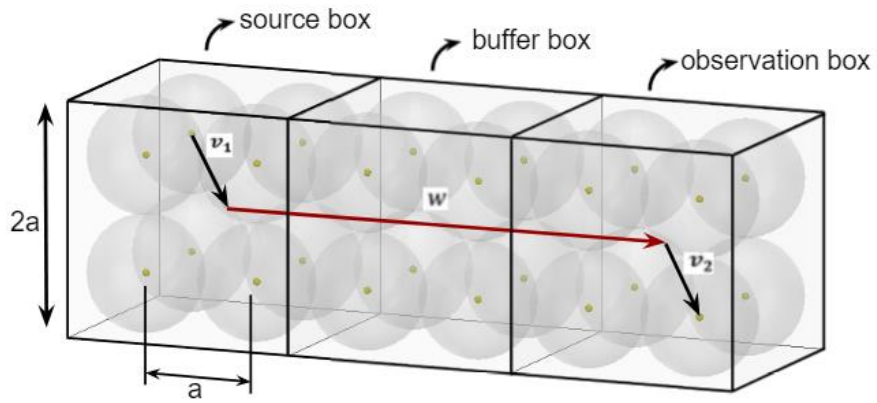


Figure 6.5. One-box-buffer scheme, including source, buffer, and observation boxes.

6.6.2 Numerical Examples

i) Image Quality Comparison:

The scenario of scattering from concentric cylinders, which is investigated in Section 5, is repeated in order to investigate how multiple reflections contribute to the quality of the reconstructed images. The problem is implemented using the discrete model given by (6.44) and resulting linear system is solved by C-SALSA-2

with the minimization of total variation of the unknown as regularization function and application of FMM.

Reflectivity values of the cylinders, which were respectively selected as 1, 0.6, 0.2 before, are replaced by relative dielectric constants of 10, 6, 2 so that the reconstructed images will share the same colour scaling. Vertically-polarized (oriented in z -direction) Hertzian dipoles are used as transmitting and receiving antennas. The cylinders are placed along y -direction between $y = 53$ cm and $y = 57$ cm planes and discretized by dielectric spheres (dipoles) of radius 5 mm ($1/6 \lambda_c, f_c = 10$ GHz), giving 6400 spheres in total. Classius-Mossotti relation is used for calculating the polarizabilities.

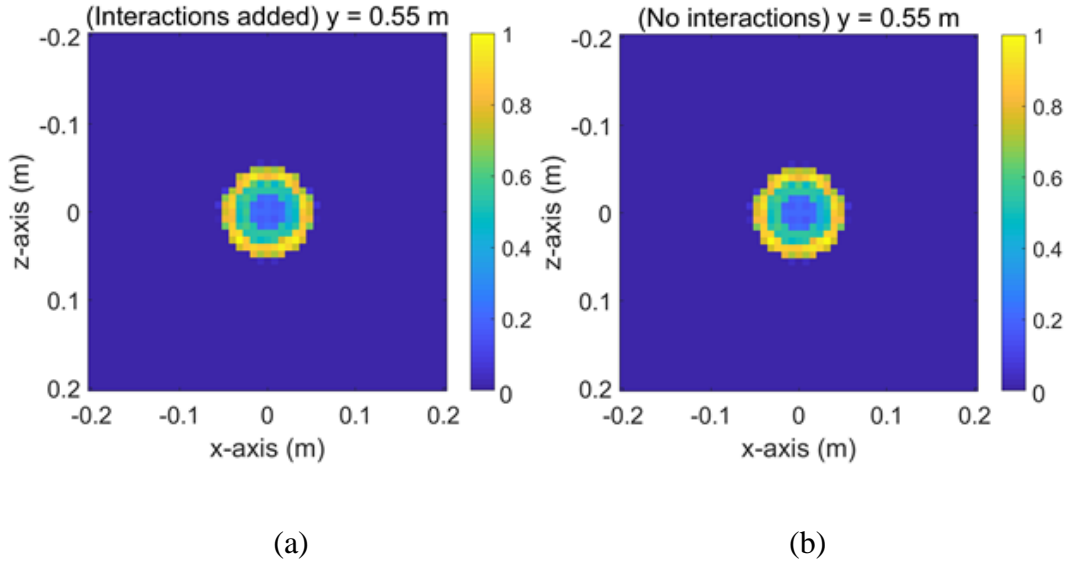


Figure 6.6. Normalized reconstructed images at $y = 55$ cm when (a) multiple reflections are included and (b) multiple reflections are ignored in the solution of the problem.

Fig. 6.6(a) shows the normalized reconstruction belonging to $y = 55$ cm slice of the cylinders, when the problem is solved by DDA approach. Fig. 6.6(b) gives the normalized reconstruction obtained in Section 5.4 to visibly compare the two results. It can be seen that quality of the reconstruction does not improve visibly when multiple reflections are added in the solution. To validate this result, the

reconstruction quality is also evaluated by PSNR. It is calculated as 36.42 dB for DDA solution, whereas it was obtained as 36.23 dB before, which supports our observations.

ii) Polarimetric Imaging

Polarization of an electromagnetic wave is defined by the curve that is traced by tip of the wave vector, e.g., vertical (up-down), horizontal (left-right), circular (clockwise or counter clockwise), etc. Polarimetric imaging is based on collecting data regarding the imaged scene using different combinations of transmitted and received wave polarizations.

Antenna array of a radar system can be designed to transmit and receive waves with different polarization pairs. Typically, a single polarization radar system transmits and receives waves with the same direction, yielding horizontal-horizontal (HH) or vertical-vertical (VV) imaging. On the other hand, a dual polarization radar system can transmit a wave in one direction but receive in two directions, providing either HH and HV or VH and VV imaging.

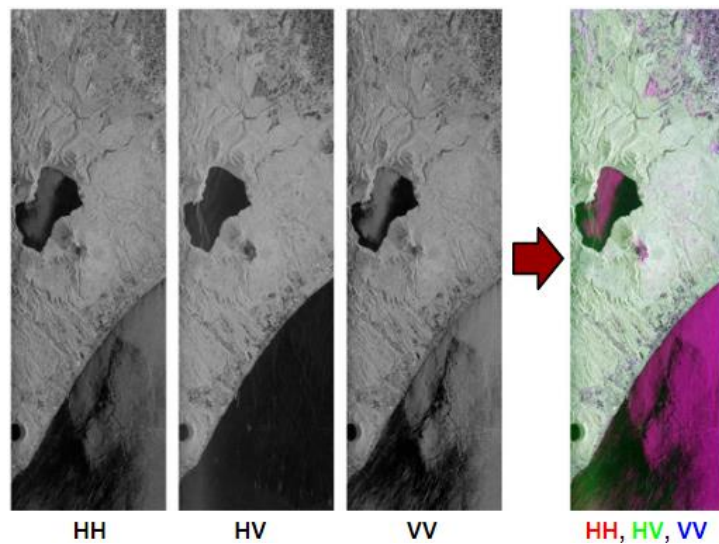


Figure 6.7. HH, HV and VH polarimetric images and RGB colour composite image of Tomakomai, Japan, acquired by PALSAR using H/V polarization on August 19, 2006.

Polarization diversity increases radar sensitivity, hence, detailed information can be collected about the imaged target such as structure, orientation, surface properties. For example, buildings, which are linearly-oriented, tend to reflect waves with the same linear direction, while tree leaves and branches, which are randomly-oriented, change the polarization of the received waves since they bounce multiple times on them. Fig. 6.7 shows radar images obtained with different polarization pairs.

Solving an imaging problem with DDA allows us to utilize polarization of the antennas while solving the problem, hence, polarimetric images of the target can be obtained. For demonstration, scattering from a homogeneous hourglass-shaped target ($\epsilon_r = 2.88$), which is composed of horizontal, vertical and diagonal parts, is considered. Normalized actual image of the target is given in Fig. 6.8 and it is discretized by dielectric spheres (dipoles) of radius 5 mm ($1/6 \lambda_c, f_c = 10$ GHz), yielding 3460 spheres overall. The target is placed at 55 cm away from the center of the MIMO array of Hertzian dipoles and imaged with HH, VV and VH polarization pairs. The problem is modeled by using (6.44) and solved by C-SALSA-2 algorithm with the application of FMM.

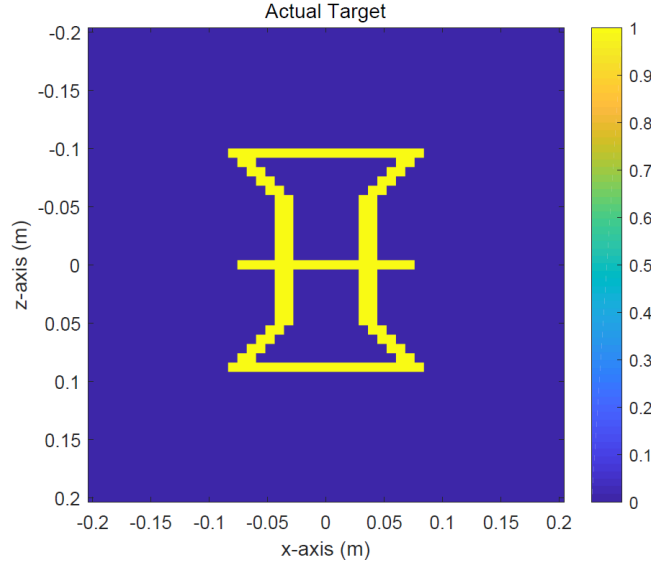


Figure 6.8. Normalized actual image of hourglass-shaped target.

Fig. 6.9(a)-(c) give color-assigned reconstruction images belonging to all polarization combinations, i.e. HH in green color scale, VV in red color scale, and VH in blue color scale. The results show that horizontally polarized fields are mostly scattered by the horizontal parts of the target, whereas vertically polarized fields are mostly scattered by the vertical parts of the target. On the other hand, diagonal parts are more visible with VH-polarization. Fig. 6.9(d) depicts the resulting colour-composite image, which is the superposition of RGB values of the color-assigned images. As can be seen, it exhibits a different color for different parts of the target with different orientation.

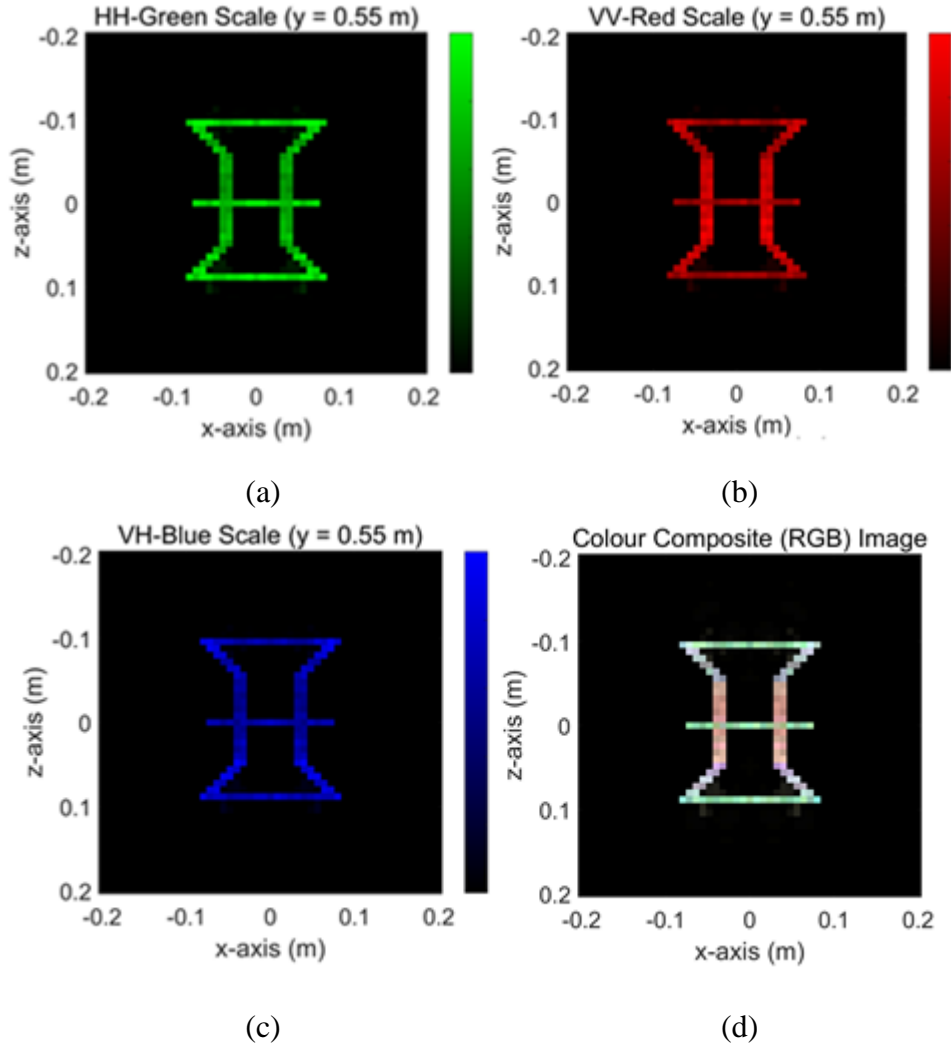


Figure 6.9. Color-assigned images for (a) HH-polarization, (b) VV-polarization, (c) HV-polarization. (d) Resulting colour-composite image of the target.

iii) Additional Analysis

The computational efficiency that FMM formulation provides for DDA solution is also investigated. For this purpose, we considered a scattering from a lossless dielectric cube of edge length 0.08 m. The cube is placed at $y = 55$ cm and illuminated by the MIMO array of Hertzian dipoles. Fig. 6.10 sketches target, whose outer part has a relative dielectric constant of 2.88, while inner part has a relative dielectric constant of 1.72. Initially, the target is replaced by an array of dielectric spheres of radius 4 mm, giving 1331 spheres in total. The problem is modeled using

(6.44) and solved by C-SALSA-2 algorithm. The reconstructed images belonging to the cross sections $y = 51$ cm, $y = 55$ cm, and $y = 59$ cm are given in Fig. 6.11, where the color scale shows the normalized magnitude of the reflectivity distribution of the target on the corresponding cross sectional cut.

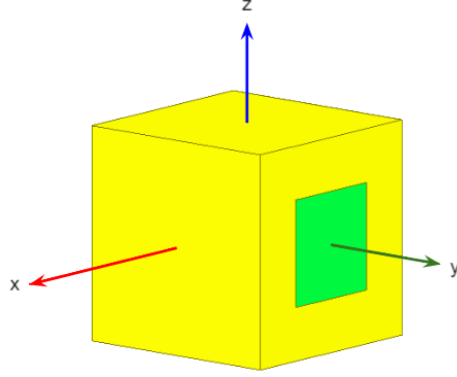


Figure 6.10. Lossless dielectric cube.

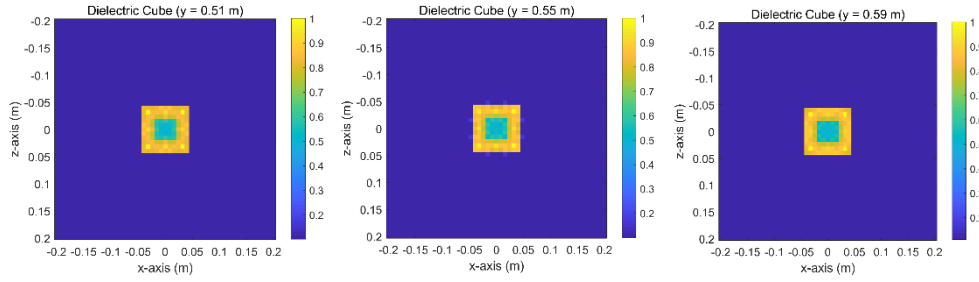


Figure 6.11. Normalized images reconstructed with the application of FMM at (a) $y = 51$ cm, (b) $y = 55$ cm, and (c) $y = 59$ cm.

Then, the same problem is repeatedly solved, while number of dipoles (represented by dielectric spheres) is increased gradually. Note that each dipole moment has three components, therefore, the number of unknowns is three times the number of dipoles. CPU time and memory requirement per matrix-vector product as a function of number of dipoles are plotted in 6.12. As expected, the graphs show that complexities of CPU time and memory requirement are obtained proportional to $O(N^{1.5})$ using FMM, whereas they are obtained proportional to $O(N^2)$ using direct matrix-vector product. FMM outperforms the direct matrix-vector product above the crossover

point, which is around 10000 dipoles. Note that this crossover point might vary with respect to the structure of the target, size of the dielectric spheres, and truncation order. Although the crossover point is reached after longer runtime than the previous approach takes, DDA yields an efficient solution, which is practically more feasible. That's because efficiency now depends on number of dipoles (represented by dielectric spheres), instead of number of antennas. Note that Fig. 6.12(b) plots the average memory usage that is monitored on the task manager during runtime.

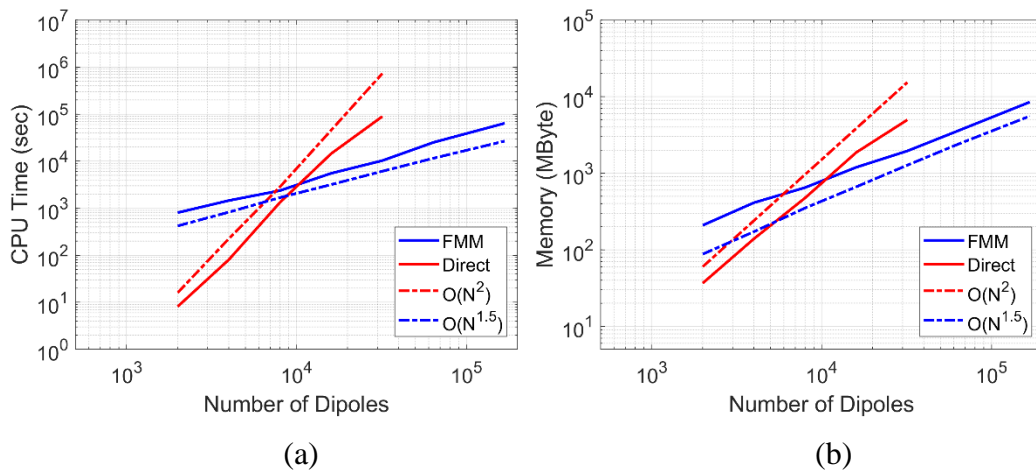


Figure 6.12. (a) CPU time and (b) memory requirement as a function of the number of unknowns.

CHAPTER 7

CONCLUSION

In this thesis, we present an efficient method for sparse solution to UWB near-field imaging problems, where the targets are assumed to be stationary. A plus-shaped MIMO radar configuration is utilized to implement the corresponding forward problem, where the imaged space is discretized by point scatterers on a predefined grid and received signals are defined using Born approximation. Due to this approximation, it is assumed that the point scatterers directly reflect the incident signals and multiple reflections between them are ignored. After discretization, the imaging problem is turned into a matrix equation to be solved, where entries of the observation matrix are products of two 3D Green's functions. As major contribution, we use this structure as key point to apply FMM formulation for calculating matrix-vector multiplications within iterative solvers. FMM enables us to calculate the multiplications without explicitly forming the observation matrix, hence, significant improvement at memory usage is obtained. Besides, grouping approach decreases the computation time significantly. It is mathematically shown that large scale imaging problems can be solved more efficiently, when FMM is applied in the solver.

Here, it must be noted that we define the problem using a known grid, although various gridless approaches are also studied in the literature. That's because number of scatterers and their location become an optimization parameter in the gridless case. Despite the fact that FMM can handle such a case, forward problem with a matrix that is not fixed cannot be solved using standard techniques.

We demonstrate applicability of the proposed FMM-based approach to various sparsity-inducing algorithms, while seeking sparse solution to imaging problems. For this purpose, we first solve several imaging scenarios with point scatterers by

using greedy pursuit algorithms (such as OMP), which are based on minimization of ℓ_0 “norm”. Afterwards, we convert the imaging problems of 2-D/3-D targets into convex optimization problem by using minimization of l_1 -norm or minimization of TV of the unknown depending on the physical properties of the target and solve them by augmented Lagrangian based algorithms (such as ADMM and C-SALSA). All these algorithms include minimization problems within their structure and we solve them in an inner iteration, where matrix-vector multiplications are calculated by FMM. We show that FMM-based solution computationally outperforms classic direct solvers, as the number of antennas exceed a specific point. Additionally, we compare reconstructed images to those obtained by direct solvers. We demonstrate that sparsity-based algorithms are able to yield more focused images (with higher PSNRs), even under low input SNR levels.

Then, we address the near-field imaging problem as an electromagnetic scattering problem and solve it by DDA approach, which replaces the solid target by an array of dipoles and includes multiple reflections in its formulation. By the use of DDA, we aim to observe possible changes at the quality of the reconstructed images, when multiple reflections are considered in the problem definition. We demonstrate that they do not improve the quality of reconstructions (visibly or quantitatively) for continuous penetrable targets. But, we think that they might be significantly effective, when the target of interest has multiple conductive parts, since the amplitude of multiple reflections might be unignorable. We leave this part as a research field that can be studied in the future.

When the problem is defined with the use of DDA, complexity of the solution depends on the number of dipoles that are used for discretizing the imaged target. As the target size, thereby the number of dipoles, increases, standard solvers become inefficient. Therefore, we finally apply FMM in DDA formulation so that the reconstruction is very efficient in terms of CPU time and memory requirement. Because the efficiency is now based on the number of dipoles instead of number of antenna elements, this new solution is practically more feasible than the previous approach.

REFERENCES

- [1] X. Zhuge and A. G. Yarovoy, "A sparse aperture MIMO-SAR based UWB imaging system for concealed weapon detection", *IEEE Trans. Geosci. Remote Sens.*, vol. 49, no. 1, pp. 509-518, Jan. 2011.
- [2] A. G. Yarovoy, T. G. Savelyev, P. J. Aubry, P. E. Lys and L. P. Ligthart, "UWB array-based sensor for near-field imaging", *IEEE Trans. Microw. Theory Tech.*, vol. 55, no. 6, pp. 1288-1295, Jun. 2007.
- [3] A. Beeri and R. Daisy, "High-resolution through-wall imaging," *Proc. SPIE*, vol. 6201, pp. 62010J, 2006.
- [4] M. Klemm, J. A. Leendertz, D. Gibbins, I. J. Craddock, A. Preece and R. Benjamin, "Microwave radar-based differential breast cancer imaging: Imaging in homogeneous breast phantoms and low contrast scenarios", *IEEE Trans. Antennas Propag.*, vol. 58, no. 7, pp. 2337-2344, Jul. 2010.
- [5] X. Zhuge, "Short-range ultra-wideband imaging with multiple-input multiple-output arrays," Ph.D. dissertation, Delft University of Technology, 2010.
- [6] B. Yang et al., "UWB MIMO antenna array topology design using PSO for through dress near-field imaging," in *Proc. German Microwave Conf.*, 2008, pp. 463–466.
- [7] T. Savelyev et al., "Comparison of UWB SAR and MIMO-based short range imaging radars," in *Proc. European Radar Conf.*, 2009, pp. 109– 112.
- [8] Y. Liu et al., "Reducing the number of elements in a linear antenna array by the matrix pencil method," *IEEE Trans. Antennas Propag.*, pp. 2955–2962, 2008.
- [9] K. Tan et al., "A novel two-dimensional sparse MIMO array topology for UWB short-range imaging," *IEEE Antennas and Wireless Propagation Letters*, pp. 702–705, 2016.

- [10] K. Tan et al., “On Sparse MIMO Planar Array Topology Optimization for UWB Near-Field High-Resolution Imaging,” *IEEE Trans. Antennas Propag.*, vol. 65, no. 2, pp. 989-994, Feb. 2017.
- [11] M. B. Kocamis and F. S. Oktem, “Optimal design of sparse MIMO arrays for near-field ultra-wideband imaging,” 2017 25th European Signal Processing Conference (EUSIPCO), Kos, 2017, pp. 1952-1956.
- [12] X. Zhuge and A. G. Yarovoy, “Three-Dimensional Near-Field MIMO Array Imaging Using Range Migration Techniques,” *IEEE Trans. on Image Process.*, vol. 21, no. 6, pp. 3026-3033, June 2012.
- [13] T. Savelyev et al., “Comparison of UWB SAR and MIMO-based short-range imaging radars,” in *Proc. European Radar Conf.*, 2009, pp. 109 – 112.
- [14] B. Sharif and F. Kamalabadi, “Optimal sensor array configuration in remote image formation,” *IEEE Trans. on Image Process.*, pp. 155–166, 2008.
- [15] F. Anderson, W. Christensen, L. Fullerton, and B. Kortegaard, “Ultrawideband beamforming in sparse arrays,” *Proc. Inst. Elect. Eng.—H*, vol. 138, no. 4, pp. 342–346, Aug. 1991.
- [16] J. L. Schwartz and B. D. Steinberg, “Ultrasparse, ultrawideband arrays,” *IEEE Trans. Ultrason., Ferroelectr., Freq. Control*, vol. 45, no. 2, pp. 376–393, Mar. 1998.
- [17] X. Zhuge, T. G. Savelyev, A. G. Yarovoy, L. P. Ligthart, J. Matuzas, and B. Levitas, “Human body imaging by microwave UWB radar,” in *Proc. EuRAD*, Oct. 2008, pp. 148–151.
- [18] J. Hadamard: *Lectures on the Cauchy problems in linear partial differential equations*. Yale Univ Press, New Haven, 1923.
- [19] M. Heili, T. Lhivaara, E. Laitinen, T. Mantere, J. Merikoski, S. Pohjolainen, K. Raivio, R. Silvennoinen, A. Suutala, T. Tarvainen, T. Tiihonen, J. Tuomela, E. Turunen, M. Vauhkonen, and S. Pohjolainen. 2016. “Mathematical Modelling” (1st. ed.). Springer Publishing Company, Incorporated.

- [20] S. Noschese and L. Reichel, “A modified truncated singular value decomposition method for discrete ill-posed problems,” *Numerical Linear Algebra with Applications*, vol. 21, no. 6, pp. 813–822, 2014.
- [21] C. Brezinski, G. Rodriguez, and S. Seatzu, “Error estimates for linear systems with applications to regularization,” *Numer. Algorithms*, 49 (2008), pp. 85–104.
- [22] C. Brezinski, G. Rodriguez, and S. Seatzu, “Error estimates for the regularization of least squares problems,” *Numer. Algorithms*, 51 (2009), pp. 61–76.
- [23] H. W. Engl, M. Hanke, and A. Neubauer, “Regularization of Inverse Problems,” Kluwer, Dordrecht, 1996.
- [24] P. C. Hansen, “Rank-Deficient and Discrete Ill-Posed Problems,” SIAM, Philadelphia, 1998.
- [25] B. W. Rust, “Truncating the Singular Value Decomposition for Ill-Posed Problems,” Report NISTIR 6131, Mathematical and Computational Sciences Division, NIST, 1998.
- [26] Tikhonov, A. N.; V. Y. Arsenin (1977). “Solution of Ill-posed Problems,” Washington: Winston & Sons.
- [27] Tikhonov, Andrey Nikolayevich; Goncharsky, A.; Stepanov, V. V.; Yagola, Anatolij Grigorevic (30 June 1995). “Numerical Methods for the Solution of Ill-Posed Problems”. Netherlands: Springer Netherlands.
- [28] Tikhonov, Andrey Nikolaevich; Leonov, Aleksandr S.; Yagola, Anatolij Grigorevic (1998). London: Chapman & Hall.
- [29] Phillips, D. L. (1962). “A Technique for the Numerical Solution of Certain Integral Equations of the First Kind”. *Journal of the ACM*. **9**: 84–97.
- [30] Fuhry, M., Reichel, L. “A new Tikhonov regularization method,” *Numer Algor* **59**, 433–445 (2012).
- [31] C. Brezinski, M. Redivo-Zaglia, G. Rodriguez, and S. Seatzu, “Extrapolation techniques for ill-conditioned linear systems,” *Numer. Math.*, 81 (1998), pp. 1–29.

- [32] L. Reichel and Q. Ye, “Simple square smoothing regularization operators,” *Electron. Trans. Numer. Anal.*, 33 (2009), pp. 63–83.
- [33] J. H. Wilkinson, “The Algebraic Eigenvalue Problem”. Oxford University Press, Oxford, 1965.
- [34] J. A. Tropp and S. J. Wright, “Computational methods for sparse solution of linear inverse problems,” *Proc. IEEE*, vol. 98, no. 6, pp. 948–958, Jun. 2010.
- [35] S. S. Chen, D. L. Donoho, and M. A. Saunders, “Atomic decomposition by its basis pursuit,” *SIAM Rev.*, vol. 43, no. 1, pp. 129–159, 2001.
- [36] S. Gazzola and J. G. Nagy, “Generalized Arnoldi-Tikhonov method for sparse reconstruction,” *SIAM J. Sci. Comput.*, 36 (2014), pp. B225–B247.
- [37] G. Davis, S. Mallat, and M. Avellaneda, “Adaptive greedy approximations,” *J. Constr. Approx.*, vol. 13, pp. 57–98, 1997.
- [38] A. C. Gilbert, M. Muthukrishnan, and M. J. Strauss, “Approximation of functions over redundant dictionaries using coherence,” in *Proc. 14th Annu. ACM-SIAM Symp. Discrete Algorithms*, Jan. 2003.
- [39] D. L. Donoho, Y. Tsaig, I. Drori, and J.-L. Starck, “Sparse solution of underdetermined linear equations by stagewise Orthogonal Matching Pursuit,” *IEEE Trans. Inf. Theory*, vol. 58, no. 2, pp. 1094–1121, 2012.
- [40] H. E. Guven, A. Gungor, and M. Cetin, “An augmented lagrangian method for complex-valued compressed SAR imaging,” *IEEE Trans. Comput. Imag.*, vol. 2, no. 3, pp. 235–250, Sep. 2016.
- [41] M. Afonso, J. M. Bioucas-Dias, M. A. T. Figueiredo, “An augmented Lagrangian approach to the constrained optimization formulation of imaging inverse problems,” *IEEE Trans. Image Processing*, vol. 20, no. 3, pp. 681–695, Mar. 2011.
- [42] S. Wright, R. Nowak, and M. Figueiredo, “Sparse reconstruction by separable approximation,” *IEEE Trans. Signal Process.*, vol. 57, no. 7, pp. 2479–2493, Jul. 2009.

- [43] M. Afonso, J. M. Bioucas-Dias, and M. A. T. Figueiredo, "Fast image recovery using Variable Splitting and constrained optimization," *IEEE Trans. Image Processing*, vol. 10, no. 9, pp. 2345-2356, Sep. 2010.
- [44] M. Figueiredo, J. M. Bioucas-Dias, and M. Afonso, "Fast frame-based image deconvolution using variable splitting and constrained optimization," in *Proc. IEEE Workshop Statist. Signal Process.*, Cardiff, U.K., 2009, pp. 109-112.
- [45] D. Wipf and B. Rao, "Sparse Bayesian learning for basis selection," *IEEE Trans. Signal Process.*, vol. 52, no. 8, pp. 2153-2164, Aug. 2004.
- [46] P. Schniter, L. C. Potter, and J. Ziniel, "Fast Bayesian matching pursuit: Model uncertainty and parameter estimation for sparse linear models," *IEEE Trans. Signal Process.* 2008
- [47] R. Chartrand, "Exact reconstruction of sparse signals via nonconvex optimization," *IEEE Signal Process. Lett.*, vol. 14, no. 10, pp. 707-710, Oct. 2007.
- [48] A. J. Miller, "Subset Selection in Regression". 2nd Ed. London, U.K.: Chapman and Hall, 2002
- [49] M. E. Yanik and M. Torlak, "Near-Field MIMO-SAR Millimeter-Wave Imaging with Sparsely Sampled Aperture Data," in *IEEE Access*, vol. 7, pp. 31801-31819, 2019.
- [50] J. R. Phillips and J. K. White, "A precorrected-FFT method for electrostatic analysis of complicated 3D structures," *IEEE Trans. Comput. Aided Des.*, 16 (10): 1059-1072, 1997.
- [51] C. H. Chan, C. M. Lin, L. Tsang, and Y. F. Leung, "A sparse - matrix/canonical grid method for analysing microstrip structures," *IEICE Trans. Electron.*, E80C: 1354-1359, 1997.
- [52] Jian-Ming Jin, "Theory and Computation of Electromagnetic Fields". 1st edition. John Wiley & Sons, 2010.

- [53] N. Engheta, W. D. Murphy, V. Rokhlin, and M. S. Vassiliou, "The fast multipole method (FMM) for electromagnetic scattering problems," *IEEE Trans. Antennas Propagat.*, vol. 40, no. 6, pp. 634–641, June 1992.
- [54] J. R. Coifman, V. Rokhlin, and S. Wandzura, "The fast multipole method for the wave equation: a pedestrian prescription," *IEEE Ant. Propag. Mag.*, vol. 35, no. 3, pp. 7–12, June 1993.
- [55] C.-C. Lu and W. C. Chew, "Multilevel fast multipole algorithm for electromagnetic scattering by large complex objects," *IEEE Trans. Antennas Propagat.*, vol. 45, no. 10, pp. 1488–1493, Oct. 1997.
- [56] J. M. Song, C.-C. Lu, W. C. Chew, and S. W. Lee, "Fast Illinois solver code (FISC)," *IEEE Ant. Propag. Mag.*, vol. 40, no. 3, pp. 27–34, Oct. 1998.
- [57] W. C. Chew, J.-M. Jin, E. Michielssen, and J. M. Song, eds., "Fast and Efficient Algorithms in Computational Electromagnetics". Boston-London: Artech House Publishers, 2001.
- [58] The Fast Multipole Method for Electromagnetic Field Computation in Numerical and Physical Hybrid Systems, Ruth Vazquez Sabariego, PhD Thesis, October 2004.
- [59] O. T. Von Ramm, S. W. Smith, and F. L. Thurstone, "Grey scale imaging with complex TGC and transducer arrays," in *Proc. Soc. Photo-Opt. Inst. Eng.*, Med. IV, 1975, vol. 70, pp. 266-270.
- [60] C. R. Cooley, B. S. Robinson, , "Synthetic Focus Imaging Using Partial Datasets," in *Proc. Ultrasonic Symposium*, 1994, vol. 3, pp. 1539-1542.
- [61] R. T. Hoxtor and S. A. Kassam, "Synthetic aperture ultrasonic imaging system using a minimum redundancy phased array," U.S. Patent 5 278 757, Jan. 11, 1994.
- [62] G. R. Lookwood, P.C. Li, M. O'Donnell, and F. S. Foster, "Optimizing the Radiation Pattern of Sparse Periodic Linear Arrays," *IEEE Trans. Ultrason., Ferroelectr. Freq. Control*, vol. 43, pp. 7-14, Jan. 1996.

- [63] S. S. Ahmed, A. Schiessl, and L.-P. Schmidt, "Near field mm-wave imaging with multistatic sparse 2D-arrays," in Proc. 6th Eur. Radar Conf. Rome, Italy, 2009, pp. 180-183.
- [64] Yang, B.; Yarovoy, A.; Aubry, P.; Zhuge, X., "Experimental verification of 2D UWB MIMO antenna array for near-field imaging radar," in Proc. 39th Euro. Micro. Conf., Rome, Italy, 2009, pp. 97-100.
- [65] X. Zhuge and A.G. Yarovoy, "Study on two-dimensional sparse MIMO UWB arrays for high resolution near-field imaging," IEEE Trans. Antennas. Propag., vol. 60, no. 9, pp. 4173-4182, Sep. 2012.
- [66] E. Fishler, A. Haimovich, R. Blum, D. Chizhik, L. Cimini and R. Valenzuela, "MIMO radar: an idea whose time has come," Proceedings of the 2004 IEEE Radar Conference (IEEE Cat. No.04CH37509), 2004, pp. 71-78.
- [67] T. Aittomaki and V. Koivunen, "Low-complexity method for transmit beamforming in MIMO radars," in Proc. 2007 IEEE Int. Conf. Acoustics, Speech, and Signal Processing (ICASSP), Honolulu, USA, Apr. 2007, pp. II 305-308.
- [68] I. Bekkerman and J. Tabrikian, "Target detection and localization using MIMO radars and sonars," IEEE Trans. Signal Process., vol. 54, pp. 3873–3883, Oct. 2006.
- [69] D. W. Bliss, and K. W. Forsythe, "Multiple-input multiple-output (MIMO) radar and imaging: Degrees of freedom and resolution," IEEE Trans. Ultrason., Ferroelectr. Freq. Control, vol. 43, pp. 7-14, Jan. 1996.
- [70] K. W. Forsythe, D. W. Bliss, and G. S. Fawcett, "Multiple-input multiple-output (MIMO) radar: Performance issues," in Proc. 38th Asilomar Conf. Signals, Systems and Computers, Pacific Grove, CA, Nov. 2004, vol. 1, pp. 310–315.
- [71] J. Li and P. Stoica, "MIMO radar with collocated antennas: Review of some recent work," IEEE Signal Process. Mag., vol. 24(5), pp. 106–114, Sep. 2007.

- [72] L. Xu and J. Li, "Iterative generalized likelihood ratio test for MIMO radar," *IEEE Trans. Signal Process.*, vol. 55(6), pp. 2375–2385, Jun. 2007.
- [73] D. W. Bliss and K. W. Forsythe, "MIMO Radar Medical Imaging: Self-Interference Mitigation for Breast Tumor Detection," 2006 Fortieth Asilomar Conference on Signals, Systems and Computers, 2006, pp. 1558-1562.
- [74] Y. Chen, I. J. Craddock, P. Kosmas, M. Ghavami and P. Rapajic, "Multiple-Input Multiple-Output Radar for Lesion Classification in Ultrawideband Breast Imaging," in *IEEE Journal of Selected Topics in Signal Processing*, vol. 4, no. 1, pp. 187-201, Feb. 2010.
- [75] J. Kim, A. Ossowska and W. Wiesbeck, "Investigation of MIMO SAR for interferometry," 2007 European Radar Conference, 2007, pp. 51-54.
- [76] I. Stojanovic and W. C. Karl, "Imaging of Moving Targets with Multi-Static SAR Using an Overcomplete Dictionary," in *IEEE Journal of Selected Topics in Signal Processing*, vol. 4, no. 1, pp. 164-176, Feb. 2010.
- [77] B. Correll, "Efficient Spotlight SAR MIMO Linear Collection Configurations," in *IEEE Journal of Selected Topics in Signal Processing*, vol. 4, no. 1, pp. 33-39, Feb. 2010.
- [78] M. Lesturgie. "Some relevant applications of MIMO to radar," In 2011 Proceedings International Radar Symposium (IRS), pages 714-721, 2011.
- [79] A. Martinez-Vazquez and J. Fortuny-Guasch. "UWB MIMO radar arrays for small area surveillance applications," In The Second European Conference on Antennas and Propagation EuCAP 2007, pages 1-6, 2007.
- [80] S. Lutz, K. Baur, and T. Walter. "77 GHz lens-based multistatic MIMO radar with colocated antennas for automotive applications," In 2012 IEEE MTT-S International Microwave Symposium Digest (MTT), pages 1-3, 2012.
- [81] C. Fischer, A. Herschlein, M. Younis, and W. Wiesbeck. "Detection of antipersonnel mines by using the factorization method on multistatic ground-penetrating radar measurements," *IEEE Transactions on Geoscience and Remote Sensing*, 45(1):85-92, 2007.

- [82] A. Dzvonkovskaya, K. W. Gurgel, T. Pohlmann, T. Schlick, and J. Xu. "Simulation of tsunami signatures in ocean surface current maps measured by HF radar," In OCEANS 2009 - EUROPE, pages 1-6, May 2009.
- [83] X. P. Masbernat, M. G. Amin, F. Ahmad, and C. Ioana. "An MIMO-MTI approach for through-the-wall radar imaging applications," In 2010 International Waveform Diversity and Design Conference (WDD), pages 000188-000192.
- [84] E. Pancera, T. Zwick, and W. Wiesbeck. "Ultra wideband radar imaging: An approach to monitor the water accumulation in the human body," In 2010 IEEE International Conference on Wireless Information Technology and Systems (ICWITS), pages 1-4, 2010.
- [85] Gibson, W.C. (2015). "The Method of Moments in Electromagnetics" (2nd ed.). Chapman and Hall/CRC.
- [86] L. Greengard and V. Rokhlin, "A fast algorithm for particle simulations," J. Comput. Phys., vol. 73, pp. 325-348, 1987.
- [87] J. M. Song and W. C. Chew, "Error analysis for the truncation of multipole expansion of vector Green's functions," IEEE Microwave and Wireless Components Lett., 11 (2001), pp. 311–313.
- [88] M. Kalfa, Ö. Ergül and V. B. Ertürk, "Error Control of Multiple-Precision MLFMA," in IEEE Transactions on Antennas and Propagation, vol. 66, no. 10, pp. 5651-5656, Oct. 2018.
- [89] I. F. Gorodnitsky, J. S. George, and B. D. Rao, "Neuromagnetic source imaging with FOCUSS: A recursive weighted minimum norm algorithm," J. Electroencephalog. Clinical Neurophysiol., vol. 95, no. 4, pp. 231–251, Oct. 1995.
- [90] B. D. Jeffs, "Sparse inverse solution methods for signal and image processing applications," in Proc. ICASSP, vol. III, Seattle, WA, May 1998, pp. 1885–1888.

- [91] D. L. Duttweiler, "Proportionate normalized least-mean-squares adaptation in echo cancelers," *IEEE Trans. Speech Audio Process.*, vol. 8, no. 5, pp. 508–518, Sep. 2000.
- [92] B. Jeffs and M. Gunsay, "Restoration of blurred star field images by maximally sparse optimization," *IEEE Trans. Image Process.*, vol. 2, no. 2, pp. 202–211, Mar. 1993.
- [93] E. Crespo Marques, N. Maciel, L. Naviner, H. Cai and J. Yang, "A Review of Sparse Recovery Algorithms," in *IEEE Access*, vol. 7, pp. 1300-1322, 2019.
- [94] Mallat, S. G. and Z. Zhang, "Matching pursuits with time-frequency dictionaries. *Signal Processing*," *IEEE Transactions on* 41(12), 3397–3415. (1993, Dec)
- [95] Y. C. Pati, R. Rezaiifar, and P. S. Krishnaprasad, "Orthogonal matching pursuit: Recursive function approximation with applications to wavelet decomposition," in *Proc. 27th Asilomar Conf. Signals, Syst. Comput.*, vol. 1, Nov. 1993, pp. 40-44.
- [96] Mallat, S. G., G. Davis, and Z. Zhang (1994, July). "Adaptive time-frequency decompositions," *SPIE Journal of Optical Engineering* 33, 2183–2191.
- [97] Davis, G., S. G. Mallat, and M. Avellaneda (1997). "Greedy adaptive approximation".
- [98] D. L. Donoho, Y. Tsaig, I. Drori, and J.-L. Starck, "Sparse solution of underdetermined systems of linear equations by stagewise orthogonal matching pursuit," *IEEE Trans. Inf. Theory*, vol. 58, no. 2, pp. 1094–1121, Feb. 2012.
- [99] Needell, D. (2009), "Topics in Compressed Sensing". UC Davis: Department of Mathematics. arXiv ID:0905.4482.
- [100] K. V. Siddamal, S. P. Bhat, and V. S. Saroja, "A survey on compressive sensing," in *Proc. 2nd Int. Conf. Electron. Commun. Syst. (ICECS)*, Feb. 2015, pp. 639-643.

- [101] D. Needell and R. Vershynin, "Uniform uncertainty principle and signal recovery via regularized orthogonal matching pursuit," *Found. Comput. Math.*, vol. 9, no. 3, pp. 317-334, Jun. 2009.
- [102] D. Needell and J. A. Tropp, "CoSaMP: Iterative signal recovery from incomplete and inaccurate samples," California Inst. Technol., Pasadena, CA, USA, Tech. Rep. 2008-01, 2008.
- [103] W. Dai and O. Milenkovic, "Subspace pursuit for compressive sensing signal reconstruction," *IEEE Trans. Inf. Theory*, vol. 55, no. 5, pp. 2230-2249, May 2009.
- [104] D. Needell and J. A. Tropp, "CoSaMP: Iterative signal recovery from incomplete and inaccurate samples," California Inst. Technol., Pasadena, CA, USA, Tech. Rep. 2008-01, 2008.
- [105] S. S. Chen, D. L. Donoho, and M. A. Saunders, "Atomic decomposition by basis pursuit," *SIAM J. Sci. Comput.*, 20(1):33–61 (electronic), 1998.
- [106] S. Boyd, N. Parikh, E. Chu, B. Peleato, and J. Eckstein, "Distributed optimization and statistical learning via the alternating direction method of multipliers," *Foundations and Trends in Machine Learning*, 3(1):1–122, 2011.
- [107] S. Boyd and L. Vandenberghe, "Convex Optimization". Cambridge University Press, 2004.
- [108] R. T. Rockafellar, "Convex Analysis". Princeton University Press, 1970.
- [109] J. M. Bioucas-Dias and M. A. T. Figueiredo, "An iterative algorithm for linear inverse problems with compound regularizers," 2008 15th IEEE International Conference on Image Processing, 2008, pp. 685-688.
- [110] Y. Wang, J. Yang, W. Yin, and Y. Zhang, A, "New Alternating Minimization Algorithm for Total Variation Image Reconstruction," *SIAM J. Imag. Sci.*, vol. 1, no. 3, pp. 248-272, 2008.
- [111] O. Batu and M. Cetin, "Parameter Selection in sparsity driven SAR imaging," *IEEE Trans. Aerosp. Electron. Syst.* Vol. 47, no. 4, pp. 3040-3050, Oct. 2011.

- [112] G. H. Golub, M. Heath, and G. Wahba, "Generalized cross-validation as a method for choosing a good ridge parameter," *Technometrics*, vol. 21, no. 2, pp. 215-223, 1979.
- [113] Purcell, E. M. and C. R. Pennypacker, "Scattering and absorption of light by nonspherical dielectric grains," *The Astrophysical Journal*, Vol. 186, 705-714, Dec. 1973.
- [114] Draine, B. T., "The discrete-dipole approximation and its application to interstellar graphite grains," *The Astrophysical Journal*, Vol. 333, No. 2, 848-872, Oct. 1988.
- [115] Lumme, K. and J. Rahola, "Light scattering by porous dust particles in the discrete-dipole approximation," *The Astrophysical Journal*, Vol. 425, No. 2, 653-667, Apr. 1994.
- [116] Rahola, J., "Solution of dense systems of linear equations in the discrete-dipole approximation," *SIAM J. Sci. Comput.*, Vol. 17, No. 1, 78-89, Jan. 1996.
- [117] S. Koç & W.C. Chew (2001) "Multilevel Fast Multipole Algorithm for the Discrete Dipole Approximation, *Journal of Electromagnetic Waves and Applications*," 15:11, 1447-1468, Apr. 2012.
- [118] Jackson, J. D., "Classical Electrodynamics". 2nd edition, Chapter 9.14, John Wiley & Sons, Inc., New York, 1975.
- [119] Goedecke, G. H. and S. G. O'Brien, "Scattering by irregular inhomogeneous particles via the digitized Green's function algorithm," *Applied Optics*, Vol. 27, No. 12, 2431-2438, June 1988.
- [120] Hage, J. I. and J. M. Greenberg, "A model for the optical properties of porous grains," *The Astrophysical Journal*, Vol. 361, No. 1, 251-259, Sep. 1990.
- [121] Draine, B. T. and J. Goodman, "Beyond Clausius-Mosotti: Wave propagation on a polarizable point lattice and the discrete dipole approximation," *The Astrophysical Journal*, Vol. 405, No. 2, 685-697, Mar. 1993.

- [122] X.Zhuge, A. Yarovoy, T. Savelyev, and L. Ligthart, "Modified Kirchho_ migration for UWB MIMO array-based radar imaging," *IEEE Trans. Geosci. Remote Sens.*, vol. 48, pp. 2692–2703, 2010.
- [123] J. Lopez-Sanchez and J. Fortuny-Guasch, "3-D radar imaging using range migration techniques," *IEEE Trans. Antennas Propag.*, vol. 48, pp. 728–737, 2000.
- [124] J. Aliferis, T. Savelyev, M. J. Yedlin, J. Y. Dauvignac, A. Yarovoy, C. Pichot, and L. Ligthart, "Comparison of the di_raction stack and time-reversal imaging algorithms applied to short-range UWB scattering data," in *2007 IEEE International Conference on Ultra-Wideband*, Sept 2007, pp. 618–621.
- [125] P. M. Morse and H. Feshbach, "Method of Theoretical Physics". New York: McGraw-Hill, 1953.
- [126] M. Böhme and D. Potts, "A Fast Algorithm for filtering and wavelet decomposition on the sphere," *Trans. Numer. Anal*, vol. 16, pp. 70-93, 2002.
- [127] E. A. Miran, F. S. Oktem and S. Koc, "Sparse Reconstruction for Near-Field MIMO Radar Imaging Using Fast Multipole Method," in *IEEE Access*, vol. 9, pp. 151578-151589, 2021.
- [128] Bo Wahlberg, Stephen Boyd, Mariette Annergren, Yang Wang, "An ADMM Algorithm for a Class of Total Variation Regularized Estimation Problems," *IFAC Proceedings Volumes*, Volume 45, Issue 16, 2012, Pages 83-88.
- [129] N. Antipa, G. Kuo, R. Heckel, B. Mildenhall, E. Bostan, R. Ng, and L. Waller, "DiffuserCam: Lensless single-exposure 3D imaging," *Optica*, vol. 5, no. 1, pp. 1-9, 2018.
- [130] O. F. Kar and F. S. Oktem, "Compressive spectral imaging with diffractive lenses," *Opt. Lett.*, vol. 44, no. 18, pp. 4582-4585, 2019.
- [131] D. Bi, X. Li, X. Xie, Y. Xie, and Y. R. Zheng, "Compressive sensing operator design and optimization for wideband 3-D millimeter-wave imaging," *IEEE Trans. Microw. Theory Techn.*, early access, Aug. 9, 2021.

- [132] S. Li, G. Zhao, H. Sun, and M. Amin, "Compressive sensing imaging of 3-D object by a holographic algorithm," *IEEE Trans. Antennas Propag.*, vol. 66, no. 12, pp. 7295-7304, Dec. 2018.
- [133] M. Kalfa and H. E. Güven, "Fast 2-D Direction of Arrival Estimation Using Two-Stage Gridless Compressive Sensing," 2018 International Conference on Radar (RADAR), 2018, pp. 1-5.
- [134] S. Semper, F. Roemer, T. Hotz and G. Del Galdo, "Grid-Free Direction-of-Arrival Estimation with Compressed Sensing and Arbitrary Antenna Arrays," 2018 IEEE International Conference on Acoustics, Speech and Signal Processing (ICASSP), 2018, pp. 3251-3255.
- [135] O. Teke, A. C. Gurbuz and O. Arikan, "Perturbed Orthogonal Matching Pursuit," in *IEEE Transactions on Signal Processing*, vol. 61, no. 24, pp. 6220-6231, Dec.15, 2013.

CURRICULUM VITAE

PERSONAL INFORMATION

Surname, Name: Miran, Emre Alp
Nationality: Turkish (TC)
Date and Place of Birth: 3 January 1990, İzmir
email: alpmiran@gmail.com

EDUCATION

Degree	Institution	Year of Graduation
PhD	METU Electrical and Electronics Engineering	2022
BS	DEU Electrical and Electronics Engineering	2012
High School	Bornova Anadolu High School, İzmir	2008

WORK EXPERIENCE

Year	Place	Enrollment
2019-Present	ENGİTEK Mühendislik	RF Design Engineer
2012-2017	METU Dept. of Electrical and Electronics Eng.	Research/Teaching Assistant
2011 August	Vestel	Intern Eng. Student
2011 July	RFMD (Qorvo)	Intern Eng. Student

PUBLICATIONS

Journal Papers

1. E. A. Miran and M. Ciydem, "Dual-polarized elliptic-h slot-coupled patch antenna for 5G applications," Turkish Journal of Electrical Engineering & Computer Sciences.
2. E. A. Miran, F. S. Oktem and S. Koc, "Sparse reconstruction for near-field MIMO radar imaging using fast multipole method," in *IEEE Access*, vol. 9, pp. 151578-151589, 2021.
3. M. Ciydem and E. A. Miran, "A low-profile hybrid-fed dual-polarized antenna with high isolation and high cross-polar discrimination," The Applied Computational Electromagnetics Society Journal, 36(9), June 2021.
4. M. Ciydem and E. A. Miran, "Dual-polarization wideband sub-6 GHz suspended patch antenna for 5g base station," in *IEEE Antennas and Wireless Propagation Letters*, vol. 19, no. 7, pp. 1142-1146, July 2020.

Conference Papers

1. M.M. Taygur, Miran E.A., Yumrukaya E., Günel, S., BAŞ, S. "Low-cost FPGA-based antenna measurement system" 2013 IEEE Applied Electronics Conference, Pilsen.
2. Miran E.A., Koç S. "Amplitude tapering scheme for through element coupled antenna elements" 2016 IEEE International Symposium on Antennas and Propagation/USNC-URSI National Radio Science meeting, Fajardo, Puerto Rico.
3. Miran E.A., Koç S. "inside-wall imaging using synthetic aperture radar," 8th URSI Scientific Congress and National General Assembly Meeting, Ankara, Turkey, 2016. [in Turkish]
4. Miran E.A., Koç S. "Sparse solution to linear inverse problems with fast multipole method," 9th URSI Scientific Congress and National General Assembly Meeting, Konya, Turkey, 2018. [in Turkish]

5. Miran E.A., Koç S. “The fast multipole for sparse solution of linear inverse scattering problems” MMS 2018 The 18th Mediterranean Microwave Symposium, Istanbul, Turkey.